Doctoral Thesis

Studies of Converting Metal-Organic Frameworks for New Structures and Properties

Jae Hwa Lee

Department of Chemistry

Graduate School of UNIST

2019

Studies of Converting Metal-Organic Frameworks for New Structures and Properties

Jae Hwa Lee

Department of Chemistry

Graduate School of UNIST

Studies of Converting Metal-Organic Frameworks for New Structures and Properties

A thesis/dissertation

submitted to the Graduate School of UNIST

in partial fulfillment of the

requirements for the degree of

Doctor of Philosophy/Master of Science

Jae Hwa Lee

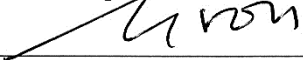06. 07. 2019

Approved by

_____

Advisor

Hoi Ri Moon

Studies of Converting Metal-Organic Frameworks for New Structures and Properties

Jae Hwa Lee

This certifies that the thesis/dissertation of Jae Hwa Lee is approved.
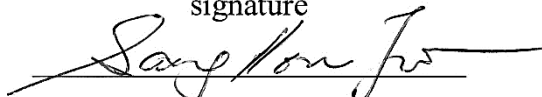
06. 07. 2019

signature

_____
Advisor: Hoi Ri Moon
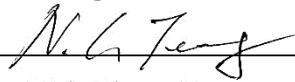
signature

_____
Myoung Soo Lah

signature

_____
Sang Hoon Joo

signature

_____
Min Kim

signature

_____
Nak Cheon Jeong

Abastract

Metal-organic frameworks (MOFs) are crystalline and porous solid materials formed by an extended network of metal ions (or clusters) coordinated to multidentate organic molecules. Therefore, with metal-ligand coordinative bonds stronger than hydrogen bonds, these materials have large internal surface areas, ultralow densities, and uniformly structured pores and channels. Also, the combination of their unique properties enables MOFs to have numerous promising applications, including hydrogen storage, methane storage, catalysis, sensing, and biomedical imaging. This new class of porous materials started to gain increasing interest in the 1990s, and now MOF chemistry is developing at an extraordinary pace with an explosion of papers in the chemical literature. In the line of MOF researches, it has been known that MOF structures have inherent transformability, and their dynamic properties are not only scientifically interesting but also practically applicable in various forms such as advanced nono-composite materials and stimuli-responsive smart materials.

In this sense, I demonstrated the utilization of MOFs as precursors, transforming into various functional nanomaterials with a special emphasis on understanding the relationship between the intrinsic nature of the parent MOFs and the daughter nanomaterials. For example, in section 2.2, I synthesized nanoporous manganese oxides via the thermal conversion of an Mn-based MOF by introducing another aliphatic ligand. Furthermore, we could control the oxidation states of the manganese oxides (i.e., MnO, Mn_3O_4, Mn_5O_8, and Mn_2O_3) by optimizing the sequential conversion reactions during annealing in N_2 and calcination with atmospheric oxygen. Importantly, the resultant MnO, Mn_3O_4, and Mn_5O_8 exhibited almost identical textural properties, including their morphology, surface areas, pore volumes, and the size of nanocrystals composing the nanoporous frameworks. Meanwhile, a Si-centered tetracarboxylic acid ligand that was capable of charge-balancing four Li+ ions was demonstrated. This newly designed MOF containing Li and Si was converted into Li-based ceramic, Li_4SiO_4 with an unusual morphology. In addition to these two approaches, the targeted sulfur elements can be directly incorporated into organic ligands to construct a MOF to be used as a single precursor for the preparation of nanostructured metal sulfide catalysts. Also, I exploited the pyrolysis of bimetallic MOFs with adipate introduced as an aliphatic ligand to prepare nanoporous structures consisting of nanocrystalline frameworks of transition-metal−ceria solid solutions.

Another trendy topic in the MOF field is imparting flexibility to MOF frameworks and revealing their structural dynamics so that external stimuli such as guest exchange, temperature, pressure, oxidation, and light can elicit structural rearrangement to alter the physicochemical properties of MOFs. Based on this background, I have prepared two flexible MOF crystals, a Luminescent Li-based MOF and a doubly interpenetrated Zn_4O-based MOF, which are capable of transforming their structures dynamically in a single-crystal to single-crystal manner upon the introduction of various nitroaromatic compounds including explosives or different kinds of solvents. Those results have allowed us to understand structural dynamism more deeply.

Contents

Chapter 3. Stimul-Responsive Transformation of Flexible MOFs

Acknowledgements

List of Figures

(a) in a box furnace with a ramping rate of 5 °C min^{-1} and (b) in a tube furnace under an oxygen flow of 100 mL min1 with a ramping rate of 1 °C min^{-1}. (c) XRPD patterns of MnO after heat treatment at 350 °C in a tube furnace under an oxygen flow of 100 mL min^{-1} and with different ramping rates of 1 °C min^{-1}, 3 °C min^{-1}, and 5 °C min^{-1}.

Figure 2.10. Characterization of an Mn$_2$O$_3$ sample: (a) XRPD pattern, (b) nitrogen adsorption−desorption isotherms, and (c,d) TEM images.

Figure 2.11. (a) Nitrogen adsorption–desorption isotherms and (b) Mn 3s XPS spectra of converted manganese oxides. The blue asterisk indicates the presence of low-valent (e.g. Mn^{2+}) manganese species in Mn$_5$O$_8$.

Figure 2.12. Pore size distribution of the nanoporous   manganese oxides obtained by BJH method from desorption branch of N$_2$ physisorption isotherm.

Figure. 2.13. Electrocatalytic activity of series of nanoporous manganese oxides for the ORR. (a) LSV curves of nanoporous manganese oxides on glassy carbon electrodes. (b) The numbers of electrons transferred at 0.4 V (vs. RHE) during the ORR obtained from the RRDE measurements. (c) Plot of the number of transferred electrons against potential during the ORR obtained by RRDE measurement. (d) Koutecký-Levich plots at 0.4 V (vs. RHE). The dotted lines show the theoretical slopes when two and four electrons are transferred during ORR. The numbers in the parentheses indicate the number of transferred electrons.

Figure 2.14. LSV polarization curves for the ORR measured at different rotating rates: (a) nanoporous Mn$_3$O$_4$, and (b) nanoporous Mn$_5$O$_8$.

Figure 2.15. Nyquist plots of the manganese oxide samples obtained by impedance spectra at a fixed potential of 0.7 V (vs. RHE) in O$_2$-saturated 0.1 M KOH.

Figure 2.16. LSV polarization curves for the nanoporous Mn$_5$O$_8$, Mn$_3$O$_4$, and MnO measured at 1600 rpm in O$_2$-saturated 0.1 M KOH.

Figure 2.17. Tetrakis(4-carboxyphenyl)silane (H$_4$TCS).

Figure 2.18. Crystal structure of LiTCS. (a) SBUs of the Li-COO chain. (b) The coordination modes of the carboxylates of a TCS^{4-} ligand. Three-dimensional framework formed by SBUs and organic ligands, projected along (c) the *c* axis and (d) the *b* axis. Coordinating DEF molecules and Li1 in Fig 2d were omitted for clarity. (Colour scheme: C, grey; O, red; N, blue; Si, orange; Li, purple.)

Figure 2.19. XRPD patterns of LiTCS: (a) measured pattern of as-synthesized LiTCS and (b) simulated pattern from the single-crystal X-ray diffraction data.

Figure 2.20. TGA traces of (a) LiTCS and (b) black powder Li$_4$SiO$_4$, measured under nitrogen and oxygen atmosphere, respectively. The result of the Li$_4$SiO$_4$ indicates 70% weight loss until 550 °C, corresponding to decomposition of carbon residue and further progress of incomplete reaction.

Figure 2.21. XRPD patterns of the Li$_4$SiO$_4$ (a) before and (b) after thermolysis under air at 650 °C.

Figure 2.22. SEM images of the as-synthesized Li$_4$SiO$_4$.

Figure 2.23. (a) SEM and (b) TEM images of the as-synthesised Li$_4$SiO$_4$, showing its coral-like morphology.

Figure 2.24. SEM and TEM images of the rock-like Li$_4$SiO$_4$ synthesized conventionally.

Figure 2.25. (a) TG curves of Li_4SiO_4 obtained at a heating rate of 5 °C/min in 15% CO_2 balanced with N_2. (b) Change in mass uptake of Li_4SiO_4 over time at different temperatures with a flow of 15% (v/v) CO_2 in N_2. (c) Gas-cycling result of the absorbent.

Figure 2.26. SEM images of the Li_4SiO_4 absorbent after twenty-five absorption-desorption cycles.

Figure 2.27. Schematic of MOF-derived synthesis of CdS nanocomposites with S-doped carbon.

Figure 2.28. Schematic illustration of the photocatalytic experiment for H_2O_2 production.

Figure 2.29. An ORTEP drawing of [Cd(EDDA)] with an atomic numbering scheme (thermal ellipsoids at 50% probability). Hydrogen atoms are omitted for clarity. Color scheme: Cd, purple; C, black; O, red; S, yellow.

Figure 2.30. XRPD patterns of [Cd(EDDA)]: (a) experimental and (b) simulated data.

Figure 2.31. TGA trance of [Cd(EDDA)] obtained under a nitrogen (blue line) or an oxygen (red line) atmosphere.

Figure 2.32. (a) Time-variable TGA trace of [Cd(EDDA)] at 270 °C under 100 mL/min of O_2 flow and (b) XRPD patterns of the corresponding [Cd(EDDA)], **$CdS_{O2,6h}$**, **$CdS_{O2,12h}$**, and **$CdS_{O2,24h}$**. (c) Representative TEM images of **$CdS_{O2,12h}$**.

Figure 2.33. XRPD patterns of [Cd(EDDA)], **$CdS_{N2,6h}$**, **$CdS_{N2,12h}$**, and **$CdS_{N2,24h}$**.

Figure 2.34. TEM images of **$CdS_{N2,24h}$**.

Figure 2.35. XPS spectra. (a) Cd $3d_{5/2}$, (b) S 2p, (c) O 1s, and (d) C 1s spectra of **$CdS_{O2,12h}$**.

Figure 2.36. EDS mapping of **$CdS_{O2,12h}$**.

Figure 2.37. Photocatalytic H_2O_2 production under visible light spectrum ($\lambda > 420nm$) in deionized water with 10% 2-propanol as a hole scavenger; (a) [Cd(EDDA)] and **$CdS_{O2,y}$** series, and (b) commercial CdS, **$CdS_{N2,24h}$**, and **$CdS_{O2,12h}$**. (c) Photocatalytic H_2O_2 decomposition and (d) comparison in use of hole scavenger for commercial CdS and **$CdS_{O2,12h}$**.

Figure 2.38. Photocatalytic hydrogen peroxide production of commercial CdS and **$CdS_{O2,12h}$** under visible light spectrum ($\lambda > 420nm$) in DI water for 24 h (a) without hole scavenger and (b) with 10% 2-propanol as a hole scavenger.

Figure 2.39. (a) EDS mapping of **Pt@CdS-0.53mol%**. (b) Photocatalytic H_2O_2 production of **$CdS_{O2,12h}$**, **Pt@CdS-0.53mol%**, and **CdS@Pt-0.04mol%**; under visible light spectrum ($\lambda > 420nm$) in deionized water with 10% 2-propanol as a hole scavenger.

Figure 2.40. TEM images of **Pt@CdS-0.53mol%**.

Figure 2.41. XRPD patterns of 0.53 mol% Pt-doped Cd(EDDA): experimental and simulated data from X-ray single-crystal data..

Figure 2.42. Photocatalytic hydrogen peroxide production of Commercial CdS and two other Pt-loaded commercial CdS samples (0.35 and 2.1 wt%, respectively) in a 10% 2-propanol solution.

Figure 2.43. Schematic of the nanoporous structure of np-$TM_xCe_{1-x}O_{2-\delta}$ (TM = Mn, Ni, Co, and Fe).

Figure 2.44. FT-IR spectra of four coordination compounds, Ce-*aph*-CP, $Mn_{0.11}Ce_{0.89}$-*aph*-CP, $Mn_{0.22}Ce_{0.78}$-*aph*-CP, and $Mn_{0.53}Ce_{0.47}$-*aph*-CP, measured by using attenuated total reflectance (ATR) technique.

Figure 2.45. XRPD patterns of the coordination compounds constructed with Ce^{3+} and an adipate ligand.

Figure 2.46. TGA traces of four coordination compounds, Ce-*aph*-CP, $Mn_{0.11}Ce_{0.89}$-*aph*-CP, $Mn_{0.22}Ce_{0.78}$-*aph*-CP, and $Mn_{0.53}Ce_{0.47}$-*aph*-CP under N_2 flow.

Figure 2.47. XRPD patterns of black solids obtained after N_2 treatment of coordination compounds, Ce-*aph*-CP (black), $Mn_{0.11}Ce_{0.89}$-*aph*-CP (red), $Mn_{0.22}Ce_{0.78}$-*aph*-CP (blue), and $Mn_{0.53}Ce_{0.47}$-*aph*-CP (dark yellow).

Figure 2.48. Comparison of nitrogen sorption isotherms before (black) and after (cyan) O_2 treatment for *np*-CeO_2.

Figure 2.49. XRPD patterns for the prepared *np*-$Mn_xCe_{1-x}O_{2-\delta}$ solid solutions and *np*-CeO_2, together with cubic CeO_2 standard card (JCPDS file no. 81-0792).

Figure 2.50. TEM images for (a) *np*-CeO_2, (b) *np*-$Mn_{0.08}Ce_{0.92}O_{2-\delta}$ solid solution, (c) *np*-$Mn_{0.18}Ce_{0.82}O_{2-\delta}$ solid solution, and (d) *np*-$Mn_{0.13}Ce_{0.87}O_{2-\delta} \cdot MnO_y$.

Figure 2.51. EDS mapping of (a) *np*-$Mn_{0.08}Ce_{0.92}O_{2-\delta}$ solid solution, (b) *np*-$Mn_{0.18}Ce_{0.82}O_{2-\delta}$ solid solution, and (c) *np*-$Mn_{0.13}Ce_{0.87}O_{2-\delta} \cdot MnO_y$.

Figure 2.52. N_2 sorption isotherms for *np*-CeO_2 and *np*-$Mn_xCe_{1-x}O_{2-\delta}$ samples. For clarity, the top three curves were offset by 60, 120, and 180 mL/g.

Figure 2.53. NLDFT pore size distribution curves of *np*-$Mn_xCe_{1-x}O_{2-\delta}$ solid solutions as well as *np*-CeO_2.

Figure 2.54. (a) Raman spectra of the *np*-$Mn_xCe_{1-x}O_{2-\delta}$ series and *np*-CeO_2. (b) Mn 3s XPS spectra of *np*-$Mn_xCe_{1-x}O_{2-\delta}$ solid solutions.

Figure 2.55. (a) H_2-TPR profiles for *np*-CeO_2, *np*-$Mn_{0.18}Ce_{0.82}O_{2-\delta}$, and *imp*-$CeO_2$-Mn(0.2) samples. (b) CO oxidation curves of *np*-CeO_2 as well as the *np*-$Mn_xCe_{1-x}O_{2-\delta}$ series. (c) Arrhenius plots of CO oxidation with pure CeO_2 and *np*-$Mn_xCe_{1-x}O_{2-\delta}$ samples.

Figure 2.56. TEM images for the *imp*-CeO_2-Mn(0.2).

Figure 2.57. XRPD patterns for the *imp*-CeO_2-Mn materials with cubic CeO_2 standard card (JCPDS file no. 81-0792).

Figure 2.58. H_2-TPR profiles for *np*-CeO_2 as well as *np*-$Mn_xCe_{1-x}O_{2-\delta}$ solid solutions.

Figure 2.59. CO-TPD profiles for *np*-CeO_2 as well as *np*-$Mn_xCe_{1-x}O_{2-\delta}$ solid solutions.

Figure 2.60. XRPD patterns of the *np*-$TM_xCe_{1-x}O_{2-\delta}$ series (TM = Ni, Co, Fe, and Mn) and *np*-CeO_2.

Figure 2.61. TEM images for converted *np*-$Ni_{0.08}Ce_{0.92}O_{2-\delta}$, *np*-$Co_{0.08}Ce_{0.92}O_{2-\delta}$ and *np*-$Fe_{0.09}Ce_{0.91}O_{2-\delta}$ solid solutions.

Figure 2.62. EDS mapping for *np*-$Ni_{0.08}Ce_{0.92}O_{2-\delta}$, *np*-$Co_{0.08}Ce_{0.92}O_{2-\delta}$ and *np*-$Fe_{0.09}Ce_{0.91}O_{2-\delta}$ solid solutions.

Figure 2.63. N_2 sorption isotherms for *np*-$M_xCe_{1-x}O_{2-\delta}$ series and *np*-CeO_2. For clarity, the isotherm curves for *np*-$Ni_{0.08}Ce_{0.92}O_{2-\delta}$, *np*-$Co_{0.08}Ce_{0.92}O_{2-\delta}$, *np*-$Fe_{0.09}Ce_{0.91}O_{2-\delta}$ and *np*-$Mn_{0.08}Ce_{0.92}O_{2-\delta}$ were offset by 50, 100, 150 and 200 mL/g, respectively.

Chapter 3

Figure 3.1. Schematic view of the adsorption profiles of rigid microporous frameworks (red line, Type I behaviour) and adsorption-induced flexible frameworks (green line, S-shaped Type V behaviour).

Figure 3.2. (a) Tabular summary of the thermo- and piezo-mechanical properties as a function of different classes of MBUs, based on the reported force constants. Schematic representations of (b) MOF-5 and (c) MIL-53 with their 2D MOF analogues made up of MBUs.

Figure 3.3. Chemical, topological, and mechanical representations of MOF-5. The far-right column represents mechanical systems of molecular trusses.

Figure 3.4. Unit cell with directions of highest and lowest Young's modulus E (left) and directional Young's modulus E at 300 K and 0 MPa represented as a 3D map (right); (a) MOF-5, (b) MIL-53-LP, and (c) MIL-53-NP.

Figure 3.5. Schematic structure of organic ligand H_2CPMA.

Figure 3.6. Preparation of bis(4-carboxyphenyl)-*N*-methylamine (H_2CPMA).

Figure 3.7. Single-crystal X-ray structure of **1**. (a) SBU of Li-O chain. (b) 3D framework formed by association of SBUs and organic ligands, projected along the *c*-axis. Hydrogen atoms and non-coordinating guest molecules are omitted for clarity. (Color scheme: C, white; O, red; N, blue; and Li, light blue) The yellow rectangle indicates the SBU of the Li-O chain.

Figure 3.8. An ORTEP drawing with an atomic numbering scheme (thermal ellipsoids at 30% probability). Hydrogen atoms are omitted for clarity. The hydrogen atoms of coordinated water molecules were not located. Symmetry operations: #1, x-1/2, -y+1/2, z; #2, -x+3/2, y+1/2, z; #3, -x+3/2, -y+1/2, z-1/2; #4, -x+2, y, z-1/2; #5, x, -y, z-1/2.

Figure 3.9. Synchrotron X-ray powder diffraction data ($\lambda = 0.79984$ Å) measured at 95 K for (a) as-synthesized **1** and (c) **1**⊃nitrobenzene, and simulated patterns from X-ray single-crystal data of (b) as-synthesized **1** and (d) **1**⊃nitrobenzene, respectively.

Figure 3.10. TGA trace of $\{Li_3[Li(DMF)_2](CPMA)_2\}\cdot4DMF\cdot1H_2O$ (**1**).

Figure 3.11. Comparison of X-ray powder diffraction data for (a) as-synthesized Li-MOF **1**, and (b) dried MOF.

Figure 3.12. Gas sorption isotherms of Li-MOF **1**.

Figure 3.13. Transmission FT-IR spectra of (a) **1** (black) and (b) **1**⊃nitrobenzene (red).

Figure 3.14. Photographs of **1** after immersing in neat nitrobenzene, benzene, toluene, and 2,4-dinitrotoluene (DNT)/DMF solution, respectively.

Figure 3.15. N 1s XPS result of **1**⊃nitrobenzene.

Figure 3.16. UV-visible spectra of **1** (black) and **1**⊃nitrobenzene (red) in the solid state.

Figure 3.17. Detection of nitrobenzene in **1**. (a) Photographs of **1**, **1**⊃nitrobenzene, and **1** regenerated by heating. (b) Fluorescence spectra of **1** and **1**⊃nitrobenzene.

Figure 3.18. Fluorescence spectra of **1** and **1**$\supset$DNT.

Figure 3.19. (a) Nitrobenzene concentration-dependent fluorescence spectra of Li-MOF **1**. (b) Percentage of fluorescence at the λ_{max}, estimated using formula (I_a/I_0) x 100%, where I_0 is the maximum intensity of Li-MOF **1**, and I_a is the maximum intensity of Li-MOF **1** after immersion in a M nitrobenzene/DMF solution.

Figure 3.20. (a) X-ray structure of **1**$\supset$nitrobenzene, in which π-π and C-H···π interactions are emphasized by the orange ball-and-stick representation (color scheme: C, white; O, red; N, blue; and Li, light blue). (b) Close-up shot of interaction between nitrobenzene (orange) and CPMA^{2-} incorporated in **1**. (c) Comparison of the superimposed X-ray structures of **1** (cyan), and **1**$\supset$ nitrobenzene (orange).

Figure 3.21. (a) Organic ligand H$_2$CPMA. (b) A single network unit with **pcu** topology composed of Zn$_4$O clusters and CPMA^{2-} ditopic ligands. (c) - (d) Doubly interpenetrated 3D framework and its simplified view.

Figure 3.22. The interpenetrated structocure of two **pcu** nets in **1** which interact each other via π- π interactions.

Figure 3.23. TGA trace of [Zn$_4$O(CPMA)$_3$]$_2$•12DMF (**1**). The result indicates 28.7% weight loss under 150 °C for twelve uncoordinating DMF guest molecules (calc. 28.8%).

Figure 3.24. The XRPD patterns for (a) **1** as-synthesized, (b) simulated pattern from the single-crystal X-ray data of **1**, (c) dried **1** that is prepared by heating **1** at 220 °C under vacuum for 24 h, and (d) solid isolated after exposure of dried **1** to DMF vapor for 3 days.

Figure 3.25. The XRPD patterns for (a) **1**$_{benzene}$ as-synthesized, (b) simulated pattern from the single-crystal X-ray data of **1**$_{benzene}$, (c) dried **1**$_{benzene}$ that is prepared by heating **1**$_{benzene}$ at 200 °C under vacuum for 24 h, and (d) solid isolated after immersion of **1**$_{benzene}$ to benzene solvent for 3 d at room temperature.

Figure 3.26. The XRPD patterns for (a) **1**$_{hexane}$ as-synthesized, (b) simulated pattern from the single-crystal X-ray data of **1**$_{hexane}$, (c) dried **1**$_{hexane}$ that is prepared by heating **1**$_{hexane}$ at 200 °C under vacuum for 12 h, and (d) solid isolated after exposure of dried **1**$_{hexane}$ to hexane vapor for 3 d at room temperature.

Figure 3.27. The XRPD patterns for (a) **1**$_{MeOH}$ as-synthesized, (b) simulated pattern from the single-crystal X-ray data of **1**$_{MeOH}$, (c) dried **1**$_{MeOH}$ that is prepared by heating **1**$_{MeOH}$ at 100 °C under vacuum for 12 h, and (d) solid isolated after exposure of dried **1**$_{MeOH}$ to methanol vapor for 3 d at room temperature.

Figure 3.28. The exchange degree of 1 with benzene as a function of time.

Figure 3.29. FT-IR spectra of **1**, **1**$_{benzene}$, **1**$_{hexane}$, and **1**$_{MeOH}$.

Figure 3.30. Photographs of **1** crystals in guest-exchange processes. Left column: **1** as-synthesized sealed in a glass cappillary together with the mother liquor. Right column: After immsion in each organic solvent for 60 h. (a) benzene, (b) *n*-hexane, and (c) MeOH.

Figure 3.31. Host-guest and guest-guest interactions in (a) **1**, (b) **1**$_{benzene}$, (c) **1**$_{hexane}$, and (d) **1**$_{MeOH}$. In (c), θ and θ' are the offset angles of the two phenyl rings. Colour scheme: C (grey), O (red), H (white), Zn (purple).

Figure 3.32. π-π interactions between doubly interpenetrated *pcu* nets and hydrogen bond interactions of MeOH molecules with water molecules or carboxylate oxygen atoms in 1_{MeOH}.

Figure 3.33. TGA traces of $[Zn_4O(CPMA)_2]_2 \cdot 12DMF$ (**1**, black), $[Zn_4O(CPMA)_3]_2 \cdot 6(n\text{-hexane})$ (1_{hexane}, red), $[Zn_4O(CPMA)_3]_2 \cdot 7benzene$($1_{benzene}$, blue), and $[Zn_4O(CPMA)_3]_2 \cdot 9MeOH \cdot 5H_2O$ (1_{MeOH}, green).

Figure 3.34. CH-π interactions between hexane molecules and phenyl rings of $CPMA^{2-}$ ligands in the framework, 1_{hexane}.

Figure 3.35. The XRPD patterns for (a) **1** as-synthesized, (b) that simulated based on X-ray single-crystal data of **1**, (c) a solid isolated $1_{benzene}$ after immersion of **1** in benzene for 60 h, (d) that simulated based on X-ray single-crystal data of $1_{benzene}$, (e) a solid isolated 1_{hexane} after immersion of **1** in *n*-hexane for 60 h, (f) that simulated based on X-ray single-crystal data of 1_{hexane}, (g) a solid isolated after immersion of 1_{MeOH} in MeOH for 60 h, and (h) that simulated based on X-ray single-crystal data of 1_{MeOH}.

List of Tables

Chapter 1. General Introduction

1.1. Metal-organic framework

Metal–organic frameworks (MOFs) are a class of crystalline solids in which metal cations or clusters are linked by organic struts via coordination bonds (Figure 1.1).[1,2] According to the IUPAC definition, MOFs are described as a "coordination network with organic ligands containing potential voids." The high degree of tunability and modularity of MOFs with a variety of metal building blocks and organic linkers have generated a myriad of MOFs that allow for their applications in a wide range of areas.[3-5] In particular, organic ligands as structure-directing building units provide two important features for MOFs: (1) added flexibility and diversity in the geometric structures of MOFs[6-8] and (2) alteration of the electronic structures and surface functionalities of MOFs.[9-11] Because the structure of a MOF is the decisive factor in these functionalities, various symmetry conformations, lengths and dimensions, and numbers of coordinating groups in the ligands have been adopted for the construction of functional MOFs.
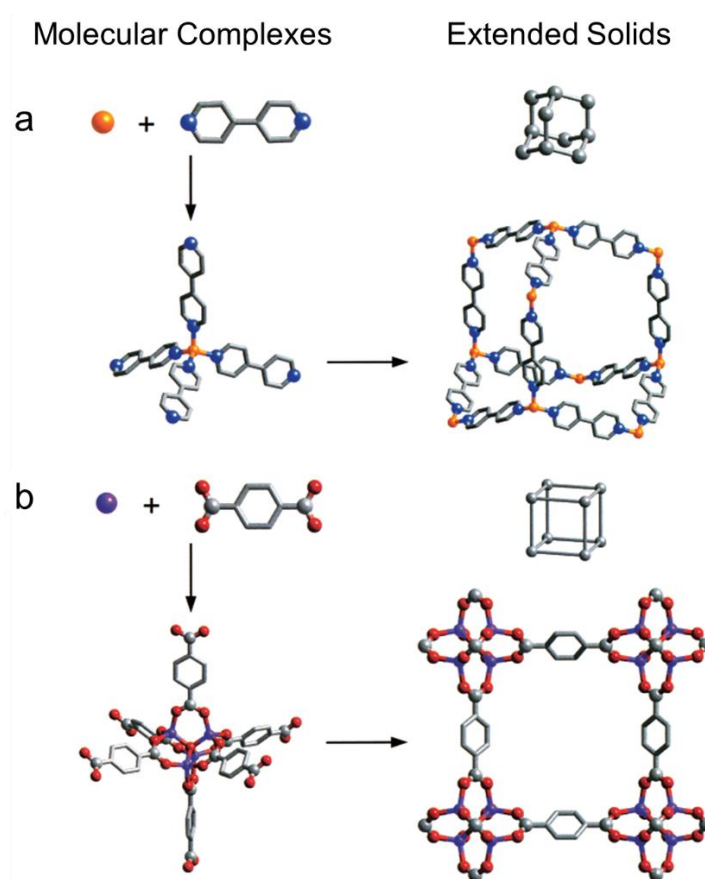
Figure 1.1. Copolymerization of metal ions with organic linkers toward assembly of MOFs, and specific examples of (a) metal-bipyridine structures with expanded diamond topology and (b) MOF-5 structure composed of metal-carboxylate clusters that are linked by benzene struts.[1]

1.2. Rigidity and flexibility of MOFs

The history of MOFs dates back 30 years when Robson reported an 'infinite polymeric framework',[12] after which, Yaghi coined the term 'metal-organic framework' in 1995.[13] At the time, a wide variety of microporous coordination compounds, which usually accommodated guest solvent molecules in the pores, were known. However, unfortunately, most of the compounds irreversibly lost their crystallinity and porosity upon the removal of the guest molecules. Therefore, a major research effort was devoted to the synthesis of MOFs that could endure the guest removal/reintroduction without the alteration of their porous structures. Based on this trend, in 1998, Kitagawa classified MOFs into three categories: 1st,2nd, and 3rd generation MOFs (illustrated in Figure 1.2a).[14,15] Interestingly, he defined the 3rd generation compounds as flexible porous frameworks that respond to external stimuli, and predicted their appearance and prevalence in the immediate future. From 2002 onwards, owing to the pioneering works led by Férey's and Kitagawa's groups, studies on the synthesis and utilization of flexible MOFs have attracted extensive interests.[16-18]
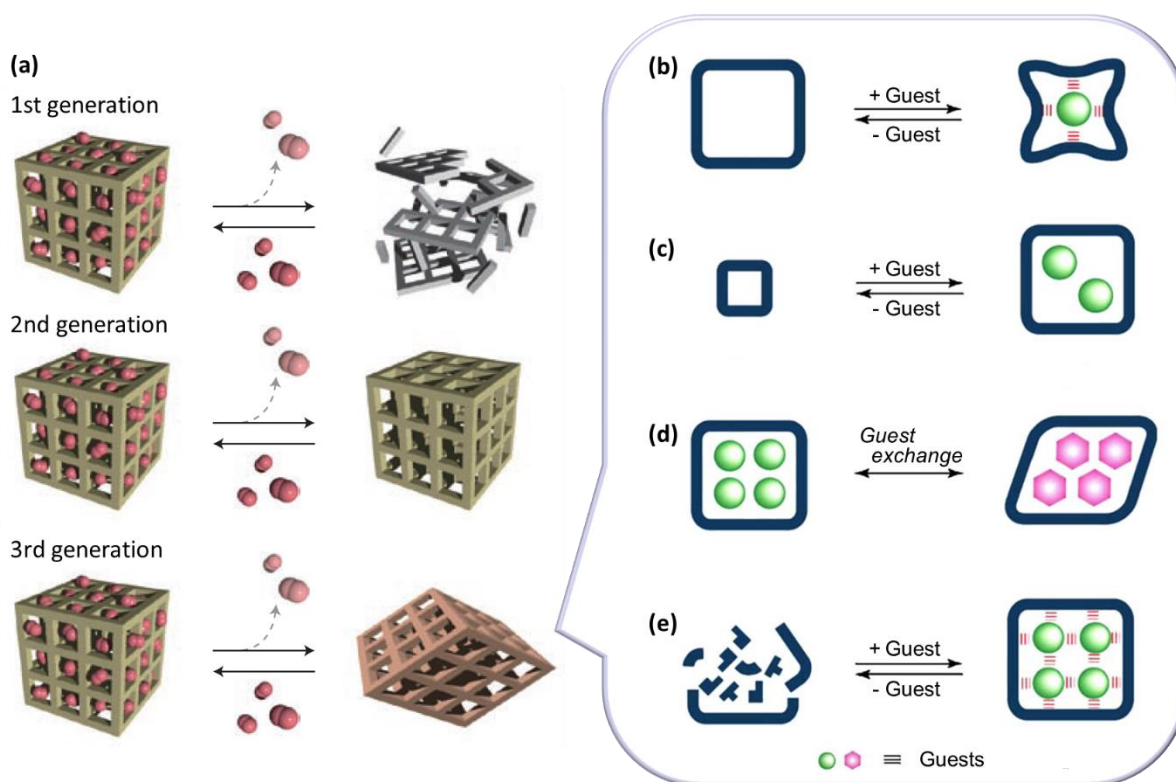
Figure 1.2. (a) Classification of porous coordination polymers (or MOFs) as 1st, 2nd, and 3rd generation ones (left side). The illustrations in the box on the right side represent the behaviors of dynamic structures upon adsorption/desorption of guest molecules; (b) induced-fit-type pores, (c) breathing-type pores, (d) guest-exchange deformation-type pores, and (e) healing-type pores.[19,20]

In 2005, Kitagawa et al. focused on the relationship between the guest molecules and pores of flexible MOFs in a review.[19] As shown in Figure 1.2b–e, the dynamic pore behaviors depending on the presence and absence of guests were categorized into four types: (b) induced-fit-type pores, (c) breathing pores, (d) guest exchange pores with deformation, and (e) healing pores. Overall, type (b)/(d) pores respond to the guest molecules, staying open during the guest inclusion or exchange. In contrast, type (c)/(e) undergo structural transformation from close to open form. This implies that the pore properties of a host framework and interactions between guest and pore-wall molecules both play a key role in determining the difference between these four types of behaviors. It is worth noting that, according to our definition of flexibility, as stated above, controversies might arise as to whether type (e) can be considered 'flexible', because the framework does not retain the structural topology during its deformation, although the authors regarded it as a flexible framework.

Actually, the term 'flexibility' used in the field of MOFs has been somewhat vague. According to common sense, one can designate a MOF as a flexible MOF when a significant yet reversible change in the unit cell is observed upon a change in the external environment. However, in terms of the structural dynamism, the scope of flexible motions would be very wide whether it is at the microscopic or macroscopic level. For example, it appears in various forms such as the rearrangement of the metal-carboxylate (M-COO) cluster constituting the secondary building unit (SBU), the rotation of the benzene ring of the organic ligand, and the expansion/contraction of the cell volume. Even MOF-5 and HKUST-1, the MOFs known to be rigid, dis-play certain degree of flexibility (which will be discussed later in detail). In a similar sense, in 2009, Susumu Kitagawa newly categorized MOFs as 'soft porous crystals'.[20] According to his definition, structural flexibility (or transformability) in a crystalline phase is only enabled via the cooperative integration of softness (atomic and molecular freedom of motion) and rigidity (mechanical strength to maintain the crystal integrity). On the other hand, regional molecular displacements can occur without altering the host framework entirely (e.g., movement of dangling chains into the pores, rotation of phenyl rings, and exchange of coordinating solvents). In this background, the broad community of chemists, materials scientists, and engineers have been devoting to elucidate the rigidity/flexibility of MOFs in depth and impart the basic principles.

Through much research progress to date, the very definition of flexibility in MOF community continues to expand. For instance, reversible switching of MOFs between crystalline and amorphous solid or liquid states has also been demonstrated in a few studies,[21-23] and these might be categorized as a new type of flexible MOFs. Likewise, depending on the perspective, flexibility can bein various forms, from just vibrational motions in so-called rigid MOFs to soft porosity like breathing effects and the structural collapses with higher disorder. In this regard, Bennett et al. provided a new intriguing perspective that flexibility, defects, and disorder are not just prevalent in MOFs but are also strongly related to each other in terms of entropy, exemplified with specific studies (Figure 1.3).[24] Recent active researches into defects and disorder have redefined even our perception of MOFs as crystalline

materials, combining with advances in the understanding of the flexible behavior of soft porous MOFs.[21,25]
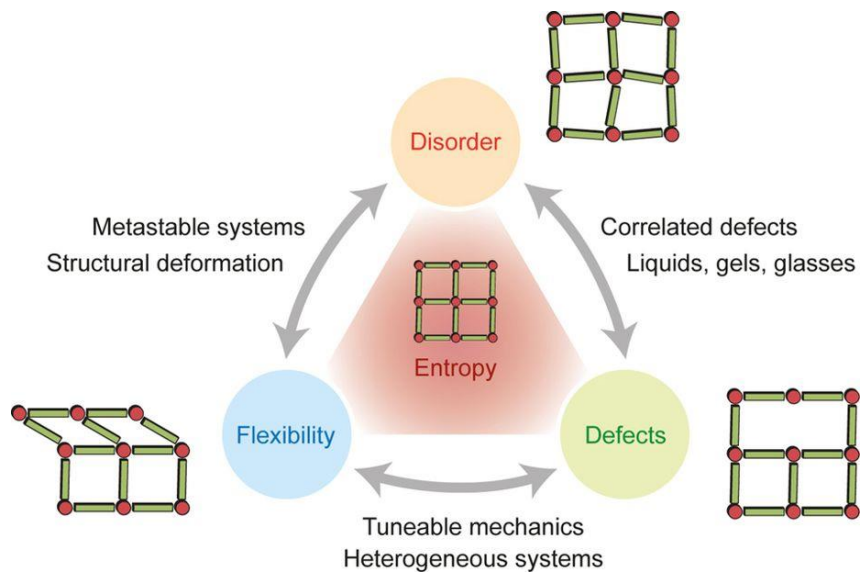
Figure 1.3. Illustration of the interplay between the intertwined concepts of flexibility, defects and disorder in MOFs, highlighting some of the phenomena (grey arrows) that emerge from their coupling. Entropy plays a central role in all these systems.[24]

1.3. Thermal decomposition and transformation of MOFs into nanomaterials

Nanostructured materials such as porous metal oxides, assembled metal nanoparticles (NPs), porous carbons, and their composites have been intensively studied due to a variety of applications including energy conversion and storage devices, catalysis, and gas storage.[26] In order to synthesize the target materials, the appropriate precursors and synthetic methods are adopted. For instance, soft- and hard-templating routes are commonly used to develop pores by incorporating organic and inorganic precursors for porous carbon and metal oxides, respectively.[27,28] To prepare composite materials of carbon and metal species, sequential and/or separate synthesis are required. As a new type of a precursor for these nanomaterials, metal-organic frameworks (MOFs) deserve attention because they contain both organic and inorganic species, which can play parallel roles as both a template and a precursor in parallel under appropriate conditions.[29]

Metal/metal-oxide nanoparticles embedded in a carbon matrix can be obtained from direct thermolysis of MOFs (Figure 1.4).[30,31] Over the thermal decomposition temperature and under inert atmosphere, organic linking 'struts' begin to collapse, and metal ions (or metal clusters) aggregate to form nanoparticles. Decomposed organic species can inhibit the agglomeration of nanoparticles by surrounding them as the amorphous carbon matrix. The amorphous carbon can be also removed through calcination under the air or utilized together with nanoparticles as composite materials.[16] Especially, these nanostructured materials directly synthesized from MOFs have performed well in fuel cell catalysts and battery electrodes.[32-35]
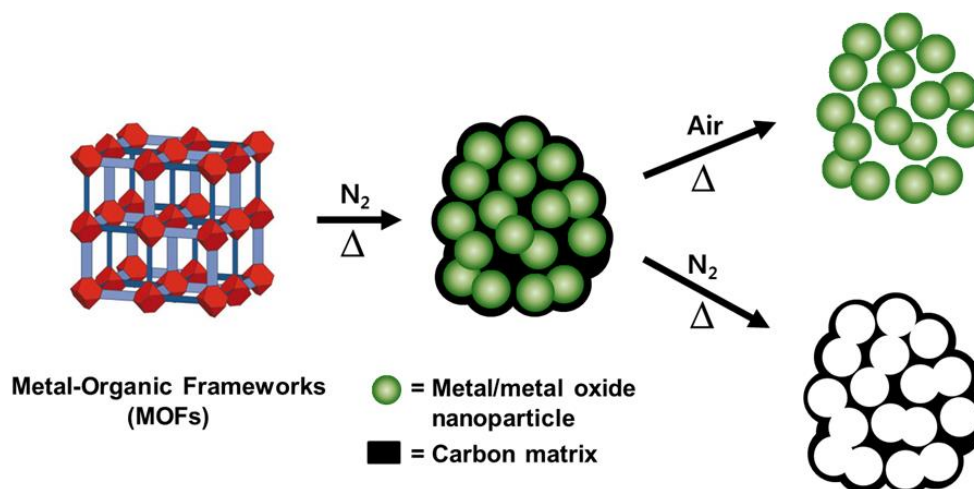
Figure 1.4. Schematic view of thermolysis of MOFs to synthesize metal/metal-oxide nanoparticles or nanoporous carbon-based materials.

Nanoporous graphitic carbon can be produced in a similar but opposite way. In 2008, for the first time, Xu et al. reported an MOF as a template to prepare nanoporous carbon.[36] They confirmed that ZnO is reduced into Zn metal at a temperature higher than 800 $^{\circ}C$ and subsequently vaporized (boiling

point of Zn is 908 °C) at 1000 °C for 8 h under an Ar flow, leaving the carbon species with nanopores. Since then, many advanced nanoporous carbon materials have been reported based on this method (Figure 1.5), attempting to adjust heat treatments,[37] switch additional carbon sources,[38] and change the kinds of MOFs.[39] Those nanoporous carbons have exhibited not only improved gas uptake with a high specific surface area but also excellent electrochemical properties in electrodes.
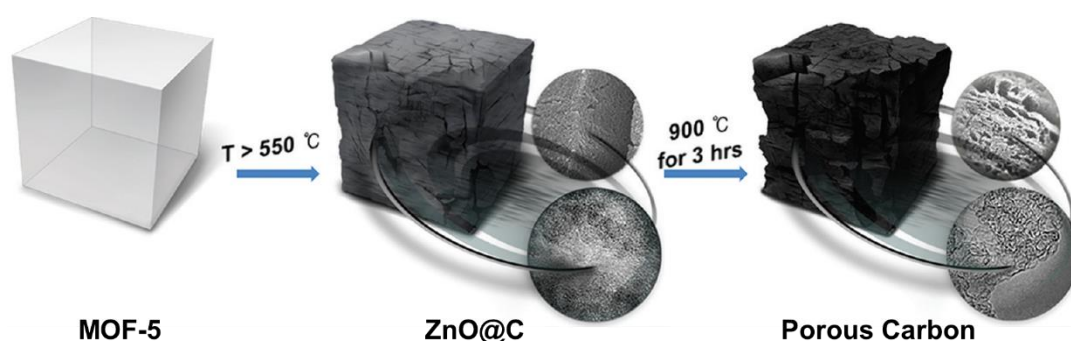
Figure 1.5. Schematic view of structural changes of MOF with heat-treatment to yield the highly porous carbon material.

References

1. M. Eddaoudi, D. B. Moler, H. Li, B. Chen, T. M. Reineke, M. O'Keeffe, O. M. Yaghi, *Acc. Chem. Res.* **2001**, *34*, 319-330.
2. H. Furukawa, K.E. Cordova, M. O'Keeffe, O. M. Yaghi, *Science* **2013**, *341*, 1230444.
3. M. P. Suh, Y. E. Cheon, E. Y. Lee, *Coord. Chem. Rev.* **2008**, *252*, 1007–1026.
4. B. Li, M. Chrzanowski, Y. Zhang, S. Ma, *Coord. Chem. Rev.* **2016**, *307*, 106–129.
5. K. J. Lee, J. H. Lee, S. Jeoung, H. R. Moon, *Acc. Chem. Res.* **2017**, *50*, 2684–2692.
6. D. Zhao, D. J. Timmons, D. Yuan, H.-C. Zhou, *Acc. Chem. Res.* **2011**, *44*, 123−133.
7. O. M. Yaghi, M. O'Keeffe, N. W. Ockwig, H. K. Chae, M. Eddaoudi, J. Kim, *Nature* **2003**, *423*, 705−714.
8. R. Wang, J. Zhang, L. Li, *Inorg. Chem.* **2009**, *48*, 7194−7200.
9. A. Kuc, A. Enyashin, G. Seifert, *J. Phys. Chem. B* **2007**, *111*, 8179−8186.
10. W. Cao, Y. Li, L. Wang, S. Liao, *J. Phys. Chem. C* **2011**, *115*, 13829−13836.
11. C. A. Bauer, T. V. Timofeeva, T. B. Settersten, B. D. Patterson, V. H. Liu, B. A. Simmons, M. D. Allendorf, *J. Am. Chem. Soc.* **2007**, *129*, 7136−7144.
12. B.F. Hoskin, R. Robson, *J. Am. Chem. Soc.* **1989**, *111*, 5962-5964.
13. O.M. Yaghi, H. Li, *J. Am. Chem. Soc.* **1995**, *117*, 10401-10401.
14. S. Kitagawa, M. Kondo, *Bull. Chem. Soc. Jpn.* **1998**, *71*, 1739-1753.
15. S. Kitagawa, R. Kitaura, S.-I. Noro, *Angew. Chem. Int. Ed.* **2004**, *43*, 2334-2375.
16. K. Barthelet, J. Marrot, D. Riou, G. Férey, *Angew. Chem. Int. Ed.* **2002**, *41*, 281-284.
17. C. Serre, F. Millange, C. Thouvenot, M. Nogues, G. Marsolier, D. Loüer, G. Férey, *J. Am. Chem. Soc.* **2002**, *124*, 13519-13526.
18. K. Uemura, S. Kitagawa, M. Kondo, K. Fukui, R. Kitaura, H.-C. Chang, T. Mizutani, *Chem. Eur. J.* **2002**, *8*, 3586-3600.
19. K. Uemura, R. Matsuda, S. Kitagawa, *J. Solid State Chem.* **2005**, *178*, 2420-2429.
20. S. Horike, S. Shimomura, S. Kitagawa, *Nat. Chem.* **2009**, *1*, 695-704.
21. T.D. Bennett, S. Horike, *Nat. Rev.* **2018**, *3*, 431-440.

22. D. Umeyama, S. Horike, M. Inukai, T. Itakura, S. Kitagawa, *J. Am. Chem. Soc.* **2015**, *137*, 864-870.
23. J.-W. Xiu, G.-E. Wang, M.-S. Yao, C.-C. Yang, C.-H. Lin, G. Xu, *Chem. Commun.* **2017**, *53*, 2479-2482.
24. T.D. Bennett, A.K. Cheetham, A.H. Fuchs, F.-X. Coudert, *Nat. Chem.* **2017**, *9*, 11-16.
25. C. Zhou, L. Longley, A. Krajnc, G.J. Smales, A. Qiao, I. Erucar, C.M.Doherty, A.W. Thornton, A.J. Hill, C.W. Ashling, O.T. Qazvini, S.J.Lee, P.A. Chater, N.J. Terrill, A.J. Smith, Y. Yue, G. Mali, D.A. Keen, S.G. Telfer, T.D. Bennett, *Nat. Commun.* **2018**, *9*, 5042.
26. A. S. Aricò, P. Bruce, B. Scrosati, J.-M. Tarascon, W. van Schalkwijk, *Nat. Mater.* **2005**, *4*, 366−377.
27. R. Ryoo, S. H. Joo, M. Kruk, M. Jaroniec, *Adv. Mater.* **2001**, *13*, 677−681.
28. A.-H. Lu, F. Schüth, *Adv. Mater.* **2006**, *18*, 1793−1805.
29. W. Xia, A. Mahmood, R. Zou, Q. Xu, *Energy Environ. Sci.* **2015**, *8*, 1837− 1866.
30. R. Das, P. Pachfule, R. Banerjee, P. Poddar, *Nanoscale* **2012**, *4*, 591− 599.
31. X. Xu, R. Cao, S. Jeong, J. Cho, *Nano Lett*. **2012**, *12*, 4988-4991.
32. W. Cho, S. Park, M. Oh, *Chem. Commun.* **2011**, *47*, 4138-4140.
33. W. Wang, Y. Li, R. Zhang, D. He, H. Liu, S. Liao, *Catal. Commun.* **2011**, *12*, 875-879.
34. B. Liu, X. Zhang, H. Shioyama, T. Mukai, T. Sakai, Q. Xu, *J. Power Sources.* **2010**, *195*, 857-861.
35. M. S. Y. Parast, A. Morsali, *Inorg. Chem. Commun.* **2011**, *14*, 645-648.
36. B. Liu, H. Shioyama, T. Akita, Q. Xu, *J. Am. Chem. Soc*. **2008**, *130*, 5390-5391.
37. S. J. Yang, T. Kim, J. H. Im, Y. S. Kim, K. Lee, H. Jung, C. R. Park, C. R. *Chem. Mater*. **2012**, *24*, 464-470.
38. J. Hu, H. Wang, Q. Gao, H. Guo, *Carbon.* **2010**, *48*, 3599-3606.
39. S. Lim, K. Suh, Y. Kim, M. Yoon, H. Park, D. N. Dybtsev, K. Kim, *Chem. Commun*. **2012**, *48*, 7447-7449.

Chapter 2. Thermal Conversion into Functional Nanomaterials

2.1. Fundamentals

MOFs are well-ordered crystalline materials constructed from coordination bonds between organic ligands and metal ions. So far these days, most works on MOFs have been targeted for synthesizing new MOFs and examining their applications such as catalysis, sensing, gas storage and separation, and electronics.[1,2] In MOF frameworks, the inorganic and organic components are periodically arranged at a certain distance, which enables their conversion reaction to produce materials with well-defined structures and chemical compositions even in the solid state. Owing to the countless types of metal ions/ clusters and organic ligands that comprise MOFs, the coordination strength between those components and the thermal stability of the framework can vary extensively. This implies that various chemical reactions can occur according to the precursor MOFs and conversion condition, thus providing inexhaustible potential for synthesizing diverse functional nanomaterials

Over the past decade, the thermal conversion of MOFs and applications of the resulting materials have been increasingly studied, particularly for electrocatalysis. The results have proved that MOFs offer a promising toolbox for synthesizing advanced nanomaterials that are not easily obtainable using conventional methods. Many relevant reviews have been published by groups of Xu, Gascon, and Yamauchi.[3-6] According to previous literatures, the high dimensionality and porosity are not always necessary requirements for the targeted functionalization of nanomaterials, even though those factors make MOFs distinguished from their coordination compounds. In this sense, recent works have also extended the materials of interest from MOFs to coordination polymers (CPs), which represent a conceptually lager family of materials than MOFs; CPs are defined as "a coordination compound with repeating coordination entities extending in 1, 2, or 3 dimensions," and MOFs as a "coordination network with organic ligands containing potential voids."[7]

Pioneering studies on MOF conversion were conducted by the Morsali group, who synthesized various nanosized metal oxides by calcining CPs in air, which were collectively discussed in a review article in 2012.[8] However, because of rapid, severe reactions between CPs and O_2 such as carbon combustion and metal oxidation, the products were not sufficiently well controlled to generate nanomaterials. Thus, recent studies on converting MOFs and CPs have mostly focused on thermolysis under an inert atmosphere. Performing the conversion reaction under these conditions enables emphasizing and revealing the role of the organic ligands on the phase and structural transition during the decomposition of MOFs, which will be discussed in this Account. Meanwhile, several intriguing solution-based conversions of MOFs have been reported,[9,10] but those wet chemical synthetic routes will be excluded from this Account, which deals solely solid-state conversion. Furthermore, Prussian

blue analogue (PBA), a representative cyanide-based coordination compound, has been widely used as a precursor, usually to produce hollow metal-based nanomaterials.[11]
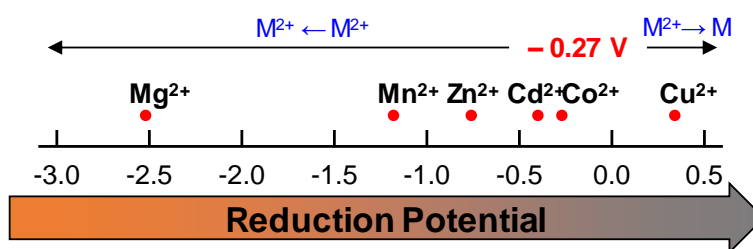
Figure 2.1. Effect of the reduction potentials of the metal ions in MOFs on the formation of metal/metal oxide species.[12]

To examine the thermal stability of MOFs, thermogravimetric analysis (TGA) is routinely performed under an inert atmosphere. Upon heating, MOFs mostly lose solvent molecules first, and then their entire structures thermally decompose at higher temperatures (principally >400 °C). In a TGA trace, this decomposition is indicated by an abrupt weight loss, which is usually attributed to organic ligands. Tens of percent by weight remain after the thermal decomposition is completed. In this section, our main area of interest is the remaining compounds during and after the destruction of MOFs, especially metal-based materials. Das et al. proposed that the reduction potentials of metal ions in MOFs are the standard factor to explain and predict the resultant materials (Figure 2.1).[12] Metal ions with a standard reduction potential of −0.27 V or higher generate the metal phase after pyrolysis under an inert atmosphere, while those with a reduction potential of less than −0.27 V generate the metal oxide phase. Although highly significant, this threshold would be not generally applicable because it does not consider chemical reactions with organic substances. Organic ligands for MOFs mostly consist of C, N, and O, but the compositions can be extended to include other elements such as S, P, and Se to produce metal chalcogenides and pnictides. Therefore, understanding the mechanism of MOF conversion is not a simple issue, and thus, designing tailor-made MOFs to synthesize target nanomaterials is very challenging.
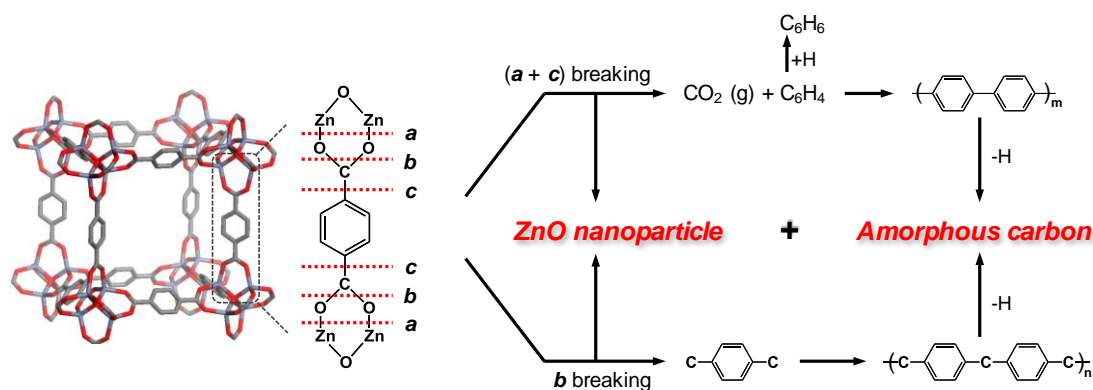
Figure 2.2. Schematic view of the decomposition mechanism of MOF-5.

In 2010, Hu and Zhang were the first to propose a mechanism for the decomposition of MOF-5 ($[Zn_4O(BDC^{2-})_3]_n$; BDC = terephthalate).[13] As shown in Figure 2.2, three types of cleavages, *a*, *b*, and *c*, are plausible below 500 °C, and as evidenced by the temperature-programmed mass spectrum (MS) the combination of breaking at positions (*a* + *c*) and b resulted in ZnO and CO_2 with benzene-derived carbon species, which then formed amorphous carbon. Therefore, the product of the thermolysis of MOF-5 was a composite of ZnO nanocrystals covered with amorphous carbon. Based on an understanding of this MOF-5 decomposition mechanism, Yang et al. synthesized porous carbon-coated ZnO quantum dots (~3.5 nm) via a controlled pyrolysis.[14] During this process, hydrocarbons, which can evolve from the cleavage of benzene rings, were not detected.
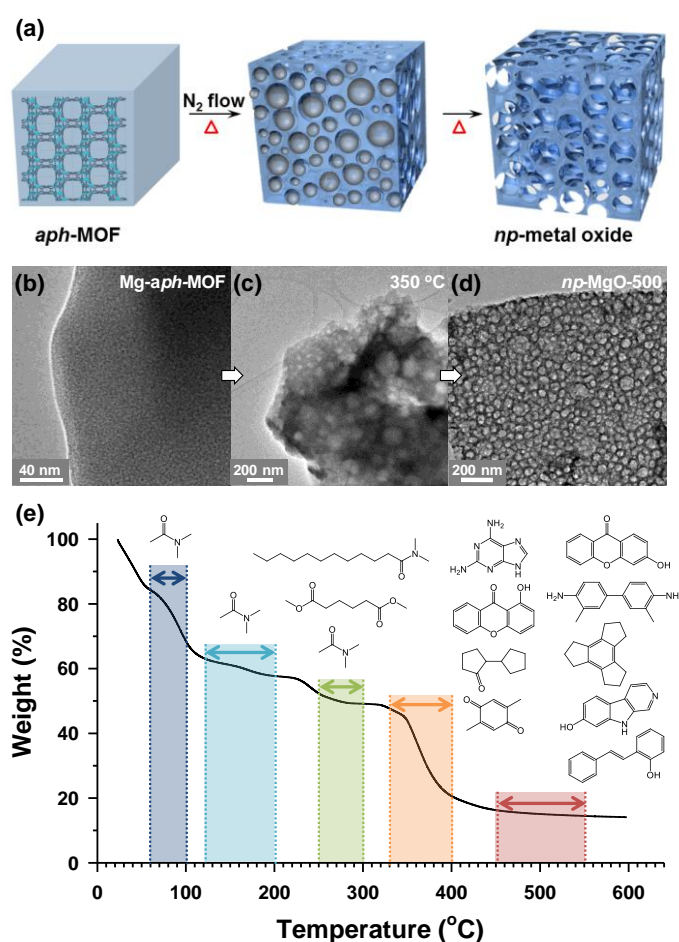
Figure 2.3. (a) Schematic view of the thermally induced conversion process of *aph*-MOF and (b−d) ex situ TEM images taken at various temperatures during heating. (e) TGA and pyro-GC/MS result of Mg-*aph*-MOF.

Paying attention to the robustness of the aromatic carboxylate, our group conversely employed aliphatic carboxylate ligands in a previous literature.[15] These ligands may construct less thermally stable aliphatic-ligand-based MOFs (*aph*-MOFs), and thus, a different thermal conversion route can be

expected. As schematically illustrated in Figure 2.3a, during the thermolysis of a Mg-*aph*-MOF under N_2 flow, before the structure was destroyed, labile adipate ligands were first transformed into organic moieties to act as pore-formers, which subsequently evaporated at higher temperatures. Ex situ transmission electron microscope (TEM) images recorded at each temperature during heating up to 500 °C support this conversion mechanism (Figure 2.3b−d). Specifically, at 350 °C, organic vesicles were distributed over the material, which indicates the generation and confinement of large amounts of organic moieties, and at the end of heat treatment at 500 °C, we obtained hierarchical nanoporous MgO (*np*-MgO). The pyrolysis−gas chromatography/mass spectrometry (pyro-GC/MS) results demonstrated how the organic substances were generated during thermolysis (Figure 2.3e). Many new organic species with high boiling points evolved in each temperature range. This process indicated that organic fragments that had decomposed from Mg-*aph*-MOF first reacted to generate new organic moieties, which were then confined in the solid until the temperature was sufficiently high to evaporate them.

References

1. M. Bosch, S. Yuan, W. Rutledge, H.-C. Zhou, *Acc. Chem. Res.* **2017**, *50*, 857−865.
2. M. P. Suh, Y. E. Cheon, E. Y. Lee, *Coord. Chem. Rev.* **2008**, *252*, 1007−1026.
3. W. Xia, A. Mahmood, R. Zou, Q. Xu, *Energy Environ. Sci.* **2015**, *8*, 1837−1866.
4. L. Oar-Arteta, T. Wezendonk, X. Sun, F. Kapteijn, J. Gascon, *Mater. Chem. Front.* **2017**, *1*, 1709−1745.
5. R. R. Salunkhe, Y. V. Kaneti, J. Kim, J. H. Kim, Y. Yamauchi, *Acc. Chem. Res.* **2016**, *49*, 2796−2806.
6. J. Tang, Y. Yamauchi, *Nat. Chem.* **2016**, *8*, 638−639.
7. S. R. Batten, N. R. Champness, X.-M. Chen, J. Garcia-Martinez, S. Kitagawa, L. Öhrström, M. O'Keeffe, M. P. Suh, J. Reedijk, *CrystEngComm* **2012**, *14*, 3001−3004.
8. M. Y. Masoomi, A. Morsali, *Coord. Chem. Rev.* **2012**, *256*, 2921−2943.
9. R. Bendi, V. Kumar, V. Bhavanasi, K. Parida, P. S. Lee, *Adv. Energy Mater.* **2016**, *6*, 1501833.
10. B. Y. Guan, L. Yu, X. Wang, S. Song, X. W. Lou, *Adv. Mater.* **2017**, *29*, 1605051.
11. L. Zhang, H. B. Wu, S. Madhavi, H. H. Hng, X. W. Lou, *J. Am. Chem. Soc.* **2012**, *134*, 17388−17391.
12. R. Das, P. Pachfule, R. Banerjee, P. Poddar, *Nanoscale* **2012**, *4*, 591−599.
13. L. Zhang, Y.H. Hu, *J. Phys. Chem. C* **2010**, *114*, 2566−2572.
14. S. J. Yang, T. Kim, J. H. Im, Y. S. Kim, K. Lee, *Chem. Mater.* **2012**, *24*, 464−470.
15. T. K. Kim, K. J. Lee, J. Y. Cheon, J. H. Lee, S. H. Joo, H. R. Moon, *J. Am. Chem. Soc.* **2013**, *135*, 8940−8946.

2.2. Transformative route to nanoporous metal oxides with identical textural properties

Introduction

Conversion reactions have been explored extensively with various types of precursors, and have enabled the synthesis of new materials with a high degree of compositional and structural complexity.[1-5] The versatility of conversion reactions can be exemplified in the preparation of thermodynamically unfavorable hollow nanoparticles from solid analogues by exploiting the nanoscale Kirkendall effect[6] or galvanic replacement reaction.[7] In the context of conversion reactions, MOFs can serve as excellent precursors, and accordingly, conversion reactions utilizing MOFs are currently being actively pursued.[9–12]
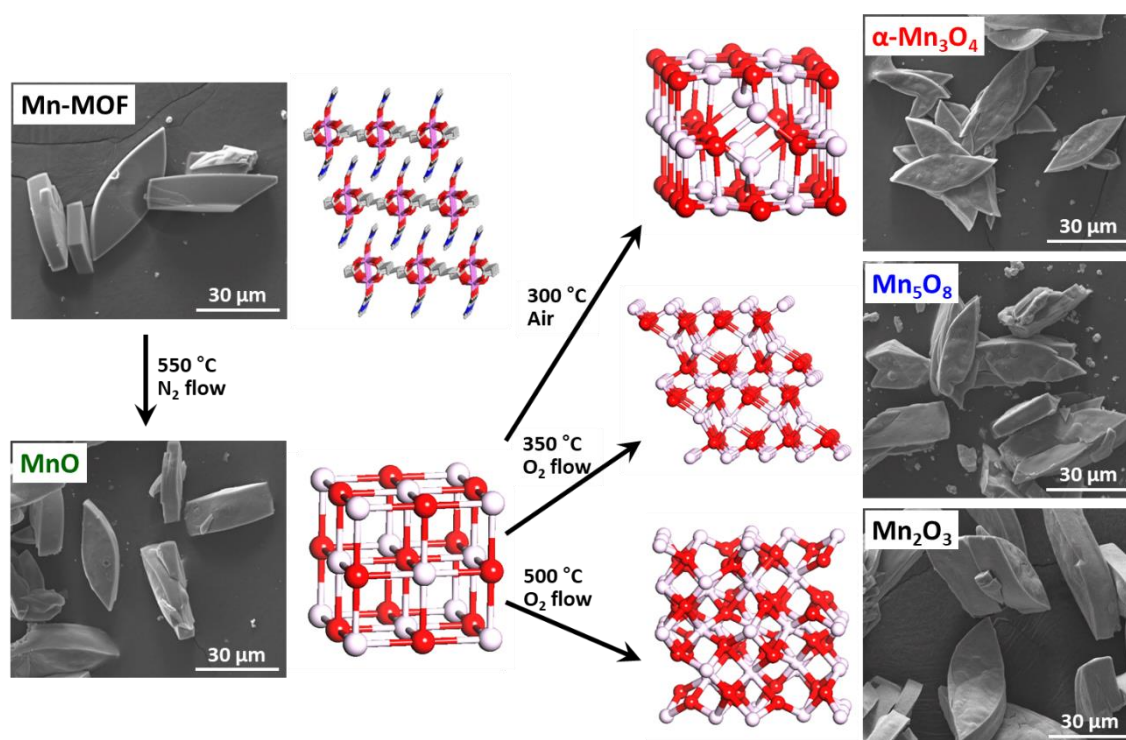
Figure 2.4. SEM images and atomic structures of Mn-MOF and converted manganese oxides during structural transformation of Mn-MOF into MnO, Mn_3O_4, Mn_5O_8 and Mn_2O_3.

In this chapter, we demonstrate that conversion reactions using MOFs as precursors can be successfully exploited to prepare nanoporous nanocrystalline metal oxides with tunable oxidation states. Manganese oxides were chosen as a model system because they can exist in various oxidation states[13] and are the centers of great interest in energy conversion and storage as well as catalysis.[14–17] We show that sequential conversion reactions are capable of transforming a Mn-based MOF (Mn-MOF) into nanoporous nanocrystalline manganese oxides with continuously tuned oxidation states, MnO, Mn_3O_4, Mn_5O_8, and Mn_2O_3, with conservation of the original morphology of the Mn-MOF crystals (Figure 2.4).

Importantly, these conversion reactions enabled the preparation of low-oxidation-state MnO and metastable intermediate Mn_5O_8 phases with nanoporous nanocrystalline architecture, which was previously difficult to access. Nanoporous MnO, Mn_3O_4, and Mn_5O_8 have almost identical textural properties, including their morphology, surface areas, pore volumes, and the size of nanocrystals composing nanoporous frameworks. The textural similarity among the series of manganese oxides allowed them to be used as a system for studying the oxidation-state effect in catalysis; previous studies related to such an effect were mostly performed with a series of catalysts possessing various other variables that can affect catalytic performances.[18-21] We investigated the electrocatalytic activity of these nanoporous manganese oxides for the oxygen reduction reaction (ORR), and observed oxidation-state-dependent catalytic activity and kinetics in the ORR
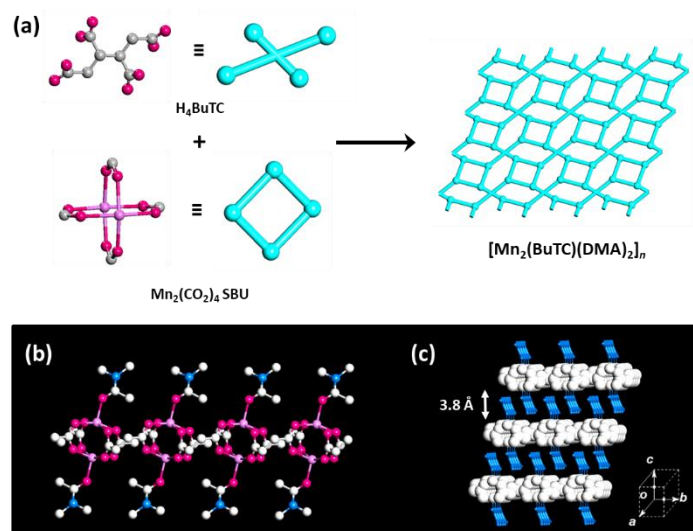
Figure 2.5. Synthesis and single-crystal X-ray structure of Mn-MOF. (a) Synthetic scheme of Mn-MOF. (b) Side view of one layer of Mn-MOF. Hydrogen atoms and guest molecules are omitted for clarity (color scheme: C, white; O, purple; N, light blue; Mn, pink). (c) Entire structure of Mn-MOF (color scheme: 2-D layer, white; coordinating DMA, blue).

Experimental section

All chemicals and solvents were of reagent grade and used without further purification. *meso*-Butane-1,2,3,4-tetracarboxylic acid (H$_4$BuTC, >98%), and *N,N*-dimethylacetamide (DMA, >99%) were supplied by TCI. Mn(NO$_3$)$_2$·4H$_2$O (>97%) was purchased from Aldrich.

Synthesis of Mn-MOF ([Mn$_2$(BuTC)(DMA)$_2$]$_n$). H$_4$BuTC (0.037 g, 0.16 mmol) was dissolved in DMA (2.5 mL), and mixed with a DMA (2.5 mL) solution of Mn(NO$_3$)$_2$·4H$_2$O (0.080 g, 0.32 mmol). The solution was sealed in a glass jar, heated to 100 ℃ for 24 h, and then cooled to room temperature. Yellowish leaf-shaped crystals formed, which were filtered and washed briefly with the mother liquor.

Yield: 35%. FT-IR (Nujol mull): $\nu_{C=O}$(DMA), 1652 (s); $\nu_{O-C=O}$, 1615, 1418 (s) cm^{-1}. Anal. Calcd for Mn$_2$C$_{16}$H$_{24}$O$_{10}$N$_2$: C, 37.37; H, 4.70; N, 5.45. Found: C, 37.53; H, 4.59; N, 5.44.

Synthesis of MnO. Solid Mn-MOF was heated at 5 °C min^{-1} under a nitrogen flow of 60 mL min^{-1}. After reaching the target temperature of 550 °C, the material was maintained at that temperature for 12 h. After cooling to room temperature, black solid was obtained.

Synthesis of Mn$_3$O$_4$. As-synthesized MnO solid was heated in a box furnace (ambient air environment) at 5 °C min^{-1}. After reaching the target temperature of 300 °C, the material was maintained at that temperature for 2 h. After cooling to room temperature, brownish solid was obtained.

Synthesis of Mn$_5$O$_8$. As-synthesized MnO solid was heated at 1 °C min^{-1} under an oxygen flow of 100 mL min^{-1}. After reaching the target temperature of 350 °C, the material was maintained at that temperature for 2 h. After cooling to room temperature, blackish solid was obtained.

Synthesis of Mn$_2$O$_3$. As-synthesized MnO was heated at 1 °C min^{-1} under an oxygen flow of 100 mL min^{-1}. After reaching the target temperature of 500 °C, the material was maintained at that temperature for 2 h. After cooling to room temperature, dark grey powder was obtained.

Single-crystal X-ray crystallography. A single-crystal of Mn-MOF was coated with paratone-*N* oil, and the diffraction data were measured at 100 K with synchrotron radiation (λ = 0.69999 Å) on an ADSC Quantum-210 detector at 2D SMC with a silicon (111) double crystal monochromator (DCM) at the Pohang Accelerator Laboratory, Republic of Korea. The ADSC Q210 ADX program[41] was used for data collection, and HKL3000sm (Ver. 703r)[42] was used for cell refinement, reduction, and absorption correction. The crystal structures were solved by direct methods and refined by full-matrix least-squares calculations with the SHELX-97 computer program.[43] The positions of all non−hydrogen atoms were refined with anisotropic displacement factors. The hydrogen atoms were positioned geometrically using a riding model.

Characterization methods. All characterizations were carried out at the Ulsan National Institute of Science and Technology (UNIST) Central Research Facilities (UCRF) Center. Infrared spectra were recorded with a ThermoFisher Scientific iS10 FT-IR spectrometer. Elemental analyses (for C, H, N, S, and O) were performed by using a Thermo Scientific Flash 2000 series CHNS/O analyzer. Thermogravimetric analyses (TGA) were performed under nitrogen gas at a scan rate of 5 °C min^{-1}, using a TGA Q50 from TA Instruments. X-ray photoelectron spectroscopy (XPS) was performed on a K-alpha from Thermo Fisher. X-ray powder diffraction (XRPD) data were recorded on a Bruker D8 advance diffractometer at 40 kV and 40 mA and a Bruker D2 phaser diffractometer at 30 kV and 10 mA for Cu Kα (λ = 1.541 Å), with a step size of 0.02° in 2θ. Scanning electron microscope (SEM) images were taken using a Quanta 200 microscope (FEI) operating at 18 kV. Transmission electron microscope (TEM) images and energy dispersive X-ray spectra were obtained with a JEOL JEM-2100F microscope. The nitrogen adsorption−desorption isotherms were measured at 77 K using liquid nitrogen on a BELSORP-MAX. Prior to the adsorption measurement, the samples were evacuated at 200 °C

under vacuum (p < 10^{-5} mbar) overnight. The specific surface area was determined in the relative pressure range from 0.05 to 0.3 of the Brunauer−Emmett−Teller (BET) plot, and the total pore volume was calculated from the amount adsorbed at a relative pressure of about 0.98−0.99. Pore size distribution curves were obtained from the corresponding isotherms using the Barrett-Joyner-Halenda (BJH) method.

Electrochemical measurements. Electrochemical characterization of the samples was carried out using an IviumStat electrochemical analyzer. The electrochemical experiments were performed at room temperature (25 °C) and under atmospheric pressure using a three-compartment electrochemical cell. A graphite counter electrode and Hg/HgO reference electrode (XR400, Radiometer Analytical) with 1 M KOH (99.999%, Aldrich) filling solution were used. The Hg/HgO reference electrode was calibrated with respect to the reversible hydrogen electrode (RHE) before use. For this purpose, Pt wires were used as both the working electrode and counter electrode, and the potential cycle between −0.93 V and −0.87 V (vs. Hg/HgO) was applied with a scan rate of 1 mV s^{-1} in H_2-saturated 0.1 M KOH solution. The resulting potential−current (*V−I*) curve after averaging the anodic and cathodic currents gave a result of **E(RHE) = E(Hg/HgO) + 0.887 V**. All potentials in this report were reported in the RHE scale. For ORR performance measurement, a rotating ring disk electrode (RRDE) with a glassy carbon disk (GC, 4 mm in diameter) and a Pt ring (5 mm in inner diameter and 7 mm in outer diameter) was used as a working electrode (ALS, Cat. No. 012613). The RRDE was polished with 1.0 and 0.3 μm alumina suspensions to generate a mirror finish. For preparation of a catalyst ink, Nafion (5 wt% in isopropyl alcohol (IPA), Aldrich) was neutralized by 0.1 M NaOH (99.99%, Aldrich) at a volume ratio of Nafion : 0.1 M NaOH = 2 : 1 in order to prevent oxide passivation.[41] Commercial carbon black (Vulcan XC-72R) was added to the catalyst ink to overcome the low electrical conductivity of oxides. The catalyst ink was prepared by mixing 5 mg of catalyst, 12 mg of Vulcan, 116 μL of neutralized Nafion, 100 μL of deionized water, and 0.98 mL of IPA (>99.9%, Aldrich) with ultra-sonication for at least 30 min. 3 μL of the catalyst ink was deposited onto the GC electrode with a micro-syringe. The resulting catalyst loading was 0.1 mg$_{oxide}$ cm^{-2}. Prior to the electrochemical measurements, a potential cycle from 0.7 to 1.0 V was applied in a N_2-saturated 0.1 M KOH for 50 cycles at a scan rate of 100 mV s^{-1} for electrochemical cleaning. Subsequently, the cyclic voltammogram was obtained under the same condition used for electrochemical cleaning, except for the change in the scan rate of 20 mV s^{-1} for 3 cycles. Linear sweep voltammetry (LSV) curves for the ORR were obtained by cycling the potential from 1.1 to 0.2 V in an O_2-saturated 0.1 M KOH solution with O_2 purging at different rotating speeds. The anodic and cathodic sweeps for the ORR were averaged in order to correct the capacitive-current contribution.[41] The ORR measurement was independently repeated three times, and the averaged currents were used.

For the evaluation of four-electron selectivity, the potential of the Pt ring was fixed at 1.3 V (vs. RHE) during LSV scans for the ORR. The number of electrons transferred was calculated by the following equation:

$$n = \frac{4}{1 + \frac{I_R}{N \times I_D}}$$

Here, I_D, I_R, and N are the disk current, the ring current and the collection coefficient, respectively. The value of N was measured in 1 M KNO_3 + 2 mM $K_3Fe(CN)_6$ at a rotating speed of 1000 rpm, and was determined to be 0.47.

The four-electron selectivity was also assessed by Koutecký-Levich equation:

$$\frac{1}{I} = \frac{1}{I_K} + \frac{1}{I_L} = \frac{1}{I_K} - \frac{1}{0.62nFAD_O^{2/3}v^{-1/6}C_O\omega^{1/2}}$$

Here, I, I_L and I_K are the measured current, the diffusion-limited current and the kinetic current, respectively. F is the Faraday constant. ($9.65 \times 10^7\ mA\ s\ mol^{-1}$), A is the GC disk area. ($0.126\ cm^2$), D_O is the diffusion coefficient of O_2 in 0.1 M KOH solution ($1.9 \times 10^{-5}\ cm^2\ s^{-1}$), v is the kinematic viscosity of 0.1 M KOH. ($0.01\ cm^2\ s^{-1}$), C_O is the concentration of O_2 in 0.1 M KOH. ($1.2 \times 10^{-6}\ mol\ cm^{-3}$), and ω is the rotation speed of the unit in radian per second.[42-44]

Before electrochemical impedance spectroscopy (EIS) measurement, the potential was cycled from 0.7 to 1.0 V for 50 cycles in N_2-saturated 0.1 M KOH solution. Then, impedance spectra were obtained in O_2-saturated 0.1 M KOH at the fixed potential of 0.7 V (vs. RHE) in the frequency range varying from 10 kHz to 0.05 Hz.

Results and discussion

We began with the synthesis of the Mn-MOF precursor. A solvothermal reaction of $Mn(NO_3)_2 \cdot 4H_2O$ and aliphatic ligand, *meso*-butane-1,2,3,4-tetracarboxylic acid (H_4BuTC), in *N,N*-dimethylacetamide (DMA) solvent at 100 °C for 24 h afforded yellowish leaf-shaped crystals of $[Mn_2(BuTC)(DMA)_2]_n$ (Figure 2.4 and 2.5). Single-crystal X-ray crystallographic data[22] (Figure 2.5) revealed that Mn-MOF is constructed with $Mn_2(COO)_4$ paddle-wheel clusters as secondary building units interconnected by the BuTC ligand to form a 2-dimensional layer. In the Mn-MOF, each Mn^{II} ion is coordinated with four oxygen atoms of four different BuTC ligands in the equatorial positions and an oxygen atom of a DMA molecule at the axial position to show a square-pyramidal coordination geometry. Four carboxylate groups of four different BuTC ligands bridge between the two Mn^{II} centers in a *syn–syn* bidentate mode, forming a paddle-wheel shaped SBU. The Mn–Mn distance in a SBU is 3.051(1) Å. Each $BuTC^{4-}$ acts as a tetrabidentate bridging ligand by coordinating to eight different Mn^{II} centers. The shortest interlayer distance is 3.8 Å, based on the van der Waals radii. The X-ray powder

pattern (XRPD) pattern of $[Mn_2(BuTC)(DMA)_2]_n$ showed good agreement with the simulated pattern (Figure 2.6a). In the TGA trace of the as-synthesized Mn-MOF in a N_2 atmosphere (Figure 2.6b), the two coordinating DMA molecules per formula ($[Mn_2(BuTC)(DMA)_2]_n$) were removed over the range 200–300 ℃, and decomposition of Mn-MOF ensued above ~400 ℃.
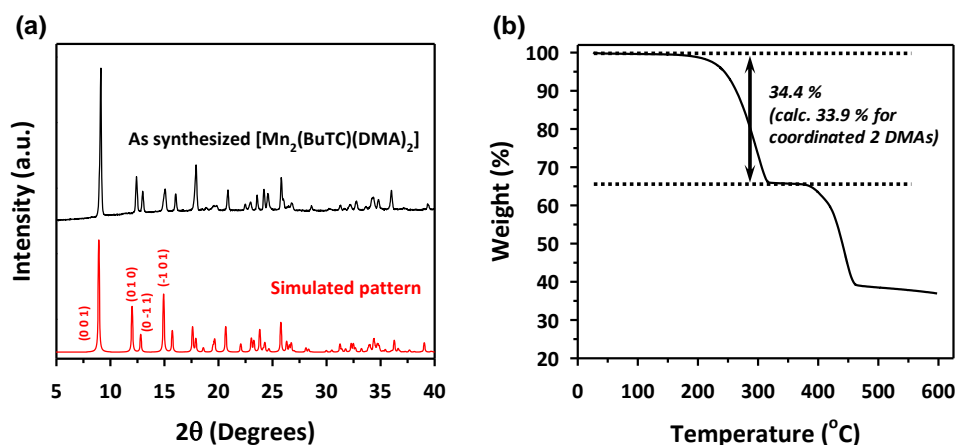
Figure 2.6. (a) Experimental and simulated XRPD patterns and (b) TGA trace of Mn-MOF.

We explored the conversion reactions of Mn-MOF into manganese oxides. Based on the above TGA result, we first heated as-synthesized Mn-MOF under N_2 flow to 550 ℃ and maintained this temperature for 12 h to achieve complete thermal decomposition of the MOF structure (refer to the experimental section). Scanning electron microscope (SEM) images of pristine Mn-MOF and converted black powder revealed a pseudomorphic conversion process (Figure 2.4). The converted material was nanoporous, as its cross-sectional SEM and TEM images (Figure 2.7a and d) clearly showed the macropores and mesopores, respectively. The TEM image revealed that the frameworks of the converted material were composed of small nanoparticles of ~5 nm. A high-resolution (HR) TEM image of this material (Figure 2.7d, inset) exhibited distinct lattice fringes indicating the highly crystalline nature of these nanoparticles. The XRPD pattern of the converted material identifies its structure as single-phase cubic manganosite (MnO), which is coincident with JCPDS no. 71-4748 (Figure 2.8, bottom). The cubic MnO phase could be confirmed by its electron diffraction pattern (Figure 2.7d, inset) as well. The crystalline size of MnO nanoparticles, calculated by applying the Scherrer equation to the (200) reflection, was 5.0 nm in diameter. The elemental analysis revealed that the nanoporous MnO contained residual carbon (18 wt%) and nitrogen (0.6 wt%).
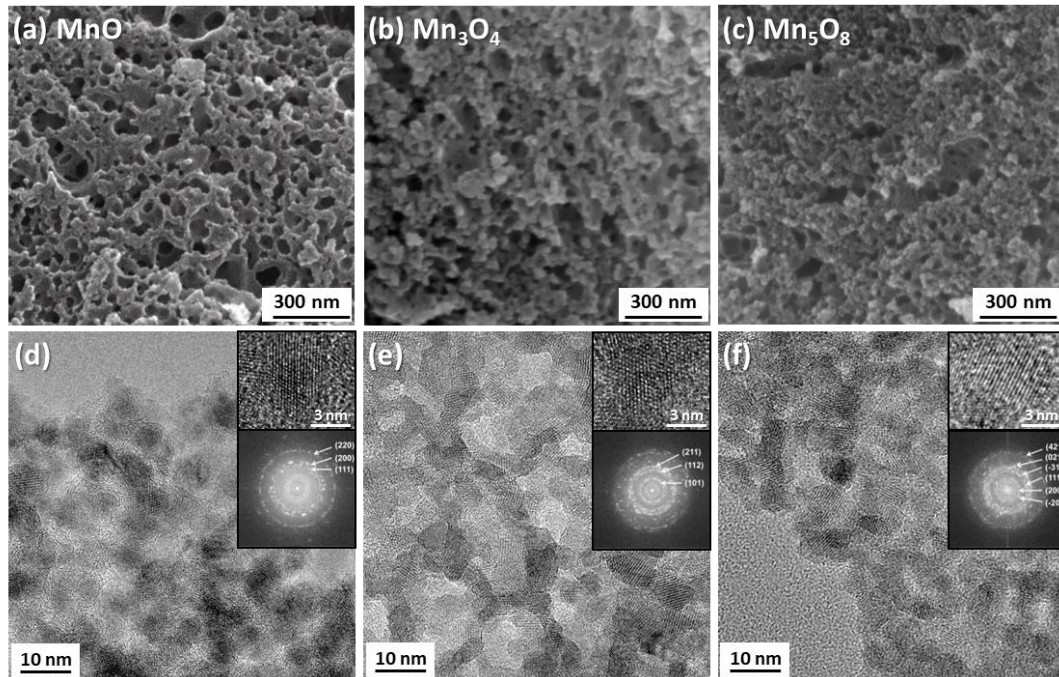
Figure 2.7. Characterization of converted manganese oxides. (a–c) SEM images, (d–f) TEM images, and (d–f, insets) HR-TEM images and electron diffraction patterns of nanoporous MnO (a and d), Mn_3O_4 (b and e), and Mn_5O_8 (c and f).
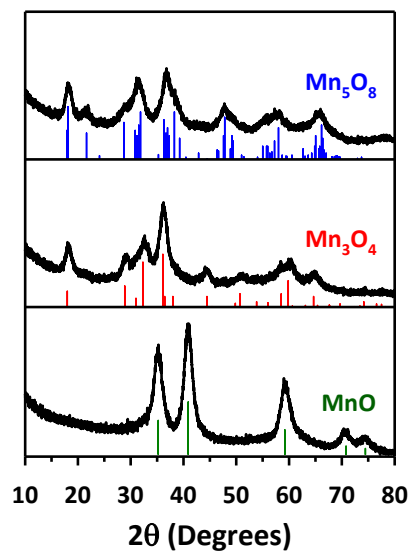
Figure 2.8. XRPD patterns of converted manganese oxides.

Using the nanoporous MnO that has the lowest oxidation state among the manganese oxide structures as a precursor, we further carried out sequential conversion reactions in an oxidizing environment to generate manganese oxides with higher oxidation states. First, nanoporous MnO was heated in ambient air. The XRPD patterns monitored at incremental heating temperatures (Figure 2.9a) indicated that the transformation of cubic MnO into tetragonal spinel-phase hausmannite-Mn_3O_4

(JCPDS no. 24-0734, hereafter Mn_3O_4) started at 100 °C, and the latter phase was maintained up to 300 °C. At 350 °C, several new peaks started to appear in the XRPD pattern, which correspond to bixbyite Mn_2O_3 (JCPDS no. 73-1826). Further heating to ≥450 °C yielded the pure phase of Mn_2O_3. Meanwhile, conversion reactions in a more oxidative environment allowed for the stabilization of metastable intermediate Mn_5O_8; we found that the nanoporous MnO can be transformed into a pure, layered Mn_5O_8 phase by way of the Mn_3O_4 phase, when it was heated to 350 °C under oxygen flow at a very slow ramping rate of 1 °C min^{-1} (Figure 2.9b and c). The heating of MnO to the same temperature but with higher ramping rates (3 or 5 °C min^{-1}) afforded a mixture of Mn_3O_4 and Mn_5O_8 phases instead of the sequential formation of pure Mn_3O_4 and Mn_5O_8 phases (Figure 2.9c). Hence, the degree of oxidation environment and the change of heating rate can adjust oxidation states and purities of the resultant manganese oxides.
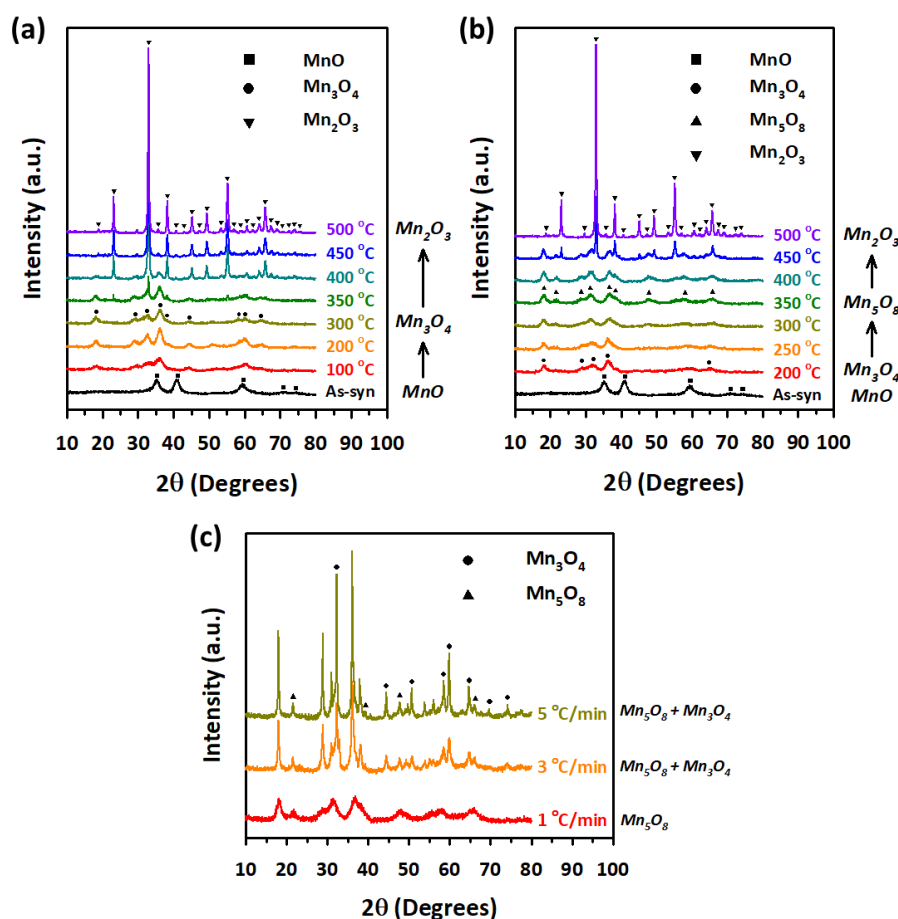
Figure 2.9. Monitoring structural transformations from MnO to manganese oxides with higher oxidation numbers. XRPD patterns for MnO before and after heat treatment at various temperatures (a) in a box furnace with a ramping rate of 5 °C min^{-1} and (b) in a tube furnace under an oxygen flow of 100 mL min1 with a ramping rate of 1 °C min^{-1}. (c) XRPD patterns of MnO after heat treatment at 350 °C in a tube furnace under an oxygen flow of 100 mL min^{-1} and with different ramping rates of 1 °C min^{-1}, 3 °C min^{-1}, and 5 °C min^{-1}.

Under the optimized experimental conditions based on the above experiments, we could obtain Mn_3O_4 and Mn_5O_8 in pure phases via pseudomorphic transformation of nanoporous MnO (Figure 2.4). Further examination of these two manganese oxides with cross-sectional SEM and TEM images (Figure 2.7b, c, e and f) revealed that the nanoporous structure of MnO was retained despite the structural transformation processes. The crystalline sizes of Mn_3O_4 and Mn_5O_8, calculated by applying the Scherrer equation to the (101) and (201) reflections of their XRPD patterns (Figure 2.8), respectively, were 5.6 nm and 5.2 nm, similar to those of MnO. The crystallinity and pure phases of nanoporous Mn_3O_4 and Mn_5O_8 were also confirmed by their HR-TEM images and electron diffraction patterns (Figure 2.7e and f, insets), respectively. However, Mn_2O_3 showed a marked increase in the nanocrystal size, from 5.0 to ~20 nm, regardless of the reaction conditions such as the gas environment or heating rate (Figure 2.9a and b, and 2.10). Hereafter, we will focus on the three phases—MnO, Mn_3O_4, and Mn_5O_8—that have almost identical textural properties, for further discussion of the converted manganese oxides.
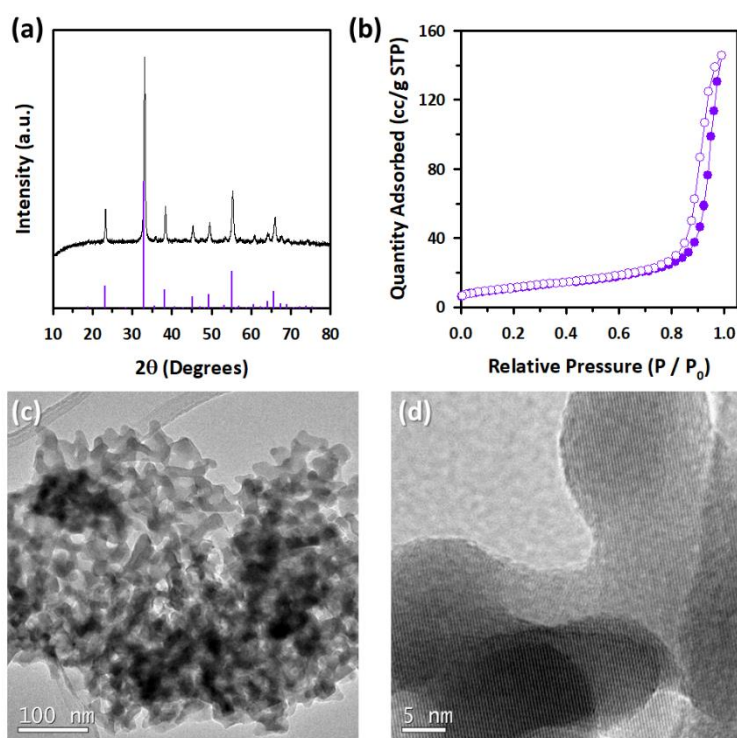
Figure 2.10. Characterization of an Mn_2O_3 sample: (a) XRPD pattern, (b) nitrogen adsorption−desorption isotherms, and (c,d) TEM images.

Figure 2.11a shows the nitrogen adsorption–desorption isotherms of the three manganese oxides, which feature type IV isotherms with H3-type hysteresis loops over all three samples, indicating well-developed mesoporosity. The highly porous nature of the three nanoporous manganese oxides provide similarly large Brunauer–Emmett–Teller (BET) surface areas (~145 m^2 g^{-1}) and pore volumes (~0.3

cm^3 g^{-1}). The pore size distribution curves obtained by the BJH method exhibited similar pores sizes (5 to 20 nm) of manganese oxides (Figure 2.12). The detailed textural data are summarized in Table 2.1. While the N_2 adsorption data reveal similar porous properties of the three manganese oxides, the X-ray photoelectron spectroscopy (XPS) data clearly establish a marked difference in their oxidation states (Figure 2.11b and Table 2.2). The Mn 3s XPS spectra (Figure 2.11b) revealed that the position of the lower binding energy peak gradually shifted to higher energy with the increase in the oxidation number of the sample (MnO / Mn_3O_4 / Mn_5O_8), which is consistent with previous results.[23-25] This systematic peak shift results in a corresponding decrease in the 3s multiplet splitting (ΔE_{3s}) of these manganese oxides (Table 2.2)
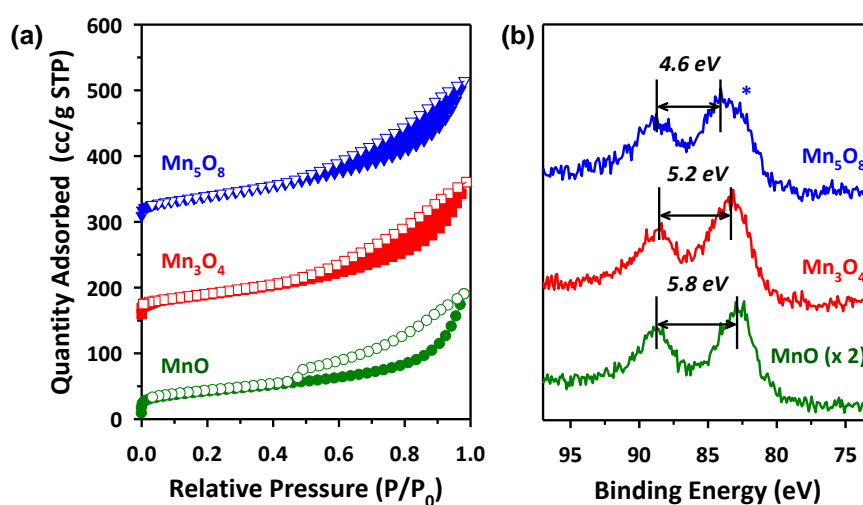
Figure 2.11. (a) Nitrogen adsorption–desorption isotherms and (b) Mn 3s XPS spectra of converted manganese oxides. The blue asterisk indicates the presence of low-valent (e.g. Mn^{2+}) manganese species in Mn_5O_8.
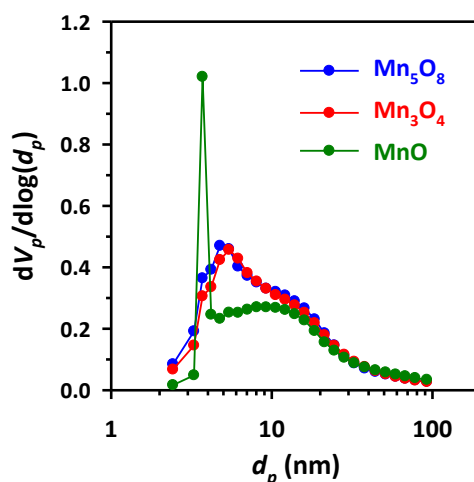
Figure 2.12. Pore size distribution of the nanoporous manganese oxides obtained by BJH method from desorption branch of N_2 physisorption isotherm.

Table 2.1. BET surface areas and total pore volumes obtained from nitrogen adsorption analysis, and the nanocrystalline sizes of nanoparticles composing frameworks of manganese oxides.

Sample	BET surface area[a] ($m^2\ g^{-1}$)	Pore volume[b] ($cm^3\ g^{-1}$)	Nanocrystalline size[c] (nm)
MnO	146	0.29	5.0
Mn_3O_4	144	0.33	5.6
Mn_5O_8	147	0.33	5.2
Mn_2O_3	39	0.22	20

[a] BET surface area was obtained in the relative pressure range of 0.05-0.3.

[b] Pore volume was calculated at the relative pressure of 0.98-0.99.

[c] Nanocrystalline size was calculated by applying the Scherrer equation to the proper reflection of XRPD patterns.

Table 2.2. The peak positions and multiplet splittings deduced from Mn 2p and 3s XPS analyses.

Sample	$3s^a$ (eV)	$3s^b$ (eV)	$\Delta E_{3s}{}^c$
MnO	82.9	88.7	5.8
Mn_3O_4	83.4	88.6	5.2
Mn_5O_8	84.1	88.7	4.6

[a, b] Peaks at lower and higher binding energies, respectively

[c] Multiplet splitting values between the peaks for lower and higher BEs were obtained from the fitted XPS spectra.

Nanoporous manganese oxides thus far reported have been predominantly limited to those with high oxidation states such as MnO_2 and Mn_2O_3.[26-33] Toward the low-oxidation-state manganese oxide, Bruce et al. prepared nanoporous Mn_3O_4 by reducing pre-synthesized nanoporous Mn_2O_3 with hydrogen gas.[33] Likewise, other nanoporous metal oxides with low oxidation states, for instance, CoO and Fe_3O_4, could be prepared by the reduction of the corresponding metal oxides with higher oxidation numbers.[34,35] In contrast, in our approach, the oxidative conversion reactions of Mn-MOF could sequentially generate nanoporous MnO, Mn_3O_4, Mn_5O_8, and Mn_2O_3, by progressively increasing the degree of oxidation. Significantly, our MOF-driven route enabled the isolation of the low-oxidation-state MnO and metastable intermediate Mn_5O_8 as pure phases with nanoporous nanocrystalline structures, which were previously rarely attainable.[36,37] In particular, to our knowledge, nanoporous Mn_5O_8 with such a large surface area and well-developed porosity is prepared for the first time.

We note that the transformations between different structures, from cubic (MnO) to spinel (Mn_3O_4), and to layered (Mn_5O_8), occurred while preserving a nanoporous structure and textural properties. As demonstrated in our previous work,[11] the conversion reactions exploiting aliphatic ligand-based MOFs

allow for the formation of thermally stable nanoporous metal oxide frameworks that are composed of small nanoparticles. In this approach, labile aliphatic ligands can act as self-templates during the thermal conversion process, and finally evaporate to generate nanopores. We also found that the infinite coordination between inorganic and organic moieties in the MOFs is critical for suppressing the aggregation of metallic entities into large particles; instead, the thermal conversion of a single coordination compound generated very large agglomerates.[12] In this way, the prepared nanoporous manganese oxide frameworks are constructed with small (~5 nm) manganese oxide nanoparticles, which have a high density of defects or grain boundaries. Compared to bulk metal oxides, nanometer scale manganese oxide nanoparticles could relieve or minimize the structural stress during the transformations between different structures, which could lead to a minimal change in their textural properties.
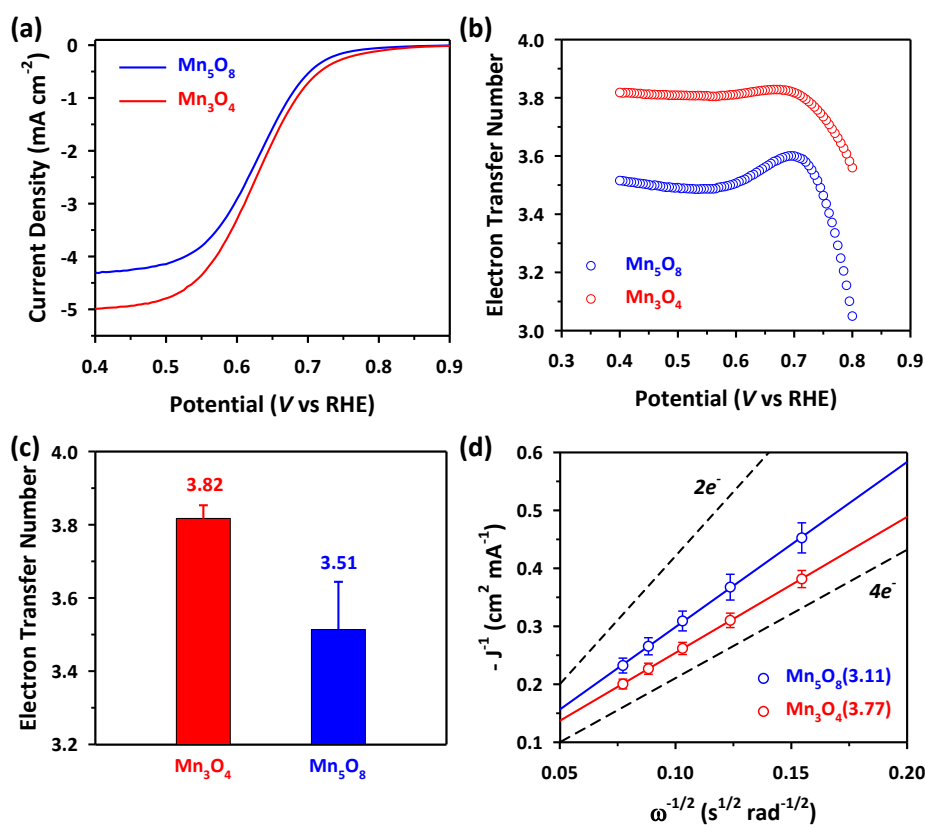
Figure. 2.13. Electrocatalytic activity of series of nanoporous manganese oxides for the ORR. (a) LSV curves of nanoporous manganese oxides on glassy carbon electrodes. (b) The numbers of electrons transferred at 0.4 V (vs. RHE) during the ORR obtained from the RRDE measurements. (c) Plot of the number of transferred electrons against potential during the ORR obtained by RRDE measurement. (d) Koutecký-Levich plots at 0.4 V (vs. RHE). The dotted lines show the theoretical slopes when two and four electrons are transferred during ORR. The numbers in the parentheses indicate the number of transferred electrons.

Among the transformed nanoporous manganese oxides, Mn_3O_4 and Mn_5O_8 have nearly identical textural properties (such as morphology, surface area, and crystallite size of framework nanoparticles) and are free of residual carbon, but differ only in their oxidation states. As such, these two manganese oxides can serve as a system for the study of the oxidation state effect in catalysis. We investigated the electrocatalytic properties of the two nanoporous manganese oxides for the ORR (Figures 2.13, 2.14, and 2.15), because the latter is a key reaction in energy conversion devices such as fuel cells and metal–air batteries. The LSV curves for the two nanoporous manganese oxides (Figure 2.13a), measured in 0.1 M KOH electrolyte at a rotating speed of 1600 rpm revealed that the nanoporous Mn_3O_4 had higher on-set potential (0.75 V vs. RHE) and current density at 0.75 V (-0.26 mA cm^{-2}) than those of Mn_5O_8 (0.73 V and -0.15 mA cm^{-2}, respectively). In addition, nanoporous Mn_3O_4 showed a higher limiting current density than Mn_5O_8. We note that nanoporous MnO showed higher current density than the other oxides in the kinetic-diffusion controlled region of the LSV curve (Figure 2.16). This result does not correspond to the previous report where MnO exhibited inferior ORR activity to Mn_3O_4.[38] We attribute this higher activity of the nanoporous MnO to the presence of residual carbon and nitrogen. The kinetic parameters of the two catalysts for the ORR were deduced by measurement of the ring currents during the ORR (Figure 2.13b and c) and the Koutecký-Levich analyses (Figure 2.13d and 2.14). Results from both the methods consistently indicated that the electron numbers transferred by the nanoporous Mn_3O_4 were higher (3.8) than Mn_5O_8 (3.1~3.5). The excellent kinetics observed for nanoporous Mn_3O_4 could also be confirmed with its smaller charge transfer resistance at 0.7 V in EIS data (Figure 2.15).
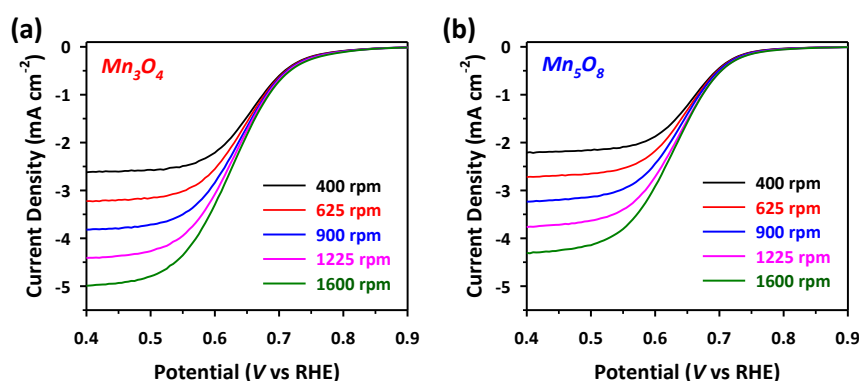
Figure 2.14. LSV polarization curves for the ORR measured at different rotating rates: (a) nanoporous Mn_3O_4, and (b) nanoporous Mn_5O_8.

Collectively, nanoporous Mn_3O_4 had higher diffusion-limited current, electron transfer number, and lower charge transfer resistance than those of Mn_5O_8. For the ORR in alkaline electrolyte, the most efficient way is direct four electron transfer mechanism, which is, however, kinetically impeded due to its high activation barrier. Instead, two-step mechanism is favored, wherein oxygen is first reduced via

two electron pathway producing peroxide species (HO_2^-) and the catalytic decomposition of HO_2^- produces half of oxygen molecule that is further reduced. Importantly, rapidly repeated the latter cycles lead to quasi-four-electron transfer mechanism. Comparing the oxidation state of the two manganese oxides, spinel Mn_3O_4 structure consists of Mn cations with +2 and +3 oxidation numbers, whereas layered Mn_5O_8 has +2 and +4 oxidation states. The decomposition of HO_2^- can be facilitated by facile redox mechanism between +2 and +3 Mn cations on the surface of Mn_3O_4 structure.[39] Such enhanced HO_2^- decomposition results in quasi-four-electron transfer with nanoporous Mn_3O_4. It is suggested that the disparity in framework structure between Mn_3O_4 and Mn_5O_8 could also contribute to the difference in their ORR activity. Layered Mn_5O_8 is constructed with dense frameworks, which can impede facile adsorption of oxygen molecules. In contrast, spinel Mn_3O_4 with relatively opened framework is favorable for oxygen adsorption, thus expediting catalytic cycles. Likewise, a recent study revealed that among a series of calcium manganese oxides, $Ca_2Mn_3O_8$ that has analogous crystal structure to Mn_5O_8 thus exhibited lowest ORR activity.[65]

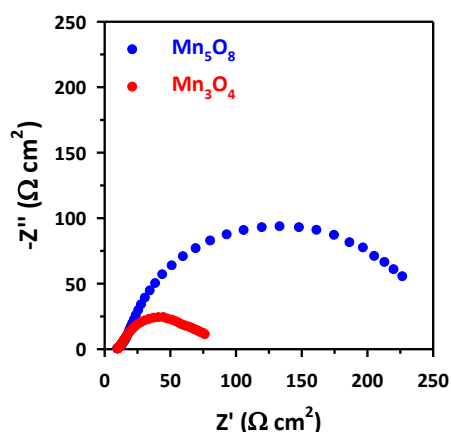**Figure 2.15.** Nyquist plots of the manganese oxide samples obtained by impedance spectra at a fixed potential of 0.7 V (vs. RHE) in O_2-saturated 0.1 M KOH.
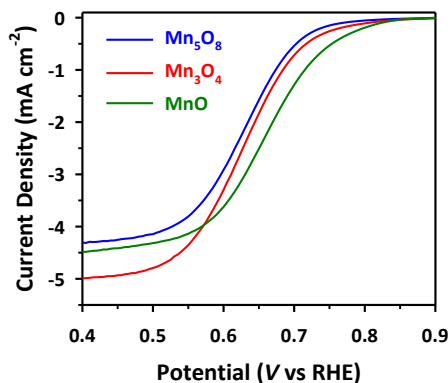

Figure 2.16. LSV polarization curves for the nanoporous Mn_5O_8, Mn_3O_4, and MnO measured at 1600 rpm in O_2-saturated 0.1 M KOH.

Conclusion

In summary, conversion reactions using Mn-MOF precursor yielded a series of nanoporous manganese oxide structures via sequential transformations. Significantly, this transformative route allowed for the preparation of low-oxidation-state (MnO) and metastable intermediate (Mn_5O_8) phases while having nanoporous architecture, which were otherwise difficult to synthesize. Additionally, this method enabled facile structural transformations between different manganese oxide structures while preserving their structural properties. In comparative investigation of the electrocatalytic activity of nanoporous manganese oxides, Mn_3O_4 showed better ORR activity and kinetics than nanoporous Mn_5O_8, demonstrating an important role of oxidation state for enhanced performance for the ORR.

Based on our previous work,[11] conversion reactions exploiting aliphatic ligand-based MOFs have been demonstrated as a versatile route to nanoporous metal oxides with nanocrystalline frameworks. This work, in particular, has shown that this transformative route can enable the preparation of nanoporous architectures with unexplored compositions. We envisage that further investigations into the MOF-driven conversion reactions can enrich the composition, structure, and function of nanoporous metal oxide materials.

References

1. Y. Vasquez, A. E. Henkes, J. C. Bauer, R. E. Schaak, *J. Solid State Chem.* **2008**, *181*, 1509–1523.
2. M. Kim, V. N. Phan, K. Lee, *CrystEngComm* **2012**, *14*, 7535–7548.
3. B. J. Beberwyck, Y. Surendranath, A. P. Alivisatos, *J. Phys. Chem. C* **2013**, *117*, 19759–19770.
4. W. Wang, M. Dahl, Y. Yin, *Chem. Mater.* **2013**, *25*, 1179–1189.
5. J. H. Han, S. Lee, J. Cheon, *Chem. Soc. Rev.* **2013**, *42*, 2581–2591.
6. Y. Yin, R. M. Rioux, C. K. Erdonmez, S. Hughes, G. A. Somorjai, A. P. Alivisatos, *Science* **2004**, *304*, 711–714.
7. Y. Sun, Y. Xia, *Science* **2002**, *298*, 2176–2179.
8. L. Zhang, H. B. Wu, S. Madhavi, H. H. Hng, X. W. Lou, *J. Am. Chem. Soc.* **2012**, *134*, 17388–17391.
9. M. Hu, A. A. Belik, M. Imura, Y. Yamauchi, *J. Am. Chem. Soc.* **2013**, *135*, 384–391.
10. A. S. Hall, A. Kondo, K. Maeda, T. E. Mallouk, *J. Am. Chem. Soc.* **2013**, *135*, 16276–16279.
11. T. K. Kim, K. J. Lee, J. Y. Cheon, J. H. Lee, S. H. Joo, H. R. Moon, *J. Am. Chem. Soc.* **2013**, *135*, 8940–8946.
12. L. Guo, H. Arafune, N. Teramae, *Langmuir* **2013**, *29*, 4404–4412.
13. A. H. Reidies, *Manganese Compounds, in Ullmann's Encyclopedia of Industrial Chemistry* **2002**, Wiley-VCH, Weinheim, ed. 6, vol. 20, pp. 543–564.
14. H. Wang, L.-F. Cui, Y. Yang, H. S. Casalongue, J. T. Robinson, Y. Liang, Y. Cui, H. Dai, *J. Am. Chem. Soc.* **2010**, *132*, 13978–13980.
15. J.-S. Lee, G. S. Park, H. I. Lee, S. T. Kim, R. Cao, M. Liu, J. Cho, *Nano Lett.* **2011**, *11*, 5362–5366.
16. W. Wei, X. Cui, W. Chen, D. G. Ivey, *Chem. Soc. Rev.* **2011**, *40*, 1697–1721.
17. F. Jiao, H. Frei, *Chem. Commun.* **2010**, *46*, 2920–2922.
18. L. Mao, T. Sotomura, K. Nakatsu, N. Koshiba, D. Zhang, T. Ohsaka, *J. Electrochem. Soc.* **2002**, *149*, A504–A507.
19. L. Mao, D. Zhang, T. Sotomura, K. Nakatsu, N. Koshiba, T. Ohsaka, *Electrochim. Acta* **2003**, *48*, 1015–1021.

20. F. H. B. Lima, M. L. Calegaro, E. A. Ticianelli, *J. Electroanal. Chem.* **2006**, *590*, 152–160.

21. F. H. B. Lima, M. L. Calegaro, E. A. Ticianelli, *Electrochim. Acta* **2007**, *52*, 3732–3738.

22. Crystal data for $Mn_2C_{16}N_2O_{10}H_{24}$, M_r = 514.25, triclinic, space group $P\bar{1}$ (no. 2), a = 6.473(13), b = 7.970(16), c = 10.577(2) Å, α = 101.69(3)°, β = 102.84(3)°, γ = 105.70(3)°, V = 491.7(17) Å^3, Z = 1, d_{calcd} = 1.737 g cm^{-3}, T = 100(2) K, crystal size 0.2 x 0.2 x 0.1 mm^3, λ = 0.69999 Å, 2θ = 67.92, 136 parameters, R_1 = 0.0379 ($I > 2\sigma(I)$, 2865 reflections), wR_2 = 0.1082 (all data, 5533 reflections), GOF = 1.093. Further crystallographic details for the structure can be obtained from the Cambridge Crystallographic Data Center, on quoting the depository number CCDC 978436.

23. M. Oku, K. Hirokawa, S. Ikeda, *J. Electron Spectrosc. Relat. Phenom.* **1975**, *7*, 465–473.

24. V. Di Castro, G. Polzonetti, *J. Electron Spectrosc. Relat. Phenom.* **1989**, *48*, 117–123.

25. T. Gao, P. Norby, F. Krumeich, H. Okamoto, R. Nesper, H. Fjellvag, *J. Phys. Chem. C* **2010**, *114*, 922–928.

26. D. Grosso, C. Boissi`ere, B. Smarsly, T. Brezesinski, N. Pinna, P. A. Albouy, H. Amenitsch, M. Antonietti, C. Sanchez, *Nat. Mater.* **2004**, *3*, 787–792.

27. Z.-R. Tian, W. Tong, J.-Y. Wang, N.-G. Duan, V. V. Krishnan, S. L. Suib, *Science* **1997**, *276*, 926–930.

28. A.-S. Malik, M. J. Duncan, P. G. Bruce, *J. Mater. Chem.* **2003**, *13*, 2123–2126.

29. A. K. Sinha, K. Suzuki, M. Takahara, H. Azuma, T. Nonaka, K. Fukumoto, *Angew. Chem., Int. Ed.* **2007**, *46*, 2891–2894.

30. M. Imperor-Clerc, D. Bazin, M. D. Appay, P. Beaunier, A. Davidson, *Chem. Mater.* **2004**, *16*, 1813–1821.

31. J.-Y. Luo, J.-J. Zhang, Y.-Y. Xia, *Chem. Mater.* **2006**, *18*, 5618–5623.

32. F. Jiao, P. G. Bruce, *Adv. Mater.* **2007**, *19*, 657–660.

33. F. Jiao, A. Harrison, A. H. Hill, P. G. Bruce, *Adv. Mater.* **2007**, *19*, 4063–4066.

34. F. Jiao, J.-C. Jumas, M. Womes, A. V. Chadwick, A. Harrison, P. G. Bruce, *J. Am. Chem. Soc.* **2006**, *128*, 12905–12909.

35. H. Tüysüz, Y. Liu, C. Weidenthaler, F. Schüth, *J. Am. Chem. Soc.* **2008,** *130*, 14108-14110.

36. G.-L. Xu, Y.-F. Xu, J.-C. Fang, F. Fu, H. Sun, L. Huang, S. Yang, S.-G. Sun, *ACS Appl. Mater. Interfaces* **2013**, *5*, 6316-6323.

37. S. S. T. Bastos, J. J. M. Orfao, M. M. A. Freitas, M. F. R. Pereira, J. L. Figueiredo, *Appl. Catal., B* **2009,** *93*, 30-37.

38. Y. Gorlin, C.-J. Chung, D. Nordlund, B. M. Clemens, T. F. Jaramillo, *ACS Catal.* **2012**, *2*, 2687-2694.

39. T. Rhadfi, J.-Y. Piquemal, L. Sicard, F. Herbst, E. Briot, M. Benedetti, A. Atlamsani, *Appl. Catal. A.* **2010**, *386*, 132-139.

40. X. Han, T. Zhang, J. Du, F. Cheng, J. Chen, *Chem. Sci.* **2013**, *4*, 368-376.

41. J. Suntivich, H. A. Gasteiger, N. Yabuuchi, Y. Shao-Horn, *J. Electrochem. Soc.* **2010,** *157*, B1263-B1268.

42. Z.-W. Liu, F. Peng, H.-J. Wang, H. Yu, W.-X. Zheng, J. Yang, *Angew. Chem., Int. Ed.*, **2011,** *50*, 3257-3261.

43. W. Yang, T.-P. Fellinger, M. Antonietti, *J. Am. Chem. Soc.* **2011,** *133*, 206-209.

44. S. Wang, D. Yu, L. Dai, *J. Am. Chem. Soc.* **2011,** *133*, 5182-5185.

2.3. Thermal conversion of a Li- and Si-containing MOF for preparation of Li_4SiO_4 ceramic

Introduction

Anthropogenic carbon dioxide (CO_2) emission is considered to be one of the major reasons for global warming, which is a serious environmental threat.[1] CO_2 is mostly derived from the combustion of fossil fuels in power plants (approximately one-third of the emitted CO_2) and it is expelled as a hot gas.[2,3] In this regard, the capture and sequestration of CO_2 at high temperatures is an emerging area of research aimed at reducing the concentration of CO_2 in the atmosphere. Among various CO_2-capture materials, lithium-based ceramics such as Li_2ZrO_3, Li_2SiO_3, Li_8SiO_6, Li_5AlO_4, Li_4TiO_4, and Li_4SiO_4 have achieved recognition, because they capture CO_2 via chemisorption in a wide temperature range and with a high degree of recyclability.[4-9] Among them, lithium orthosilicate (Li_4SiO_4) is a qualified candidate for the uptake of CO_2 from combustion gases, because of its fast absorption kinetics and large absorption capacity (theoretical sorption amount of 36.7 wt%).[10,11]

Li_4SiO_4-based absorbents are conventionally synthesised by the solid-state reaction of silica with lithium salts such as LiOH and Li_2CO_3, as described in equation (1). As part of an effort to vary the types of precursors and the synthetic conditions, the impregnation-precipitation process[12,13] and sol-gel synthesis[14,15] have been used for the synthesis of Li_4SiO_4, which has led to changes to its surface properties and to an increase of its surface area. Because CO_2 molecules react with Li^+ and O^{2-} ions diffused from inside of the Li_4SiO_4 absorbent on the surface[16] according to equation (2), those efforts were effective for enhancing the CO_2-capture performances. Therefore, various attempts with new precursors and methods are meaningful to develop absorbents with good performances.

$$2Li_2CO_3 + SiO_2 \rightarrow Li_4SiO_4 + 2CO_2 \qquad \text{Eq. (1)}$$
$$Li_4SiO_4 + CO_2 \rightarrow Li_2SiO_3 + Li_2CO_3 \qquad \text{Eq. (2)}$$

The conversion reaction of MOFs has been employed as a synthetic method that affords inorganic materials with novel properties. In particular, because ceramics that require solid-state reactions at high temperatures hardly allow for control of the morphologies, the implementation of a method to convert MOFs into ceramics enables ceramics to possess various interesting morphologies. In this work, a newly designed MOF, containing Li and Si atoms, was synthesised and used as a precursor. This MOF was thermally converted into Li_4SiO_4, which has a coral-like morphology; its unique structural properties enhance its CO_2-sorption behaviour. We attribute these features to the MOF precursor and its thermal conversion reaction. To construct a MOF containing Li and Si atoms in a 4:1 ratio, it is important to introduce an appropriate organic building block. In this sense, tetrakis(4-carboxyphenyl)silane (H_4TCS) is a proper ligand.[17] It is a Si-centred tetracarboxylic acid ligand (Figure 2.17); the electronic charge of the derived tetracarboxylate can be balanced by four Li^+ ions.
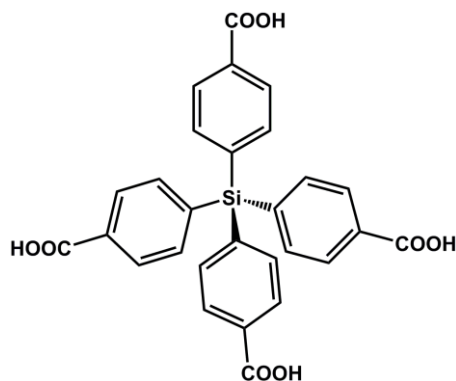
Figure 2.17. Tetrakis(4-carboxyphenyl)silane (H₄TCS).

Experimental section

All chemicals and solvents used in the synthesis were of reagent grade and those were used without further purification. Tetrakis(4-carboxyphenyl)silane (TCS) was prepared by the method reported in the previous study.[24] Infrared spectra were recorded with a ThermoFisher Scientific iS10 FT-IR spectrometer. Elemental analyses were performed at the Ulsan National Institute of Science and Technology (UNIST) Central Research Facilities by using a Thermo Scientific Flash 2000 series CHNS/O analyzer. TGA was performed under a N_2 (g) atmosphere at a scan rate of 5 $^{\circ}C$ min^{-1} using Q50 from TA instruments. XRPD data were recorded on a Bruker D2 phaser diffractometer at 30 kV and 10 mA for Cu Kα (λ = 1.541 Å), with a step size of 0.02° in 2θ. SEM images were taken using a Quanta 200 microscope (FEI) operating at 18 kV. TEM images and energy dispersive X-ray spectra were obtained with a JEOL JEM-2100F microscope. The nitrogen adsorption-desorption isotherms were measured at 77 K using liquid nitrogen on a BELsorp-MAX. Prior to adsorption measurement the samples were evacuated at 250 $^{\circ}C$ under vacuum (p < 10^{-4} bar) for 6 h.

Synthesis of LiTCS, [Li₄(TCS)·2DEF·1EtOH]·0.25EtOH·1H₂O. TCS (40 mg, 0.078 mmol) was dissolved in DEF (4 mL) and added to an EtOH solution (2 mL) of LiNO₃•6H₂O (25 mg, 0.31 mmol). The mixture was placed in a Teflon vessel within the autoclave, and heated and kept at 120 $^{\circ}C$ for 24 h. The solution was cooled to room temperature. Pale-yellow crystals formed, which were filtered off and washed briefly with the mother liquor. Yield: 69%. FTIR (KBr, cm^{-1}): 3449 (O-H, coordinated EtOH), 3059 (Ar-H), 2976 (C-H, DEF), 2880 (C-H, aldehyde in DEF), 1660 (C=O amide in DEF), 1611 (asymmetric O-C=O, carboxylate), 1414 (symmetric O-C=O, carboxylate), 1100, 730 (Si–Ph). Anal. Calcd for C₄₀.₅H₄₇.₅Li₄N₂O₁₂.₂₅Si₁: C, 59.75; H, 5.88; N, 3.44. Found: C, 59.10; H, 5.13; N, 3.41.

Synthesis of Li₄SiO₄ by a conversion reaction of LiTCS MOF. Grinded LiTCS crystals were heated at 5 $^{\circ}C$ min^{-1} under a nitrogen flow of 250 mL min^{-1}. After reaching the target temperature of 700 $^{\circ}C$, it was maintained for 6 h, then cooled to room temperature. As the next step, the resultant black powder was heated in a box furnace (ambient air environment) at 10 $^{\circ}C$ min^{-1}. After reaching the target

temperature of 650 $^{\circ}$C, the material was maintained at that temperature for 2 h. After cooling to room temperature, white solid was acquired.

Synthesis of Li$_4$SiO$_4$ by a conventional method for comparison. A mixture of lithium hydroxide monohydrate and fumed silica in water with a Li/Si molar ratio of 4.1:1 was stirred and heated at 70 ºC until the precursors were dissolved in water. Then, the solution was heated at 105 ºC to evaporate the water and the resulting powder was calcined at 700 ºC for 4 h in tube furnace under a nitrogen flow of 500 mL/min.

Single-crystal X-ray crystallography. A single-crystal of LiTCS was coated with paratone-*N* oil, and the diffraction data were measured at 100 K with synchrotron radiation (λ = 0.64999 Å) on an ADSC Quantum-210 detector at 2D SMC with a silicon (111) double crystal monochromator (DCM) at the Pohang Accelerator Laboratory, Republic of Korea. The ADSC Q210 ADX program[25] was used for data collection, and HKL3000sm (Ver. 703r)[26] was used for cell refinement, reduction, and absorption correction. The crystal structures were solved by direct methods and refined by full-matrix least-squares calculations with the SHELXL computer program.[27] The positions of all non−hydrogen atoms were refined with anisotropic displacement factors. The hydrogen atoms were positioned geometrically using a riding model.

Results and discussion

The solvothermal reaction of LiNO$_3$·6H$_2$O with H$_4$TCS in a mixture of *N*,*N*-diethylformamide (DEF) and ethanol (EtOH) yielded yellowish block-shaped crystals of [Li$_4$(TCS)(DEF)$_2$(EtOH)]·0.25EtOH·H$_2$O (designated as LiTCS; synthetic details in Experimental section). The structure of LiTCS, determined by single-crystal X-ray diffraction,[18] consists of one TCS ligand, four lithium ions, two coordinating DEF molecules, and one coordinating EtOH molecule per asymmetric unit. All the Li$^+$ ions have distorted tetrahedral geometries (Figure 2.18a): Li3 and Li4 are bonded to carboxylate oxygen atoms associated with four different TCS^{4-} moieties. Li1 is coordinated by two carboxylates and two DEF molecules. Li2 is coordinated by three carboxylates and one EtOH molecule. As shown in Figure 2.18b, among the various possible bridging modes of carboxylate ligands, the carboxylates belonging to Ph1 and Ph4 display μ_4-η^2:η^2 modes, the carboxylate from Ph2 displays a μ_3-η^1:η^2 mode, and the carboxylate from Ph3 shows a μ_2-η^1:η^1 mode. The infinite coordination in these modes generates one-dimensional [Li-COO] chains as secondary building units along the *b* axis (Figure 2.18c). Because the central Si atom of a TCS ligand has a tetrahedral geometry, the TCS ligand is expected to act as a tetrahedral node. However, in the present MOF, because two carboxylates (belonging to Ph1 and Ph4) in a TCS ligand coordinate to the intrachain Li ions, the two other carboxylates extend to coordinate to two neighbouring [Li-COO] chains (Figure 2.18d). Thus, this

ligand is a three-way junction to generate a three-dimensional (3D) network. Because of the pore blockage of two coordinating DEF molecules, this 3D MOF possesses 1D channels (Figures 2.18c and d). The X-ray powder diffraction (XRPD) pattern of the as-synthesised LiTCS is consistent with the simulated pattern derived from the single-crystal diffraction data (Figure 2.19), indicating that the bulk and single crystals are the same material.

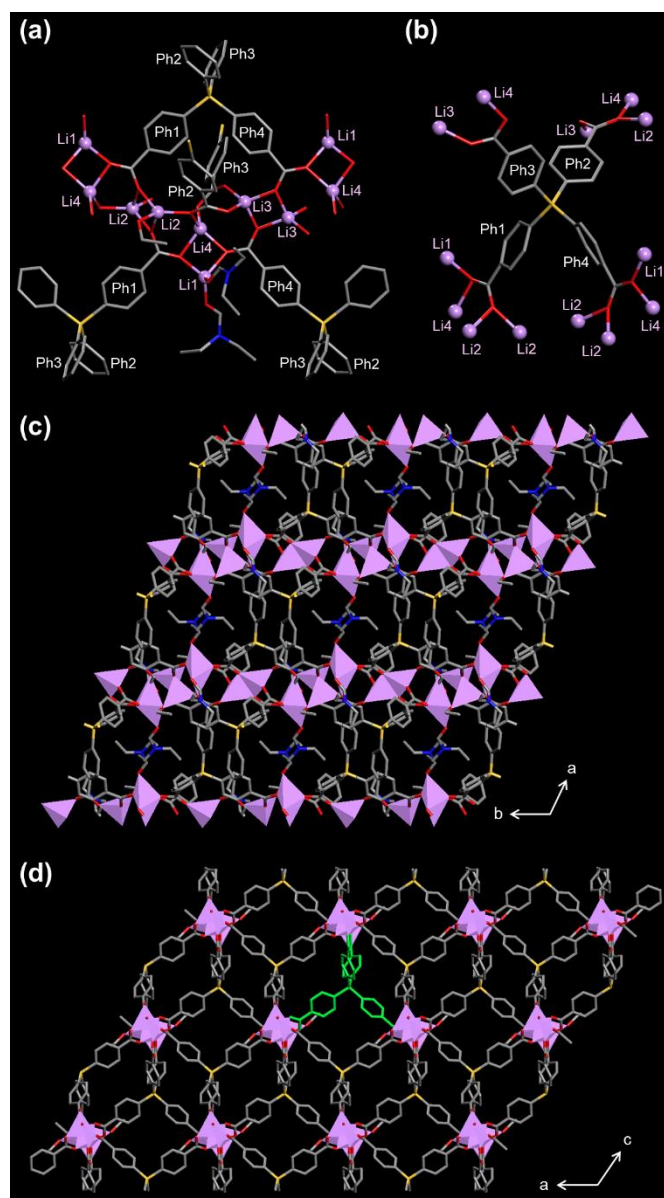**Figure 2.18.** Crystal structure of LiTCS. (a) SBUs of the Li-COO chain. (b) The coordination modes of the carboxylates of a TCS^{4-} ligand. Three-dimensional framework formed by SBUs and organic ligands, projected along (c) the *c* axis and (d) the *b* axis. Coordinating DEF molecules and Li1 in Fig 2d were omitted for clarity. (Colour scheme: C, grey; O, red; N, blue; Si, orange; Li, purple.)
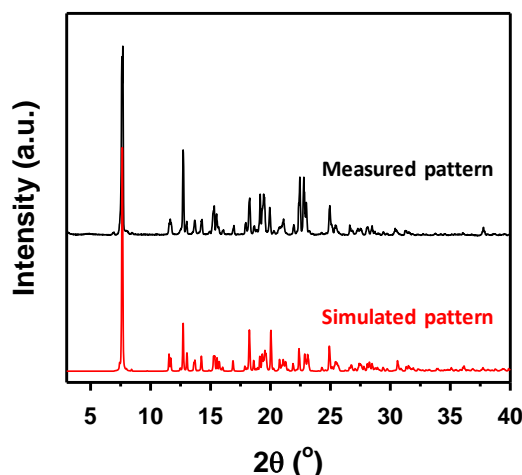
Figure 2.19. XRPD patterns of LiTCS: (a) measured pattern of as-synthesized LiTCS and (b) simulated pattern from the single-crystal X-ray diffraction data.

Thermogravimetric analysis (TGA) indicated that LiTCS thermally decomposes above ca. 550 ℃ (Figure 2.20a). Because the conventional synthesis of Li_4SiO_4 is conducted at 600–900 ℃, the grinded yellowish crystals of LiTCS were heated at 700 ℃ for 6 h in a tube furnace under a N_2 flow of 250 mL/min. As shown in Figure 2.21a, XRPD data for the resulting black powder show broad peaks that coincide with those measured for Li_4SiO_4 (JCPDS No. 76-1085). The relatively low crystallinity might originate from a large amount of carbon residue (49 wt%, based on elemental analysis) due to incomplete reaction (Figure 2.20b). Further heat treatment under air at 650 ℃ for 2 h (Figure 2.20b) consequently resulted in highly crystalline white product, displaying the sharp XRPD pattern (Figure 2.21b) of Li_4SiO_4 (trace amounts of Li_2SiO_3 were present). Despite the high annealing temperature, a small amount of carbon (~1.3 wt%) was still detected; this may be attributed to unburned carbon in the solid and/or to lithium carbonate on the surface.
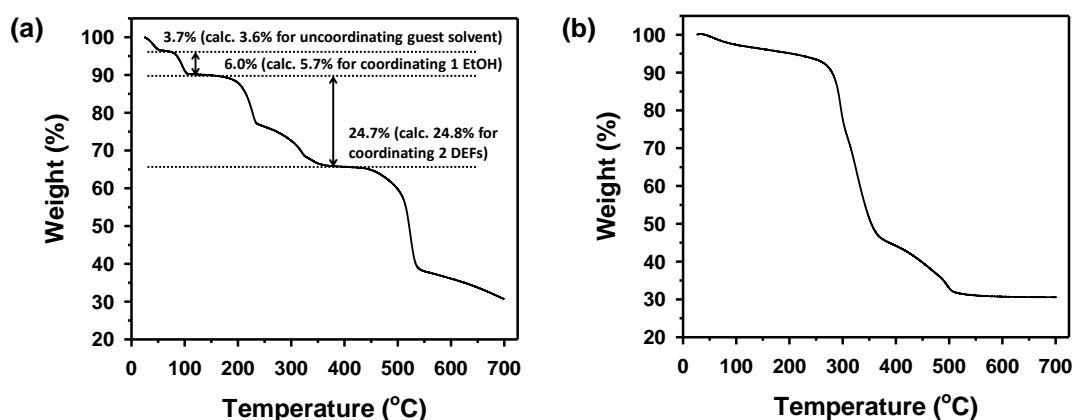

Figure 2.20. TGA traces of (a) LiTCS and (b) black powder Li_4SiO_4, measured under nitrogen and oxygen atmosphere, respectively. The result of the Li_4SiO_4 indicates 70% weight loss until 550 ℃, corresponding to decomposition of carbon residue and further progress of incomplete reaction.
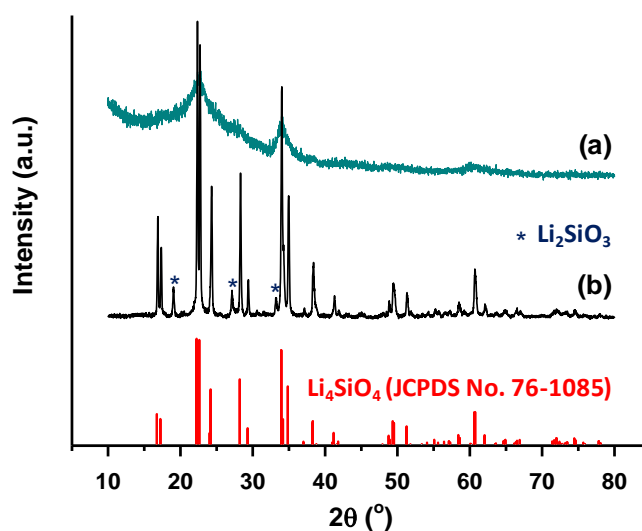
Figure 2.21. XRPD patterns of the Li_4SiO_4 (a) before and (b) after thermolysis under air at 650 °C.

The morphology of the prepared Li_4SiO_4 was investigated by scanning electron microscopy (SEM) and transmission electron microscopy (TEM). The SEM images (Figures 2.22 and 2.23) reveal the loss of original LiTCS morphology and the formation of large cracks in the solid, which is presumably caused by volume shrinkage in going from LiTCS to Li_4SiO_4 (1057.9 to 82.4 $Å^3$, based on the volume for each formula containing one Si) and by the liberation of organic components during the thermal conversion. Interestingly, the resulting solid of Li_4SiO_4 has a coral-like morphology, constructed by the connection of secondary particles with relatively uniform dimensions (ca. 300 nm). The coarse integration of the secondary particles results in voids, corresponding to macropores. Thus, even though the nitrogen adsorption/desorption experimental results indicated a low surface area (Brunauer–Emmett–Teller surface area of 8 m^2/g), the material's macroporosity helps the mass transport of gas during CO_2 capture, thus enhancing the uptake rate and amounts. High-magnification SEM and TEM images, for closer observation, show that each secondary particle is composed of primary particles of 20–50 nm (Figure 2.23a (inset) and b). It should be noted that the present Li_4SiO_4 has a unique morphology which cannot be achieved by conventional synthetic methods (details in the experimental section).[4] As shown in Figure 2.24, Li_4SiO_4 is usually in the form of large agglomerates, forming a rock-like bulk solid. In contrast, the coral-like morphology of the Li_4SiO_4 reported herein is attributed to the self-templating effect of the MOF. We have previously suggested that organic substances generated during the thermal decomposition of the MOF are confined to act as templates;[19-21] afterwards, they are converted into nanopores. Accordingly, the conversion reaction of MOFs can be a facile and successful method to impart metal oxides with interesting architectures; this is especially true for ceramics, which require high reaction temperatures.
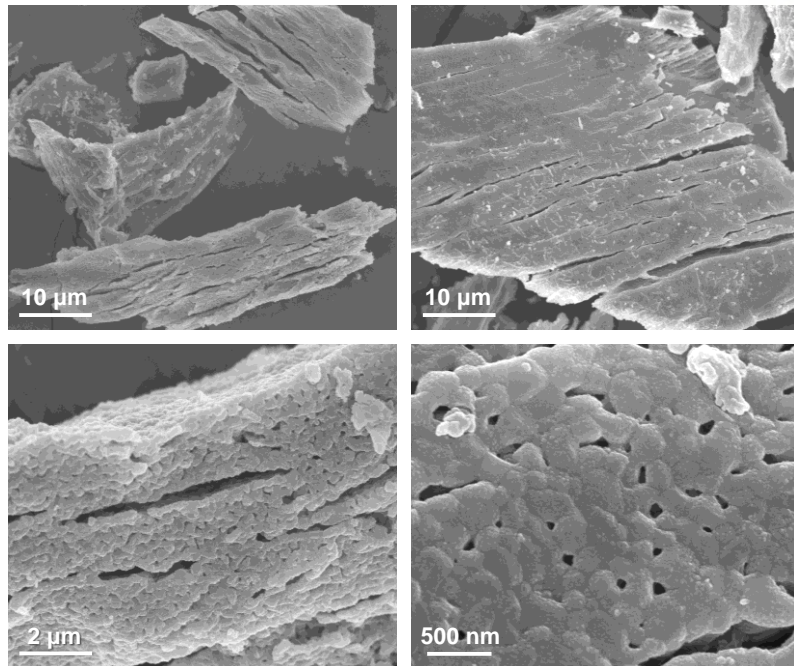
Figure 2.22. SEM images of the as-synthesized Li_4SiO_4.
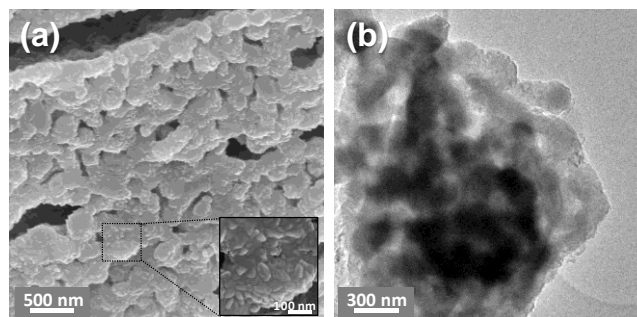

Figure 2.23. (a) SEM and (b) TEM images of the as-synthesised Li_4SiO_4, showing its coral-like morphology.
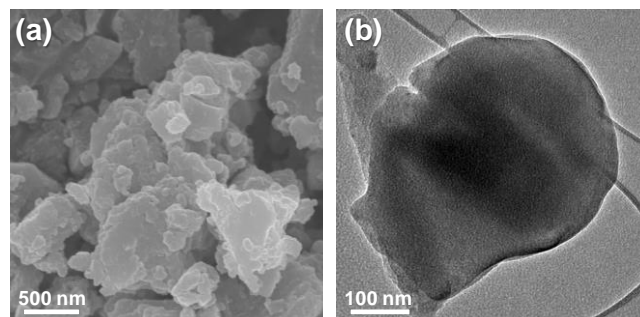

Figure 2.24. (a) SEM and (b) TEM images of the rock-like Li_4SiO_4 synthesized conventionally.

To verify the advantages of the special morphology of Li_4SiO_4 regarding CO_2 capture, CO_2-absorption experiments were conducted using a TGA apparatus. Figure 2.25a displays the dynamic thermogram measured at a heating rate of 5 ℃/min and a flow of 15% (v/v) CO_2 in N_2, which mimics flue gas. This trace displays CO_2 chemisorption around 500 ℃, accompanied by a small sorption peak below 300 ℃ (2.6 wt%; the blue asterisk in Figure 2.25a), which is due to the reaction of Li_2SiO_3 with CO_2.[22,23] The actual CO_2-chemisorption process of Li_4SiO_4 begins at 455 ℃ and reaches the apex of 18.7 wt% at 620 ℃, at which absorption and desorption are in equilibrium. At higher temperatures, the absorbed CO_2 molecules in this Li_4SiO_4 are liberated, resulting in a loss of 27.7 wt%. More mass loss relative to the initial weight (ca. 9 wt%) results from the decomposition of remaining carbon species as well as from the dissociation of CO_2 from the pre-existing Li_2CO_3 in the as-synthesised Li_4SiO_4, as mentioned previously. To examine the temperature dependence of the CO_2-absorption behaviour of Li_4SiO_4, the absorbent was monitored isothermally under flowing mimicked flue gas at 500, 550, and 600 ℃ for 6 h (Figure 2.25b). At 500 ℃, the uptake of Li_4SiO_4 shows a relatively slow saturation to 29.4 wt%. The ultimate CO_2-uptake amounts at 550 and 600 ℃ similarly approach 32.4 wt%, which corresponds to 88% of the theoretical capacity of Li_4SiO_4. However, the initial absorption rates at 550 and 600 ℃ are significantly different: during the first 5 min, while 12.0 wt% uptake occurs at 550 ℃, only 3.5 wt% uptake occurs at 600 ℃.

The Li_4SiO_4 reported herein shows a CO_2-sorption behaviour superior to that of Li_4SiO_4-based absorbents previously prepared by the conventional solid-state synthesis (maximum uptake at 550 ℃ of 7.8 wt%; 3.3 wt% uptake at 550 ℃ after 5 min) (dotted line in Figure 2.25b). The stability of the coral-like Li_4SiO_4 was also tested by cyclic absorption/desorption experiments. Absorption was performed with 15% CO_2 in N_2 at 550 ℃ and desorption was performed under pure N_2 at 650 ℃. The experimental results indicate a severe decay of the absorption amounts during the first four cycles, decreasing from 22.4 wt% to 11.4 wt%. After 25 cycles, the CO_2-absorption/desorption processes converged to 7.7 wt%, which is a third of the uptake of the first cycle. SEM images of the solid at the end of the experiment show that the porous coral-like morphology had mostly collapsed (Figure 2.26). This result indicates that the deterioration of the CO_2-capture capacity is directly related to the destruction of the material's morphology. The same cyclic test for the morphologically featureless rock-like Li_4SiO_4, meanwhile, displayed a gradual decline of the absorption capacity from 6.5 wt% to 2.2 wt% over the 25 cycles (dotted red line in Figure 2.25c). The result implies there might be other factors that have a bad influence on the reversibility of the CO_2 absorption processes, except the morphological one. However, since the coral-like sample shows the much larger degradation of absorption capacity during the cycles, it can be said that the enhanced CO_2-uptake capacity is surely caused by the coral-like morphology generated during the MOF conversion, which has a significant effect on the absorption rate and capacity. As a result, the development of absorbents showing advanced and robust morphologies will be a further important direction of this research.

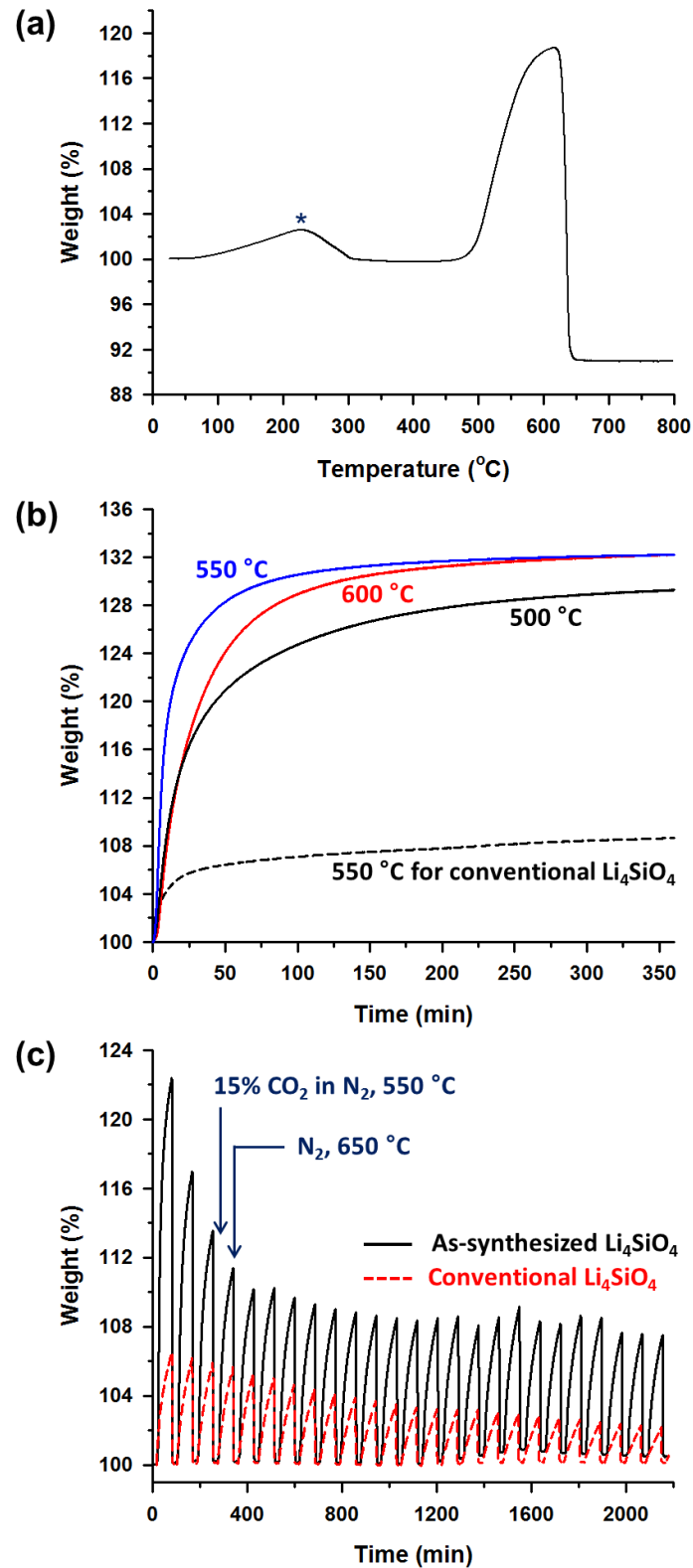**Figure 2.25.** (a) TG curves of Li_4SiO_4 obtained at a heating rate of 5 °C/min in 15% CO_2 balanced with N_2. (b) Change in mass uptake of Li_4SiO_4 over time at different temperatures with a flow of 15% (v/v) CO_2 in N_2. (c) Gas-cycling result of the absorbent.
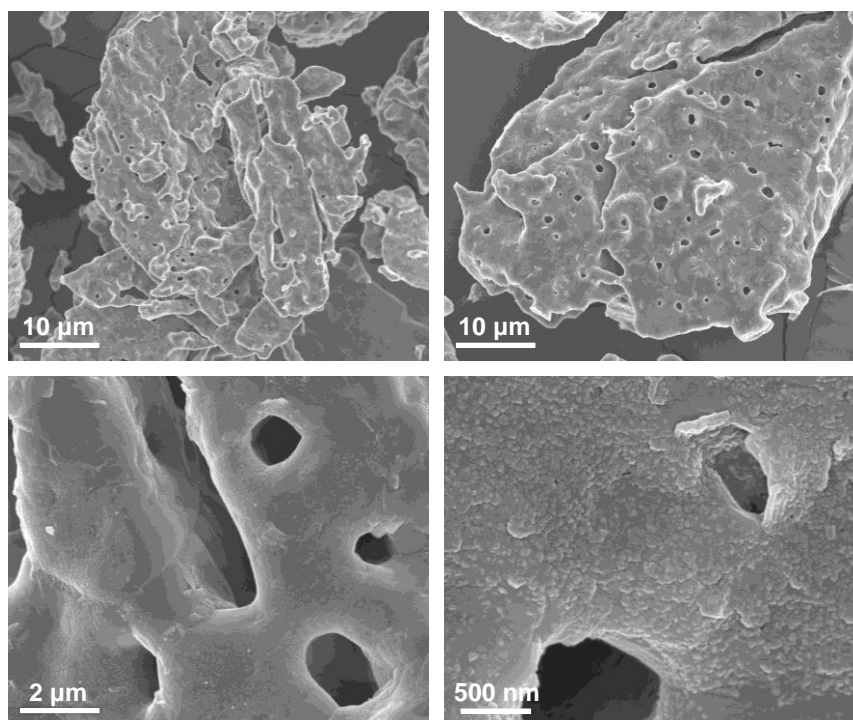
Figure 2.26. SEM images of the Li_4SiO_4 absorbent after twenty-five absorption-desorption cycles.

Conclusion

LiTCS, which is a tailored MOF containing Si and Li atoms, was synthesised and used as a precursor for Li_4SiO_4. This MOF-conversion method resulted in a coral-like morphology of Li_4SiO_4, which can hardly be achieved by the conventional synthetic approach. The as-prepared Li_4SiO_4 showed CO_2-absorption behaviour superior to that of other materials, having a much higher uptake amount and faster absorption. This might be attributed to its interesting coral-like morphology, providing a passage for the mass transport of gas and a high surface area for effective interaction. Therefore, this novel approach of MOF conversion can be a new route toward useful metal oxides (especially ceramics) with interesting architectures and advanced properties.

References

1. K. M. K. Yu, I. Curcic, J. Gabriel, S. C. E. Tsang, *ChemSusChem* **2008**, *1*, 893.
2. S, Choi, J. H. Drese, C. W. Jones, *ChemSusChem* **2009**, *2*, 796.
3. B. N. Nair, R. P. Burwood, V. J. Goh, K. Nakagawa, T. Yamaguchi, *Prog. Mater. Sci.* **2009**, *54*, 511.
4. N. Togashi, T. Okumura, K. Oh-ishi, *J. Ceram. Soc. Jpn.* **2007**, *115*, 324.
5. R. Rodríguez-Mosqueda, H. Pfeiffer, *J. Phys. Chem. A* **2010**, *114*, 4535.
6. T. Ávalos-Rendón, J. Casa-Madrid, H. Pfeiffer, *J. Phy. Chem. A* **2009**, *113*, 6919.
7. Q. Xiao, Y. Liu, Y. Zhong, W. Zhu, *J. Mater. Chem.* **2011**, *21*, 3838.

8. B. Zhang, M. Nieuwoudt, A. J. Easteal, *J. Am. Ceram. Soc.* **2008**, *91*, 1927.

9. F. durán-Muñoz, I. C. Romero-Ibarra, H. Pfeiffer, *J. Mater. Chem. A* **2013**, *1*, 3919.

10. H. Xu, W. Cheng, X. Jin, G. Wang, H. Lu, H. Wang, D. Chen, B. Fan, T. Hou, R. Zhang, *Ind. Eng. Chem. Res.* **2013**, *52*, 1886.

11. I. Romero-Ibarra, J. Ortiz-Landeros, H. Pfeiffer, *Thermochimica Acta* **2013**, *567*, 118.

12. S.Y. Shan, S.M. Li, Q.M. Jia, L.H. J, Y.M. Wang, J.H. Peng, *Ind. Eng. Chem. Res.* **2013**, *52*, 6941.

13. V. L. Mejía-Trejo, E. Fregoso-Israel, H. Pfeiffer, *Chem. Mater.* **2008**, *20*, 7171.

14. P. V. Subha, B. V. Nair, P. Hareesh, A. P. Mohamed, T. Yamaguchi, K. G. K. Warrier, U. S. Hareesh, *J. Mater. Chem. A* **2014**, *2*, 12792.

15. X. Wu, Z. Wen, X. Xu, X. Wang and J. Lin, *J. Nucl. Mater.*, 2009, **392**, 471.

16. Z. Qi, H. Daying, L. Yang, Y. Qian, Z. Zibin, *Am. Inst. Chem. Eng.* **2013**, *59*, 901.

17. H. Yu, M. Tian, C. Shen, Z. Wang, *Polym. Chem.* **2013**, *4*, 961-968.

18. Crystal data for $Li_4C_{40}H_{44}N_2O_{11}Si_1$, M_r = 784.62, triclinic, space group $P\bar{1}$ (no. 2), a = 13.725(3), b = 14.074(3), c = 14.187(3) Å, α = 114.15(3)°, β = 114.20(3)°, γ = 98.24(3)°, V = 2115.7(10) $Å^3$, Z = 2, d_{calcd} = 1.232 g cm^{-3}, T = 100(2) K, crystal size 0.17 x 0.12 x 0.11 mm^3, λ = 0.64999 Å, 2θ range = 48.694, 552 parameters, R_1 = 0.0577 ($I > 2\sigma(I)$, 8489 reflections), wR_2 = 0.1816 (all data, 16681 reflections), GOF = 1.075. Further crystallographic details for the structure can be obtained from the Cambridge Crystallographic Data Center, on quoting the depository number CCDC 1049388.

19. J. H. Lee, Y. J. Sa, T. K. Kim, H. R. Moon, S. H. Joo, *J. Mater. Chem. A* **2014**, *2*, 10435.

20. K. J. Lee, T.-H. Kim, T. K. Kim, J. H. Lee, H.-K. Song, H. R. Moon, *J. Mater. Chem. A* **2014**, *2*, 14393.

21. T. K. Kim, K. J. Lee, J. Y. Cheon, J. H. Lee, S. H. Joo, H. R. Moon, *J. Am. Chem. Soc.* **2013**, *135*, 8940.

22. J. Ortiz-Landeros, C. Gómez-Yáñez, H. Pfeiffer, *J. Solid State Chem.* **2011**, *184*, 2257.

23. E. Ochoa-Fernandez, T. Zhao, M. Ronning, D. Chen, *J. Environ. Eng.* **2009**, *135*, 397.

24. H. Yu, M. Tian, C. Shen, Z. Wang, *Polymer Chemistry* **2013**, *4*, 961-968.

25. A. J. Arvai, C. Nielsen, *ADSC Quantum-210 ADX Program*, Area Detector System Corporation; Poway, CA, USA, **1983**.

26. Z. Otwinowski, W. Minor, Methods in Enzymology, Part A. In *Macromolecular Crystallography*; Carter Jr., C. W., Sweet, R. M., Eds.;, Academic Press: New York, **1997**; Vol. 276, pp 307-326.

27. G. M. Sheldrick, *Acta Crtst, Section C* **2015**, *71*, 3.

2.4. Gradual decomposition of a tailored MOF toward CdS photocatalyst with S-doped carbon

Introduction

Hydrogen peroxide (H_2O_2) is an extremely efficient and environment-friendly oxidant, since it possesses the highest content of active oxygen (~47%) and only release H_2O as by-product on oxidation, so has been selected as one of the 100 most important chemical compound.[1,2] The commercial H_2O_2 production has been mainly done by the anthraquinone oxidation (AQO) process, but this process requires high energy input for hydrogenation/oxidation reaction, supply of H_2 gas, and organic solvents.[3,4] To not only minimize the waste generation during liquid-liquid extraction for H_2O_2 recovery at the end of AQO process but also improve the sustainability of the H_2O_2 production, noble metal-based catalysts (Pd, Pd-Au alloys, Ag, etc.) have been proposed in a direct reaction of H_2 and O_2 gases.[5-8] However, the explosive nature of the mixture of those gases incurs extra expenses for its operationalization and prevention of the contingencies, demanding a more advanced route toward cost-effective and eco-friendly H_2O_2 generation.

To subdue concerns for the explosion as well as the environment, photocatalytic production of H_2O_2 has been demonstrated to be very promising because its synthetic pathway only requires natural resources (sun light, air (O_2 gas), and water).[9-13] Metal oxide-based materials (particularly TiO_2) have shown great performances in the photocatalytic H_2O_2 production, but are only active in UV spectrum of light and have strong tendency to oxidize H_2O_2 on their surfaces, which results in the decomposition of photogenerated H_2O_2 again.[14] Many studies have observed saturation in the H_2O_2 production after a certain time period (mostly ~3 h), associated with the self-oxidation of H_2O_2 at higher concentration. To restrict this and enhance the photo-efficiency, several strategies have been proposed, such as surface passivation by fluorine,[15-17] use of a hole scavenger,[12,13,18] loading metal nanoparticles,[18-20] and addition of redox/charge transfer mediator.[21] Nevertheless, all the methods still indicate serious either environmental or economic implications with insufficient catalytic activities. Apart from them, a polymeric/complex system has been also adopted, but still had photostability issues.[22-26] Therefore, it is critical to develop ideal photocatalysts, which should be: i) robust and photostable, ii) photocatalytic with high efficiency preferably under visible light, and, at the same time, iii) inactive to photogenerated H_2O_2 as much as possible.

We firstly selected cadmium sulfide (CdS) as a potential photocatalyst, because it has narrow band gap (2.42 eV) and relatively high conduction band edge position (-0.52 V, vs NHE), so can reduce O_2 and generate H_2O_2 under visible spectrum of light.[27-29] Furthermore, it has been known that the carbon encapsulation on the catalyst can restrict the fast charge recombination, which subsequently improves the photocatalytic efficiency for H_2O_2 formation.[30,31] Thus, to produce a composite material of CdS and carbon species, we employed a metal-organic framework (MOFs) composed of Cd(II) ions and sulfur-containing organic ligands, because it has been well-known that MOFs can play parallel roles as both a

template and a precursor under an appropriate condition. For example, by utilizing the thermolysis of Ni_2(EDTA) ($EDTA^{4-}$ = ethylenediaminetetraacetate), Ni nanoparticles embedded in a carbon matrix could be easily prepared, where the carbon species are derived from the decomposition of the organic ligand.[32,33] Herein, based on this background, [Cd(EDDA)], the Cd- and S-based MOF ($EDDA^{2-}$ = 2,2'-(ethylenedithio)diacetate), was thermally transformed into CdS nanoparticles with S-doped carbon (Figure 2.27), which showed remarkable photocatalytic activities and much longer lifetime in H_2O_2 production. It is also noteworthy that using a MOF with a sulfur-containing ligand as a single precursor for the synthesis of metal sulfide nanocomposites has not been reported yet.
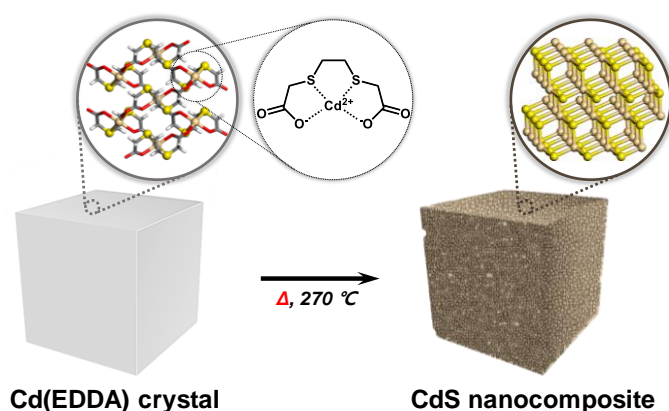

Cd(EDDA) crystal　　　　　　**CdS nanocomposite**

Figure 2.27. Schematic of MOF-derived synthesis of CdS nanocomposites with S-doped carbon.

Experimental section

All chemicals and solvents used in the syntheses were of reagent grade and they were used without further purification. 2,2'-(Ethylenedithio)diacetic acid (H_2EDDA) was bought from TCI, and $Cd(NO_3)_2 \cdot 4H_2O$ from JUNSEI. Infrared spectra were measured by a Thermo Fisher Scientific Nicolet 6700 FT-IR spectrometer. XRPD data were recorded on a Bruker D2 phaser diffractometer at 30 kV and 10 mA for Cu Kα ($\lambda = 1.54050$ Å), with a step size of 0.02° in 2θ. N_2, CO_2, H_2O sorption isotherms of samples were obtained using a BELSORP-max at 77 K, 196 K, and 298 K, respectively. Prior to the adsorption measurements, the samples were evacuated (p < 10^{-5} mbar) at RT for 24 h and then 110 °C for 4 h. TGA were performed under N_2(g) atmosphere at a scan rate of 5 °C/min using Q50 from TA instruments. Elemental analyses were done by UNIST Central Research Facilities center (UCRF) in Ulsan National Institute of Science and Technology (UNIST).

Preparation of [Cd(EDDA)]. $Cd(NO_3)_2 \cdot 4H_2O$ (1.54 g, 5 mmol) and H_2EDDA (1.05 g, 5 mmol) were dissolved in a mixture of *N,N*-dimethylformamide (DMF) and H_2O (100 mL, 1:1, v/v). The mixture solution was placed in a 500 mL glass reaction vessel, and heated at a rate of 1 °C/min and maintained at 80 °C for 12 h. After cooling to room temperature, colorless crystals were filtered off and briefly

washed with water and ethanol. Yield: ~23.5%. Anal. Calcd for $Cd_1C_6H_8O_4S_2$: C, 22.47; H, 2.51; N, 0.00; S, 20.00. Found: C, 22.47; H, 2.49; N, 0.00; S, 20.74. FT-IR (ATR, cm^{-1}): ν_{C-H} 2969, 2914 (w), $\nu_{C-O=O}$ 1566, 1370 (s). The hydrothermal reaction with a small portion of triethylamine (1.4 mL, 10 mmol) also afforded the synthesis of the same compound in powder form.

Synthesis of CdS$_{X,Y}$ nanocomposite (where x = the gas type (O_2 or N_2) and y = the heating time). Solid [Cd(EDDA)] was heated at 5 °C min^{-1} under a 500 mL min^{-1} of X gas. After reaching the target temperature of 270 °C, the material was maintained at that temperature for Y h. After cooling to room temperature, dark yellow solid was obtained.
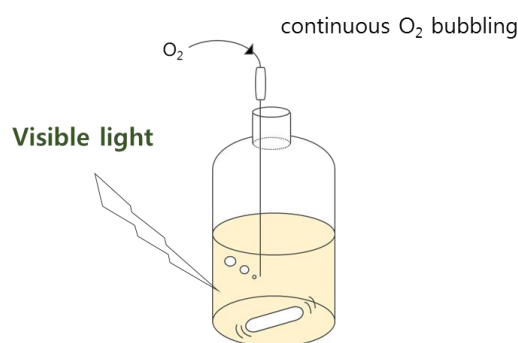
Photocatalytic production of H$_2$O$_2$. Photocatalytic activity of the samples for hydrogen peroxide production was evaluated at room temperature and pressure (Figure 2.28). 0.1g of photocatalyst powder was dispersed in 100 ml of deionized water with and without the presence of 2-propanol that was used as a sacrificial agent. The colloidal solution in the reactor was purged with oxygen gas for half an hour to saturate the oxygen in the solution in the dark condition. The performance test of the H$_2$O$_2$ production was carried out with 300W Xenon lamp with continuous oxygen bubbling. To maintain dispersion, the solution was stirred by magnetic stirrer before and during the reaction. The photocatalyst samples were tested under both visible light irradiation with 420nm cut-off filter and 1sun (100mW/cm^2) irradiation with one sun filter. 1 mL of sample was collected at every 30 min for 3 hours of the reaction by a syringe and filtrated by 0.45 µM PTFE syringe filter (Millex).
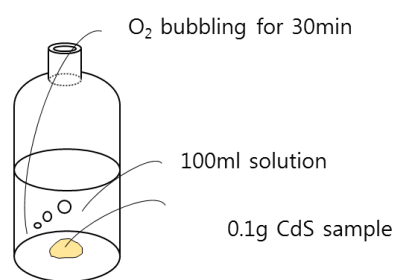
Figure 2.28. Schematic illustration of the photocatalytic experiment for H$_2$O$_2$ production.

Photocatalytic decomposition of H$_2$O$_2$. Hydrogen peroxide decomposition activity of commercial CdS and MOF-derived CdSs is tested under 1sun (100mW/cm^2) intensity with 1 sun filter and polymer/TiO$_2$ is tested under visible light irradiation with 420nm cut-off filter with 300W Xenon lamp with continuous stirring. 0.1 g of commercial CdS and MOF-derived CdSs was dispersed in 100 ml of 1mM

H_2O_2 solution that was made by diluting hydrogen peroxide (35%, Alfa Aesar) in deionized water. To avoid H_2O_2 production from oxygen, reactor was purged with nitrogen gas and oxygen gas was removed for 30 mins in dark before decomposition test.

Measurement of H_2O_2 concentration. The concentration of generated H_2O_2 is measured by DPD method. 1 mL H_2O_2 sample was collected by syringe from the reactor and it was filtrated by 0.45 µM PTFE filter (Millex) to separate H_2O_2-containing solution from photocatalyst powders. Sodium phosphate buffer was added to properly diluted sample and then, deionized water is added. N,N,-Diethyl-p-phenylene-diamine sulfate (DPD, ≥98%, Sigma-Aldrich) solution (in 0.1 N sulfuric acid standard solution) and peroxidase (POD, horseradish, Sigma) solution (in deionized water) was used to make vivid color for measuring absorbance of hydrogen peroxide. The concentration corresponding its absorbance was automatically calculated by using UV-visible spectrophotometer (UV-2600, Shimazu).

Results and discussion

[Cd(EDDA)] can be readily prepared via the coordination of Cd(II) ions with EDDA[2-] by heating in a 1:1 (v/v) mixture of *N,N'*-dimethylformamide (DMF) and water. In the corresponding product, which is colorless crystals,[34] the Cd(II) center is positioned in an octahedral geometry, forming six bonds with two sulfur atoms of the thioethers from one EDDA ligand and four oxygen atoms of the carboxylates from the three different EDDA ligands (Figure 2.29 and 2.30). Their repetitive assemblies generate 2D sheets, which are stacked in parallel. Thermogravimetric analysis (TGA) showed that this compound is thermally stable up to 300 °C without any weight loss, whether under the flow of N_2 or O_2 (Figure 2.31). Nevertheless, we could observe that heating at 270 °C can slowly transform the structure into single phase CdS (Hawleyite, JCPDS No. 10-0454), as revealed by the time-variable TGA trace measured at 270 °C and X-ray powder diffraction (XRPD; Figure 2.32a-b and 2.33), which take 12 h to complete the thermal transition into the CdS phase (hereafter, the as-synthesized samples will be designated as **CdS$_{x,y}$** where x = the gas type (O_2 or N_2) and y = the heating time). It should be noted that the [Cd(EDDA)] crystals gradually turned yellowish over the heating time, and the X-ray diffraction of a selected crystal after 6 h heat-treatment showed both single-crystal pattern of [Cd(EDDA)] and polycrystalline ring pattern of CdS. This implies that the CdS phase is generated throughout the crystals, resulting in the homogeneous mixture of the two different materials, notably, which kind of partial decomposition within a MOF crystal has been very rarely reported so far.

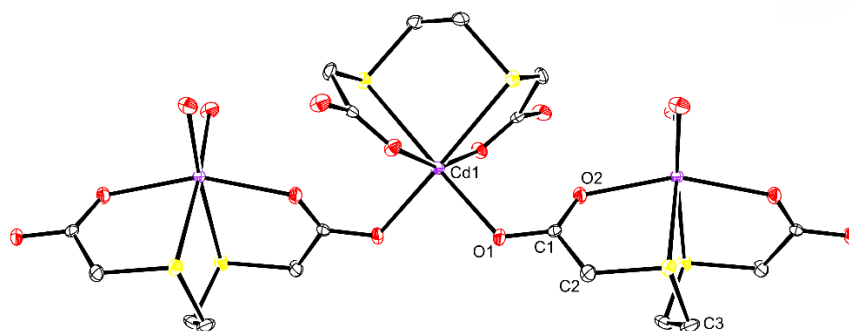**Figure 2.29.** An ORTEP drawing of [Cd(EDDA)] with an atomic numbering scheme (thermal ellipsoids at 50% probability). Hydrogen atoms are omitted for clarity. Color scheme: Cd, purple; C, black; O, red; S, yellow.

Figure 2.30. XRPD patterns of [Cd(EDDA)]: (a) experimental and (b) simulated data.

Figure 2.31. TGA trance of [Cd(EDDA)] obtained under a nitrogen (blue line) or an oxygen (red line).

54
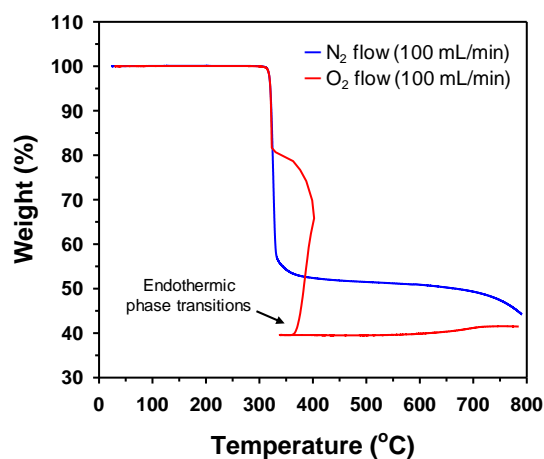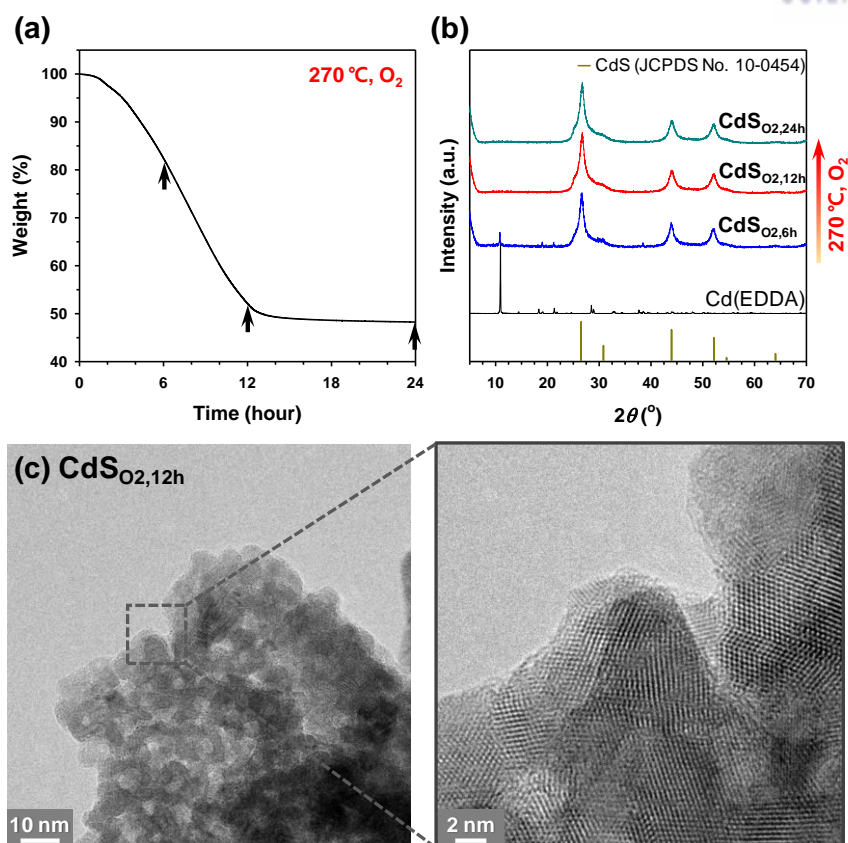
Figure 2.32. (a) Time-variable TGA trace of [Cd(EDDA)] at 270 ℃ under 100 mL/min of O_2 flow and (b) XRPD patterns of the corresponding [Cd(EDDA)], **CdS$_{O2,6h}$**, **CdS$_{O2,12h}$**, and **CdS$_{O2,24h}$**. (c) Representative TEM images of **CdS$_{O2,12h}$**.

Figure 2.33. XRPD patterns of [Cd(EDDA)], **CdS$_{N2,6h}$**, **CdS$_{N2,12h}$**, and **CdS$_{N2,24h}$**.

The broad peaks in the XRPD patterns indicate a nanocrystalline nature of the obtained dark-yellow solids. The average sizes of nanocrystals in $CdS_{O2,6h}$, $CdS_{O2,12h}$, and $CdS_{O2,24h}$ were estimated to be 5.5, 5.4, and 5.6, respectively, by applying the Debye-Scherrer equation to the (220) reflections. T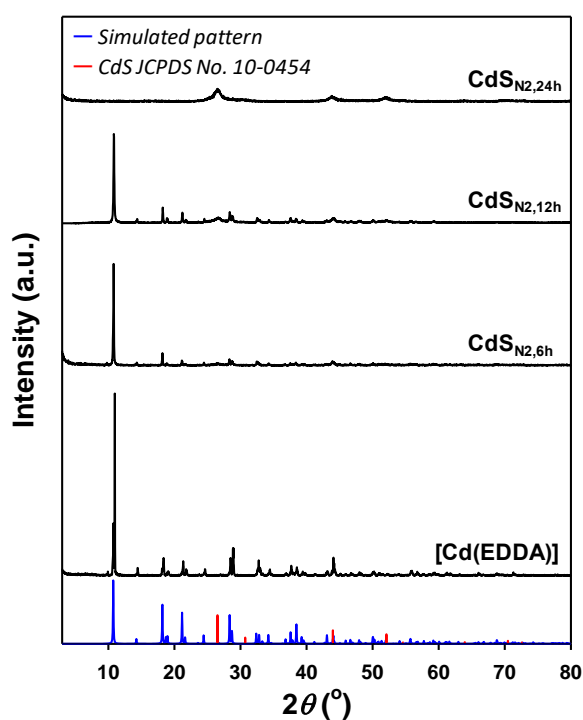ransmission electron microscopy (TEM) images in Figure 2.32c further confirm that the materials consist of 5~10 nm-sized nanoparticles. Due to the slow and gradual transformation under the moderate temperature, aggregation of nanoparticles does not result from the heating under O_2. Meanwhile, the clear lattice fringes indicate that the CdS crystallites were well-constructed even in nanoscale during the MOF conversion. However, it was difficult to identify carbon species through the TEM images, even though the elemental analysis identifies a small portion of carbon residue within the samples (4.18wt% and 3.43wt% for $CdS_{O2,12h}$ and $CdS_{O2,24h}$, respectively). On the other hand, converting [Cd(EDDA)] under N_2 atmosphere is completed after 24 h and remains CdS nanoparticles (similar size to the samples obtained under O_2) and 9.11wt% of carbon, which could be observed in the TEM images (Figure 2.34).
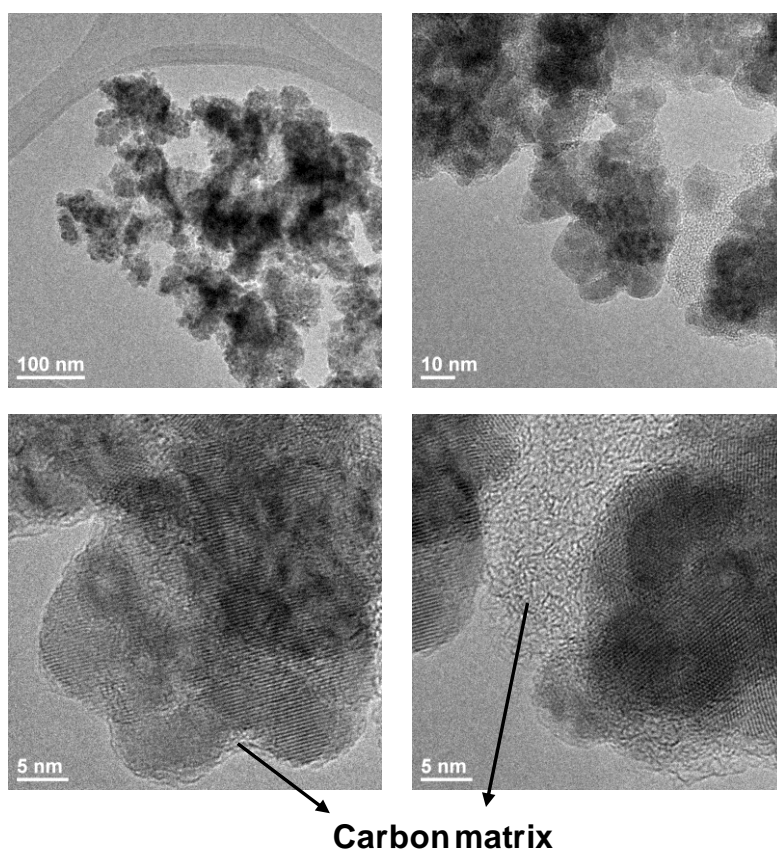

Carbon matrix

Figure 2.34. TEM images of $CdS_{N2,24h}$.

To establish the states of CdS and carbon residue, the X-ray photoelectron spectroscopy (XPS) was conducted for the **CdS$_{O2,12h}$** and the Cd 3d$_{5/2}$, S 2p, O 1s, and C 1s spectra were deconvoluted as shown in Figure 2.35. Besides the peak from cadmium sulfide at 161.0 eV, the other four peaks in the S 2p spectra are assigned to organic sulfur (e.g., thiol or C-S groups; 161.9 and 163.0 eV) and sulfate species (168.9 and 170.2 eV). In the C 1s spectra, the major peak at 284.8 eV is attributable to organic sp^3 carbon. The binding energies of 287.0 and 288.4 eV may represent carbon in many different environments (e.g. C-S, C-OH and C-O-C for 287.0 eV, and S-C=O, O-C=O and C=O for 288.4 eV). Those results indicate that **CdS$_{O2,12h}$** possess sulfur-doped polymeric carbon on the surface. Notably, the Cd 3d$_{5/2}$ spectra reveals the presence of cadmium oxide with binding energy of 404.0 eV, where oxygen may come from either the gas or the pre-coordinated oxygen atoms from the ligand's carboxylates. The similar result is also observed for the O 1s spectra with the peak at 530.4 eV assigned to cadmium. It is noteworthy that the role of this coexistent cadmium oxide on the photocatalysis has been excluded based on our experimental results that the surface oxidation of commercial CdS almost did not change its photocatalytic activity. In the energy-dispersive X-ray spectroscopy (EDS) mapping as well, the CdS nanoparticles as well as the carbon and cadmium oxide are well dispersed across the **CdS$_{O2,12h}$** sample (Figure 2.36).

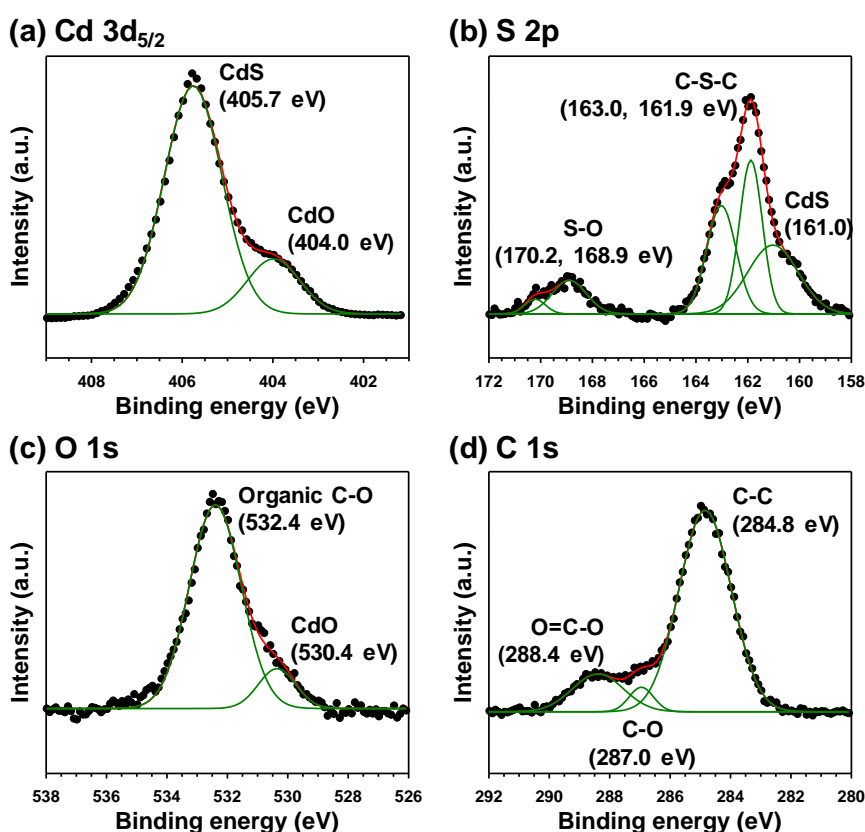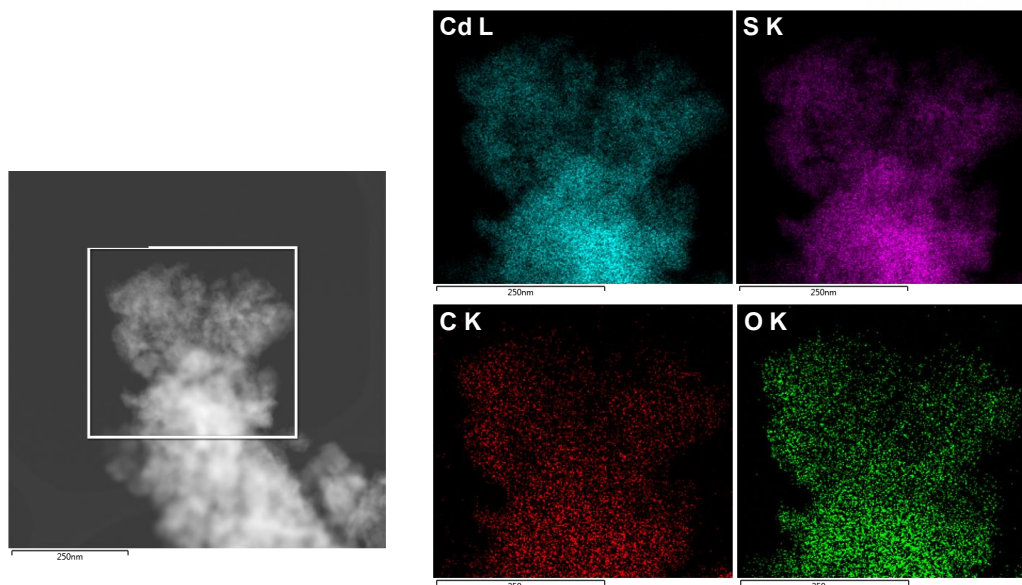**Figure 2.35.** XPS spectra. (a) Cd 3d$_{5/2}$, (b) S 2p, (c) O 1s, and (d) C 1s spectra of **CdS$_{O2,12h}$**.

Figure 2.36. EDS mapping of **CdS$_{O2,12h}$**.

To determine the optimal sample for the photocatalytic H$_2$O$_2$ formation, four samples ([Cd(EDDA)], **CdS$_{O2,6h}$**, **CdS$_{O2,12h}$**, and **CdS$_{O2,24h}$**) were firstly tested under visible light spectrum in deionized water at room temperature with 10% of 2-propanol as a hole scavenger (detailed experimental methods in SI). As summarized in Figure 2.37a, the bare [Cd(EDDA)] sample shows photo-inactivity; the concentration of H$_2$O$_2$ after 3 h is 0.02 mM (i.e. almost zero). On the other hand, a dramatic increase of photocatalytic performances in H$_2$O$_2$ production was observed for **CdS$_{O2,6h}$**, **CdS$_{O2,12h}$**, and **CdS$_{O2,24h}$**; after 3 hours, the highest concentration of H$_2$O$_2$ was recorded as 0.36, 0.82, and 0.71 mM, respectively. Thus, it is conclusive that the optimum annealing time under O$_2$ atmosphere is 12 h.

To make comparative studies, **CdS$_{O2,12h}$** is further compared with commercial CdS and **CdS$_{N2,24h}$** (Figure 2.37b). The commercial CdS shows the concentration of 0.20 mM after 3 h photo-reaction), which is much lower than that of **CdS$_{O2,12h}$**. This may have been attributed to its larger particle size (still nanoscale though) and absence of the carbon species. Interestingly, for the case of **CdS$_{N2,24h}$**, the H$_2$O$_2$ concentration linearly increases over time, reaching 0.24 mM at 3 h, but the capability itself to generate H$_2$O$_2$ is not much different compared to commercial CdS until 3 h. This result indicates that the high amount of carbon may stabilize the photocatalyst; i.e., the thicker carbon layer blocks the approach of H$_2$O$_2$ molecules on to the surface of the photocatalyst and thus prevents their photodecomposition, which can result in the steady formation of H$_2$O$_2$ without saturation. However, carbon may also prohibit the optical absorption to the photocatalyst, thereby reducing its photo-activity itself. Therefore, the increase in H$_2$O$_2$ concentration can be the most pronounced in the **CdS$_{O2,12h}$** sample owing to its optimal amount of carbon shell, with the strongest photoactivity despite its slight saturation of the concentration over time.
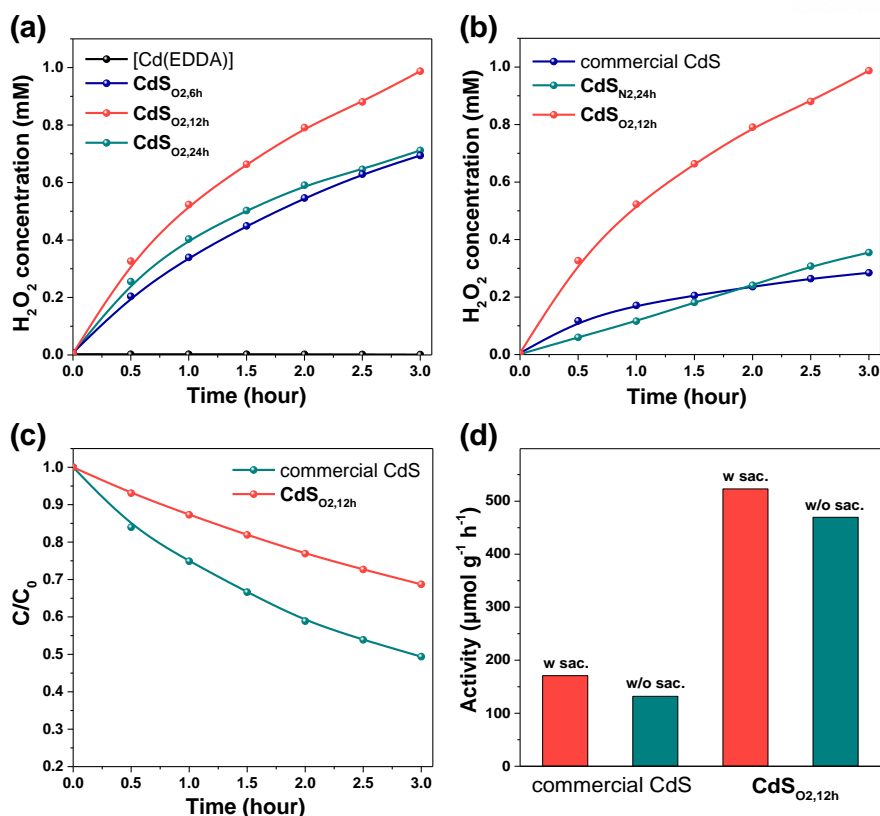
Figure 2.37. Photocatalytic H_2O_2 production under visible light spectrum ($\lambda > 420$nm) in deionized water with 10% 2-propanol as a hole scavenger; (a) [Cd(EDDA)] and **CdS$_{O2,y}$** series, and (b) commercial CdS, **CdS$_{N2,24h}$**, and **CdS$_{O2,12h}$**. (c) Photocatalytic H_2O_2 decomposition and (d) comparison in use of hole scavenger for commercial CdS and **CdS$_{O2,12h}$**.

Figure 2.37c indicates the photocatalytic decomposition rates of H_2O_2 under visible light irradiation. Approximately half of pre-existed H_2O_2 was degraded by commercial CdS after 3 h. On the other hand, **CdS$_{O2,12h}$** decomposes only about 30 percent of H_2O_2 during 3 h, although H_2O_2 itself is usually used as a sacrificial reagent of photocatalytic reaction. The low H_2O_2 degradation rate for **CdS$_{O2, 12h}$**, desptie its much higher photoactivity than that of commercial CdS, is another evidence that carbon residues on the surface is inhibiting H_2O_2 from being adsorbed on the surface of the photocatalyst and degraded by accepting holes from the photocatalyst. To further prove this point, the test for the H_2O_2 production of the commercial CdS and **CdS$_{O2,12h}$** samples was extended up to 24 h. The H_2O_2 formation by **CdS$_{O2,12h}$** was not saturated even until 24 h, reaching to 2.75 mM (5.5 times higher than 0.5 mM of commercial CdS), while commercial CdS almost saturated after 8 h (Figure 2.38). Furthermore, both the samples shows little difference in photocatalytic activity with or without the hole scavenger (i.e. 2-propanol), as compared in Figure 2.37d.
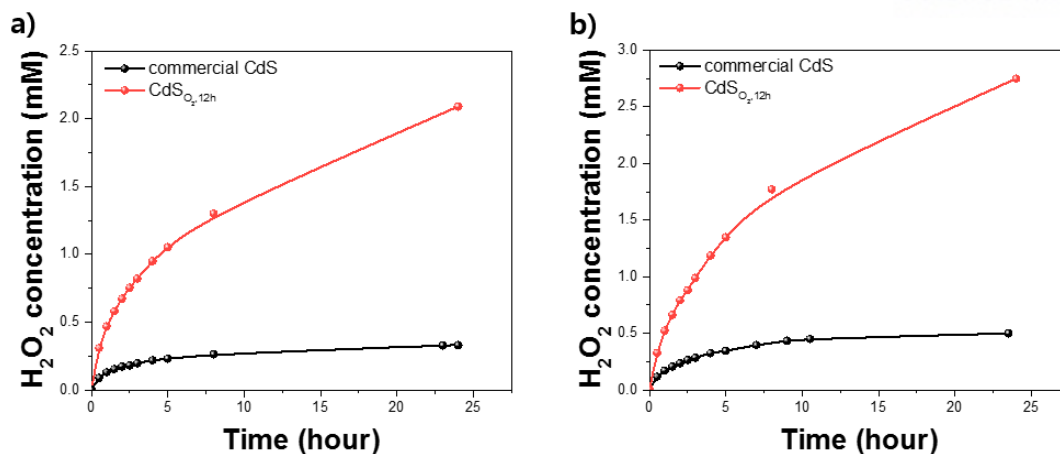
Figure 2.38. Photocatalytic hydrogen peroxide production of commercial CdS and **CdS$_{O2,12h}$** under visible light spectrum (λ > 420nm) in DI water for 24 h (a) without hole scavenger and (b) with 10% 2-propanol as a hole scavenger.

The great advantage of synthesizing metal-based nanomaterials via the MOF conversion approach is that it is very easy to dope and distribute other kinds of metal atoms within the original materials. Our group has previously demonstrated the synthesis of nanostructured ceria-based solid solutions by simultaneously coordinating transition metal ions at a synthetic stage of the MOF precursors. Inspired by the work, a small amount of Pt(II) ions were added during the synthesis of [Cd(EDDA)] and rapidly precipitated by triethylamine, to create Pt-doped crystals of [Cd(EDDA)] (Figure 2.41), which were then converted into a CdS nanocomposite following the same condition as **CdS$_{O2,12h}$** (designated as **Pt@CdS-0.53mol%**; the molar concentration cacluated based on inductively coupled plasma-mass spectroscopy (ICP-MS); synthetic details in SI). This **Pt@CdS-0.53mol%** sample has almost identical textural prperties (similar sized nanoparticles; Figure 2.40) with **CdS$_{O2,12h}$**, yet the Pt atoms are very homogeneously distributed throughout the material as proved by EDS mapping (Figure 2.39a). Accordingly, as shown in Figure 2.39b, **Pt@CdS-0.53mol%** shows a slight increment in the performance. The interesting point is that adding a Pt species generally provokes the self-oxidation of H_2O_2 and dramatically decrease the capacity in photocatalytic H_2O_2 production (Figure 2.42). According to previous literatures, atomically dispersed Pt catalysts in carbon can selectively produce H_2O_2, not following a conventional pathway to produce H_2O. In our case, Pt atoms would be infiltrated within the CdS nanoparticles. On the contrary to this, the S-doped polymeric carbon from **CdS$_{O2,12h}$** might be exploited to interact and disperse an introduced Pt species owing to a high affinity of platinum(II) for sulfur. In this sense, we synthesized **CdS@Pt-0.04mol%** by simply introducing a H_2PtCl_6 methanolic solution to the **CdS$_{O2,12h}$** sample and reducing under 10% H_2/N_2 mixture gas. The material has the similar nano-properties and shows no sign of an aggregation of any Pt species in neither PXRD nor TEM analysis and EDS mapping, and thus significantly improves the photocatalytic H_2O_2 production activity.
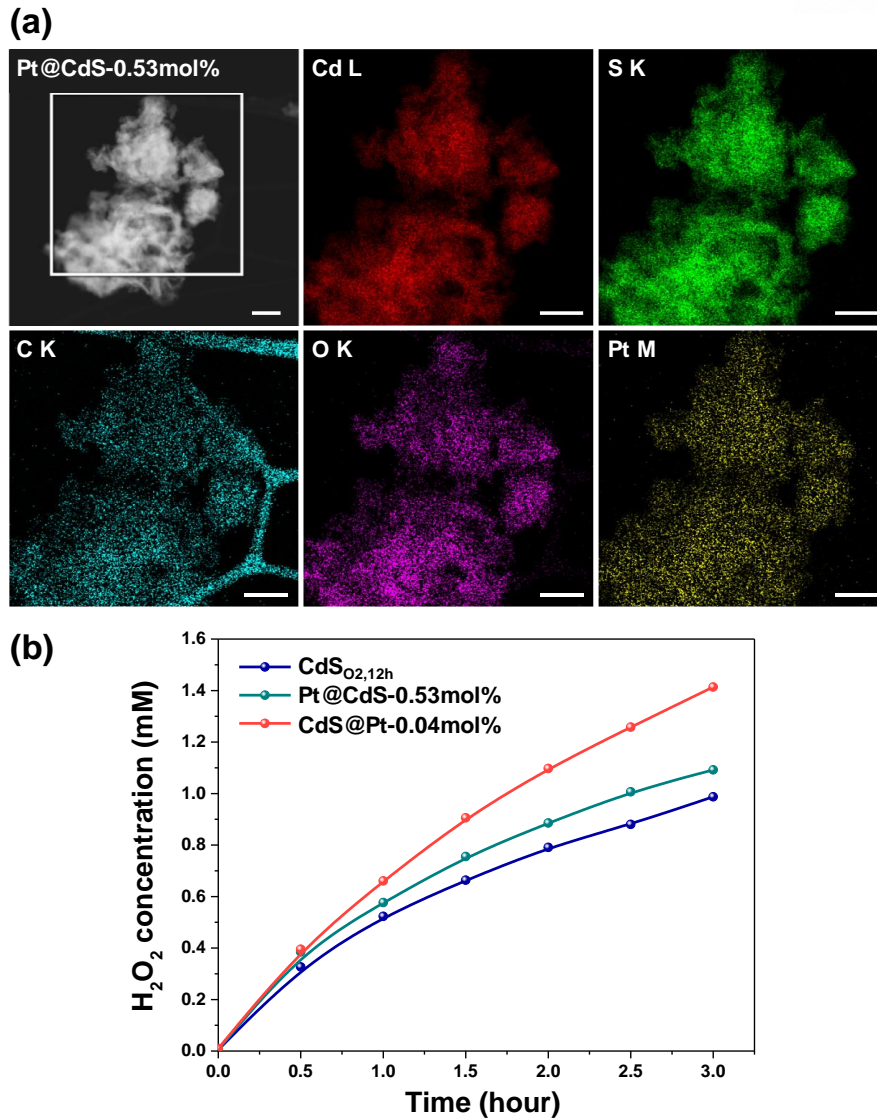
(a)

(b)

Figure 2.39. (a) EDS mapping of **Pt@CdS-0.53mol%**. (b) Photocatalytic H_2O_2 production of **CdS$_{O2,12h}$**, **Pt@CdS-0.53mol%**, and **CdS@Pt-0.04mol%**; under visible light spectrum ($\lambda > 420nm$) in deionized water with 10% 2-propanol as a hole scavenger.
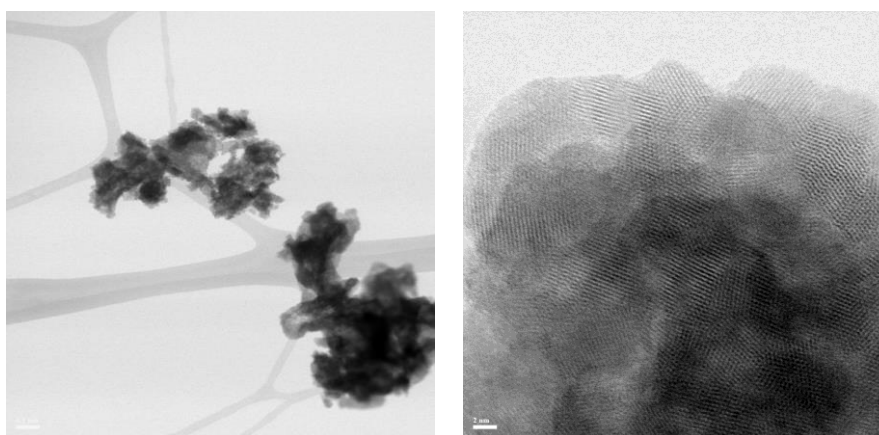
Figure 2.40. TEM images of **Pt@CdS-0.53mol%**.
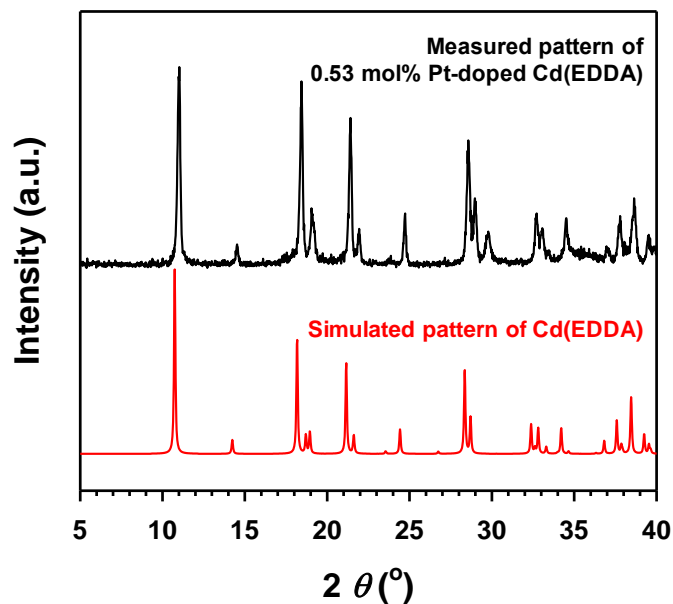
Figure 2.41. XRPD patterns of 0.53 mol% Pt-doped Cd(EDDA): experimental and simulated data from X-ray single-crystal data..
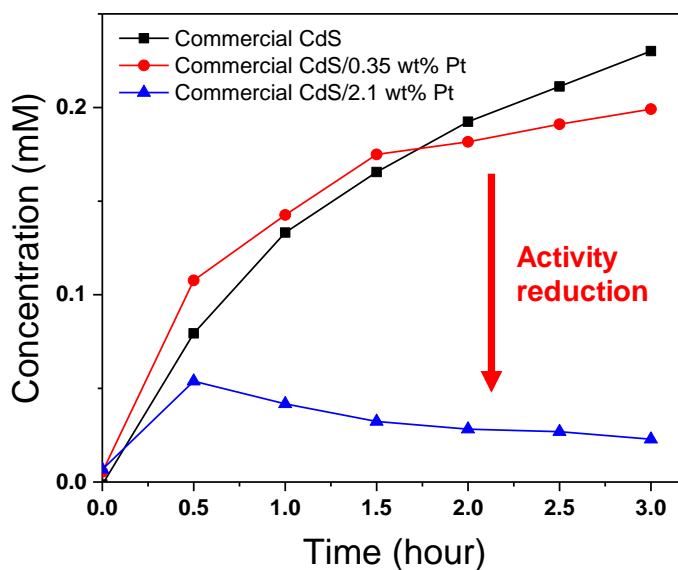
Figure 2.42. Photocatalytic hydrogen peroxide production of Commercial CdS and two other Pt-loaded commercial CdS samples (0.35 and 2.1 wt%, respectively) in a 10% 2-propanol solution.

Conclusion

In conclusion, we reported for the first time the MOF-derived synthesis of CdS photocatalyst covered with carbon for H_2O_2 production under visible spectrum just from H_2O and O_2 even in the absence of hole scavenger and noble metal co-catalyst. Exciting feature of this reported work is the continuous H_2O_2 generation without reaching saturation even after 24 h of continuous photocatalytic

reaction. We have demonstrated that this type of material can show better photocatalytic performance than earlier reported inorganic photocatalysts, and coexistent carbon layers prevent the self-oxidation of photogenerated H_2O_2 by passivating the photocatalyst surface. Thus, through this work, several CdS-based photocatalysts could have been examined to find an optimal photocatalyst after prepared via the MOF-assisted synthesis, and we envision that our results would be able to benefit further visible light-mediated catalytic coupling reactions.[35]

References

1. Y. Yi, L. Wang, G. Li, H. Guo, *Catal. Sci. Technol.* **2016**, *6*, 1593-1610.
2. R. L. Myers, *The 100 Most Important Chemical Compounds: A Reference Guide*, Greenwood Press, Westport, CT, **2007**.
3. T. Nishimi, T. Kamachi, K. Kato, T. Kato, K. Yoshizawa, *Eur. J. Org. Chem.* **2011**, *2011*, 4113-4120.
4. J. M. Campos-Martin, G. Blanco-Brieva, J. L. G. Fierro, *Angew. Chem. Int. Ed.* **2006**, *45*, 6962-6984.
5. Y. Liu, F. Chen, Q. Wang, J. Wang, J. Wang, *Appl. Catal. B* **2018**, *224*, 940-950.
6. J. K. Edwards, B. Solsona, E. N. Ntainjua, A. F. Carley, A. A. Herzing, C. J. Kiely, G. J. Hutchings, *Science* **2009**, *323*, 1037-1041.
7. C. Samanta, *Appl. Catal. A* **2008**, *350*, 133-149.
8. S. Melada, R. Rioda, F. Menegazzo, F. Pinna, G. Strukul, *J. Catal.* **2006**, *239*, 422-430.
9. G.-h. Moon, M. Fujitsuka, S. Kim, T. Majima, X. Wang, W. Choi, *ACS Catal.* **2017**, *7*, 2886-2895.
10. K. Mase, M. Yoneda, Y. Yamada, S. Fukuzumi, *ACS Energy Lett.* **2016**, *1*, 913-919.
11. H.-i. Kim, O. S. Kwon, S. Kim, W. Choi, J.-H. Kim, *Energy Environ. Sci.* **2016**, *9*, 1063-1073.
12. G.-h. Moon, W. Kim, A. D. Bokare, N.-e. Sung, W. Choi, *Energy Environ. Sci.* **2014**, *7*, 4023-4028.
13. Y. Shiraishi, S. Kanazawa, D. Tsukamoto, A. Shiro, Y. Sugano, T. Hirai, *ACS Catal.* **2013**, *3*, 2222-2227.
14. D. Friedmann, C. Mendive, D. Bahnemann, *Appl. Catal. B* **2010**, *99*, 398-406.
15. M. Mrowetz, E. Selli, *New J. Chem.* **2006**, *30*, 108-114.
16. V. Maurino, C. Minero, G. Mariella, E. Pelizzetti, *Chem. Commun.* **2005**, *2005*, 2627-2629.
17. M. C. Lee, W. Choi, *J. Phys. Chem. B* **2002**, *106*, 11818-11822.
18. D. Tsukamoto, A. Shiro, Y. Shiraishi, Y. Sugano, S. Ichikawa, S. Tanaka, T. Hirai, *ACS Catal.* **2012**, *2*, 599-603.
19. H. Kobayashi, M. Teranishi, R. Negishi, S.-i. Naya, H. Tada, *J. Phys. Chem. Lett.* **2016**, *7*, 5002-5007.
20. M. Teranishi, S.-i. Naya, H. Tada, *J. Am. Chem. Soc.* **2010**, *132*, 7850-7851.
21. R. Cai, Y. Kubota, A. Fujishima, *J. Catal.* **2003**, *219*, 214-218.
22. H. Hirakawa, S. Shiota, Y. Shiraishi, H. Sakamoto, S. Ichikawa, T. Hirai, *ACS Catal.* **2016**, *6*, 4976-4982.
23. Y. Kofuji, S. Ohkita, Y. Shiraishi, H. Sakamoto, S. Tanaka, S. Ichikawa, T. Hirai, *ACS Catal.* **2016**, *6*, 7021-7029.
24. Y. Shiraishi, Y. Kofuji, H. Sakamoto, S. Tanaka, S. Ichikawa, T. Hirai, *ACS Catal.* **2015**, *5*, 3058-3066.
25. Y. Shiraishi, S. Kanazawa, Y. Kofuji, H. Sakamoto, S. Ichikawa, S. Tanaka, T. Hirai, *Angew. Chem. Int. Ed.* **2014**, *53*, 13454-13459.
26. X. Wang, S. Blechert, M. Antonietti, *ACS Catal.* **2012**, *2*, 1596-1606.
27. C. Jiang, X. Xu, M. Mei, F.-n. Shi, *ACS Sustainable Chem. Eng.* **2018**, *6*, 854-861.
28. S. Han, Y.-C. Pu, L. Zheng, L. Hu, J. Z. Zhang, X. Fang, *J. Mater. Chem. A* **2016**, *4*, 1078-1086.
29. R. E. Stephens, B. Ke, D. Trivich, *J. Phys. Chem.* **1955**, *59*, 966-969.

30. C. H. Choi, M. Kim, H. C. Kwon, S. J. Cho, S. Yun, H.-T. Kim, K. J.J. Mayrhofer, H. Kim, M. Choi, *Nat. Commun.* **2016**, *7*, 10922.

31. C. H. Choi, H. C. Kwon, S. Yook, H. Shin, H. Kim, M. Choi, *J. Phys. Chem. C* **2014**, *118*, 30063-30070.

32. K. J. Lee, J. H. Lee, S. Jeoung, H. R. Moon, *Acc. Chem. Res.* **2017**, *50*, 2684-2692.

33. K. J. Lee, Y. J. Sa, Y. Jeong, C. W. Bielawski, S. H. Joo, H. R. Moon, *Chem. Commun.* **2015**, *51*, 6773-6776.

34. Crystal data for $Cd_1C_6H_8O_4S_2$, M_r = 320.64, *Orthorhombic*, space group $P2_12_12$ (no. 18), a = 9.4797(19), b = 5.6883(11), c = 8.2300(16) Å, α = 90°, V = 443.79(15) Å^3, Z = 2, d_{calcd} = 2.400 g cm^{-3}, T = 173(2) K, crystal size 0.175 x 0.06 x 0.04 mm^3, λ = 0.71073 Å, 2θ range = 55.00, 60 parameters, R_1 = 0.0160 ($I > 2\sigma(I)$, 1015 reflections), wR_2 = 0.0294 (all data, 4304 reflections), GOF = 1.110.

35. T. Mitkina, C. Stanglmair, W. Setzer, M. Gruber, H. Kisch, B. König, *Org. Biomol. Chem.* **2012**, *10*, 3556-3561.

2.5. Facile synthesis of nanostructured transition metal/ceria solid solutions via bimetallic MOF

Introduction

Ceria (CeO_2) has been studied as a catalyst for many reactions such as the water gas shift reaction,[1] water splitting,[2] oxidation of carbon monoxide (CO),[3] and conversion of nitrogen oxide.[4] The catalytic potential stems from its high oxygen storage capacity that originates from the formation of oxygen vacancies, and the low redox potential between Ce^{4+} and Ce^{3+}.[5,6] However, pure ceria has only a limited amount of anion defects, and often shows severe agglomeration of crystalline domains due to its instability at high temperature. Hence, the oxygen storage capacity of CeO_2 is reduced. An attractive alternative is forming a solid solution of ceria with other cations.[7-9] The physicochemical properties of the resulting material, such as thermal stability, oxygen vacancies, and redox properties can be tuned by the doping metals to achieve superior catalytic performance.[7-15] So far, approaches to synthesize transition-metal-substituted ceria solid solutions include co-precipitation,[10,11] combustion,[12] sol-gel,[13] excess-solution impregnation,[14] and hydrothermal methods.[15] Nevertheless, these methods often cause the segregation/agglomeration of the transition metal oxide phase from ceria, thereby preventing the formation of homogeneous solid solutions with the intended nanostructures.

Conversion reactions that transform mixed-metal coordination compounds into multi-metal/metal oxide nanomaterials have emerged as a new synthetic approach in material chemistry.[16-24] In coordination compounds, the closely and periodically positioned hetero-metal ions enable the formation of homogeneous solid solutions. Recently, Yang and coworkers synthesized transition-metal-substituted CeO_2 nanoparticles (NPs) with a diameter of 3 nm, using solution-based pyrolysis of bimetallic Schiff base complexes as precursors.[24] Since cerium ions and other transition metal ions are placed close to each other in these complexes, the conversion reaction produced $M_{0.1}Ce_{0.9}O_{2-x}$ (M = Mn, Fe, Co, Ni, Cu) NPs with homogeneous phase. However, in this solution-based (wet chemistry) reaction, the use of surfactants is necessary to stabilize the small NPs, while a surfactant-free surface is critical for the accessibility of reagent molecules in catalytic applications.[25-29] Therefore, the surfactant-assisted NPs prepared by Yang et al. require a subsequent annealing step for use as catalysts. Furthermore, nanostructured materials with hierarchical porosity are of great interest in catalysis, due to their efficient mass transport of large molecules and the accessible pores where the reaction could take place.[25-29] The nanoporous structure also gives rise to a large surface area that expose more catalytically active sites. Thus, transition metal-ceria solid solutions with nanoporous structures and composed of nanocrystalline

frameworks would be desirable catalysts due to the large number of active surface oxygen atoms and fast mass transfer.

Our group has intensely studied the pyrolysis of well-designed coordination compounds, especially metal-organic frameworks (MOFs), as suitable precursors for nanoporous metal oxides.[30-33] Among these compounds, Ce-*aph*-MOF with introduced adipate as an aliphatic ligand could be converted into nanoporous CeO_2 (*np*-CeO_2) with highly nanocrystalline frameworks, in which the adipate ligand acts as a self-template that evaporates later to generate nanopores.[33] In the present work, we exploit this transformation, i.e., pyrolysis of bimetallic coordination polymers (CPs), to prepare nanoporous structures consisting of nanocrystalline frameworks of transition metal-ceria solid solution (*np*-$TM_xCe_{1-x}O_{2-\delta}$; TM = Ni, Co, Fe, and Mn, Figure 2.43), without the need for additional surfactants or templates. The resulting structures with 4-nm-sized nanocrystalline frameworks have different physical and chemical properties from those of pure ceria, due to the well-dispersed Mn species within, as evidenced by H_2-temperature-programmed reduction (TPR) studies. The CO oxidation results indicate that the homogeneous phase of *np*-$Mn_xCe_{1-x}O_{2-\delta}$ increased the catalytic activity by an order of magnitude compared to pure ceria.
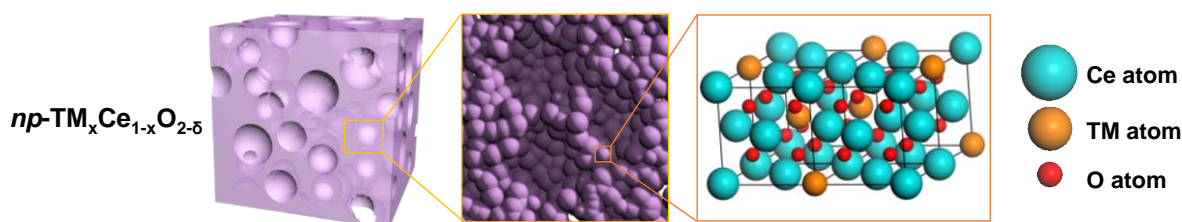

Figure 2.43. Schematic of the nanoporous structure of *np*-$TM_xCe_{1-x}O_{2-\delta}$ (TM = Mn, Ni, Co, and Fe).

Experimental section

All chemicals and solvents were of reagent grade and used without further purification. Infrared spectra were recorded with a ThermoFisher Scientific iS10 FT-IR spectrometer. Elemental analyses were performed at the UNIST Central Research Facilities Center in Ulsan National Institute of Science and Technology (UNIST). Raman spectroscopy measurements were performed using a micro-Raman system (WITec) with an excitation energy of 2.41 eV (532 nm). Thermogravimetric analysis (TGA) was performed under N_2 (g) at a scan rate of 5 °C/min (TGA Q50, TA instruments). Transmission electron microscopy (TEM) images and energy-dispersive X-ray spectrometry (EDS) mapping were obtained on a JEOL JEM-2100 microscope. X-ray powder diffraction (XRPD) data of *imp*-CeO_2-Mn(X) materials were recorded on a Bruker D8 advance diffractometer at 40 kV and 40 mA for Cu Kα radiation (λ = 1.54050 Å), with a step size of 0.02° in 2θ. For the other materials, the XRPD data were recorded on a Bruker D2 phaser diffractometer at 30 kV and 10 mA for Cu Kα radiation (λ = 1.54050

Å), with a step size of 0.02° in 2θ. X-ray photoelectron spectroscopy (XPS) analysis was performed using a Thermo Scientific K-Alpha XPS spectrometer. The chemical composition of np-$Mn_xCe_{1-x}O_{2-\delta}$ samples was analyzed by inductively coupled plasma-mass spectrometry (ICP-MS, ELAN DRC-e, Perkin Elmer). N_2 sorption isotherms were obtained by a BELSORP-max instrument at 77 K. Prior to the adsorption measurements, sample materials converted from CPs were evacuated ($p < 10^{-5}$ mbar) at 150 °C for 6 h. The specific surface area was determined in the relative pressure range from 0.05 to 0.3 of the Brunauer-Emmett-Teller (BET) plot, and the total pore volume was calculated from the amount adsorbed at a relative pressure of about 0.98-0.99.

Table 2.3. Experimental details for the preparation of coordination compounds.

Sample Name[b]	$Ce(NO_3)_3 \cdot 6H_2O$ (mmol)	Transition metal precursor[a] (mmol)	Adipic acid (mmol)	TEA (mmol)
Ce-*aph*-CP	8	0	12	30
$Mn_{0.11}Ce_{0.89}$-*aph*-CP	7.2	0.8	11.6	29
$Mn_{0.22}Ce_{0.78}$-*aph*-CP	6.4	1.6	11.2	28
$Mn_{0.53}Ce_{0.47}$-*aph*-CP	4	4	10	25
$Ni_{0.10}Ce_{0.90}$-*aph*-CP	7.2	0.8	11.6	29
$Co_{0.11}Ce_{0.89}$-*aph*-CP	7.2	0.8	11.6	29
$Fe_{0.11}Ce_{0.89}$-*aph*-CP	7.2	0.8	12	30

[a] $Mn(NO_3)_2 \cdot 4H_2O$ was used as a Mn precursor.
 $Ni(NO_3)_2 \cdot 6H_2O$ was used as a Ni precursor.
 $Co(NO_3)_2 \cdot 6H_2O$ was used as a Co precursor.
 $Fe(NO_3)_3 \cdot 9H_2O$ was used as a Fe precursor.
[b] The sample names of bimetallic CPs are designated based on the ICP results.

Preparation of bimetallic CPs. An ethanol (40 mL) solution of adipic acid (1.75 g, 12 mmol) and *N,N,N*-triethylenediamine (TEA, 4.2 mL, 30 mmol) was added to an ethanol solution (40 mL) of $Ce(NO_3)_3 \cdot 6H_2O$ (3.47 g, 8 mmol) under vigorous stirring. A white precipitate was formed soon after the two solutions were mixed. After vigorous stirring for 2 h, the synthesized product was collected by centrifugation (5000 rpm, 10 min). The as-obtained sample was washed several times with fresh ethanol. After drying in vacuo at 80 °C overnight, 2.39 g of Ce-*aph*-CP was obtained as a white powder. Yield (based on the used amount of Ce^{3+}): 76%. FT-IR (ATR, cm^{-1}): ν_{OH} = 3345(br); $\nu_{C-H(aliphatic)}$ = 2937, 2870 (w); $\nu_{O-C=O(carboxylate)}$ = 1522, 1406(s). Anal. Calcd for $Ce_2C_{18}H_{32}O_{16}$ ($Ce_2(adipate)_3 \cdot 4H_2O$): C, 27.55; H, 4.11; N, 0.00. Found: C, 27.24; H, 3.76; N, 0.00. The synthetic procedures for the other bimetallic CPs were the same, except for the amounts of precursors. A stoichiometric amount of adipic acid and 2.5 times the stoichiometric amount of TEA were used. The amounts of metal precursors and ligands are

summarized in Table 2.3. For $Mn_{0.11}Ce_{0.89}$-*aph*-CP, 2.35 g of white powder was obtained. Yield (based on the used amount of Mn^{2+}): 88%. FT-IR (ATR, cm^{-1}): ν_{OH} = 3354(br); $\nu_{C-H(aliphatic)}$ = 2938, 2869 (w); $\nu_{O-C=O(carboxylate)}$ = 1528, 1408(s). Anal. Calcd for $Mn_{0.11}Ce_{0.89}C_{8.7}H_{14.6}O_{7.3}$ ($Mn_{0.11}Ce_{0.89}(adipate)_{1.45}\cdot1.5H_2O$): C, 28.49; H, 4.01; N, 0.00. Found: C, 27.87; H, 3.81; N, 0.00. For $Mn_{0.22}Ce_{0.78}$-*aph*-CP, 2.09 g of white powder was obtained. Yield (based on the used amount of Mn^{2+}): 85%. FT-IR (ATR, cm^{-1}): ν_{OH} = 3336(br); $\nu_{C-H(aliphatic)}$ = 2938, 2869 (w); $\nu_{O-C=O(carboxylate)}$ = 1529, 1408(s). Anal. Calcd for $Mn_{0.22}Ce_{0.78}C_{8.34}H_{12.72}O_{6.36}$ ($Mn_{0.22}Ce_{0.78}(adipate)_{1.39}\cdot0.8H_2O$): C, 29.80; H, 3.81; N, 0.00. Found: C, 29.82; H, 3.60; N, 0.00. For $Mn_{0.53}Ce_{0.47}$-*aph*-CP, 1.76 g of white powder was obtained. Yield (based on the used amount of Mn^{2+}): 80%. FT-IR (ATR, cm^{-1}): ν_{OH} = 3343(br); $\nu_{C-H(aliphatic)}$ = 2938, 2870 (w); $\nu_{O-C=O(carboxylate)}$ = 1536, 1405(s). Anal. Calcd for $Mn_{0.53}Ce_{0.47}C_{7.44}H_{11.92}O_{5.96}$ ($Mn_{0.53}Ce_{0.47}(adipate)_{1.24}\cdot H_2O$): C, 30.63; H, 4.12; N, 0.00. Found: C, 31.58; H, 4.19; N, 0.00.

Synthesis of np-$M_xCe_{1-x}O_{2-\delta}$ solid solutions. The as-synthesized bimetallic CP (1.00 g) was ground into a powder and then heated at a rate of 5 °C/min under a N_2 (g) flow rate of 100 mL/min. The material was maintained at the target temperature of 500 °C for 6 h. After cooling to room temperature, a second heat treatment was used to remove the organic species to activate the pre-formed pores. The material was heated in an O_2 (g) flow of 100 mL/min at the rate of 1 °C/min, and maintained at the target temperature of 300 °C for 3 h. After cooling to room temperature, the desired solid was obtained. All solids obtained after N_2 treatment were black, whereas the resultant np-CeO_2, np-$Mn_{0.08}Ce_{0.92}O_{2-\delta}$, np-$Mn_{0.18}Ce_{0.82}O_{2-\delta}$, np-$Mn_{0.13}Ce_{0.87}O_{2-\delta}\cdot MnO_y$, np-$Ni_{0.08}Ce_{0.92}O_{2-\delta}$, np-$Co_{0.08}Ce_{0.92}O_{2-\delta}$, and np-$Fe_{0.09}Ce_{0.91}O_{2-\delta}$ after O_2 treatments were pale-yellow, brown, dark-brown, dark-brown, dark-brown, light-brown, and brown powders, respectively.

Synthesis of imp-CeO_2-Mn(X). Imp-CeO_2-Mn(X) samples were prepared using a commercial CeO_2 powder (Rhodia, BET surface area = 133 m^2/g) by an incipient wetness impregnation method. A given amount of $Mn(NO_3)_2\cdot6H_2O$ (determined based on 2 g of CeO_2) was completely dissolved in distilled water (2.3 mL). The aqueous solution was added drop-by-drop to the CeO_2 powder until the mixture turned into a malleable paste. Then the paste was dried in air at 120 °C. These two steps were repeated until the aqueous solution was used up. The resulting sample was calcined in a muffle furnace at 500 °C for 4 h, with a heating rate of 1.6 °C/min. After cooling naturally down to 120 °C in the furnace, the product was moved out to the ambient atmosphere and cooled to room temperature.

Rietveld refinement analysis. For detailed structural analysis, the XRPD data were collected using an EMPYREAN diffractometer (PANanalytical) at Chonnam Center for Research Facilities. The crystallographic information files (CIF) are given in Supporting Information. Cu Kα radiation was utilized with the generator operating at 30 mA and 40 kV. The goniometer and the detector system were ω/2θ and PIXcel[3D] with prefix interface Xenon proportional detector, respectively. The fixed divergence slit had a size of 0.10886° and the receiving slit size was 0.1 mm. The data were obtained at room temperature in reflection mode with spinning, with a step size of 0.0130° for a scan time of 987 s per

step over $2\theta = 3 - 99°$. LeBail refinement of the obtained X-ray diffraction pattern was performed with a pseudo-Voigt function as described in the literature[34], together with a manually interpolated background using the GSAS package[35]. For the Rietveld refinement, the model structure of CeO_2 was employed and the occupancy of Ce was substituted with other incorporated metal, when the isotropic atomic displacement factor was considered. At the final stage of refinement, all structural parameters were refined simultaneously without the constraint. The refinement quality indices R_p, R_{wp}, and R_{exp} all achieved convergence well below 5%.

H_2-TPR and CO-TPD experiments. Prior to the H_2-TPR experiments, 0.05 g of the sample was pre-treated in a fixed bed reactor at 350 °C for 0.5 h under air flow (60 mL/min). Afterwards, the sample was cooled to room temperature under air flow and then purged with 2% H_2/Ar (60 mL/min) for 2 h. After stabilization of the thermal conductivity detector (TCD) signal of the gas chromatograph (GC, Agilent 7820A), the TPR experiment was carried out in 2% H_2/Ar (60 mL/min) flow with a heating rate of 10 °C/min. The amount of H_2 consumption was determined from the TCD signal intensities calibrated using CuO/SiO_2 reference. The CO-temperature-programmed desorption (TPD) experiments were performed after CO adsorption on the samples. 0.05 g of the sample was pre-treated in a fixed bed reactor at 350 °C for 0.5 h under air flow (60 mL/min). After cooling to room temperature under air flow, the sample was purged in He for 0.5 h and then exposed to 1.8% CO/He gas mixture for 0.5 h (66 mL/min), followed by another He purge for 1.5 h in order to remove the weakly-bound CO molecules. Next, the TPD experiment was carried out in a He flow (60 mL/min) with a heating rate of 10 °C/min using a flame ionization detector (FID). The desorbed gases were converted to methane using Ni/Al_2O_3 catalysts with H_2 (20 mL/min) at 400 °C, then flowed directly to the FID without the GC column separation. The desorbed amount was determined from the FID signal intensities, with the FID sensitivity factor calibrated using 500-uL pulses of 10% CO in He. To identify desorbed gas species, CO-TPD experiment was also performed with CaX zeolite as a CO_2 trap, which was installed between the reactor and Ni/Al_2O_3 catalysts.

Catalytic study for CO oxidation. CO oxidation measurements were performed in a quartz flow reactor using 0.01 g of sample supported by quartz wool. The sample was pre-treated at 350 °C for 0.5 h under air flow (60 mL/min), and then cooled to room temperature under air flow. For the temperature-programmed reaction, the air flow was changed to He/O_2 gas (the same as reaction composition), then CO was added to the reaction gas mixture and the temperature was increased at the rate of 5 °C/min. The reaction gas composition was 1.8% CO and 2.3 % O_2 in He (total flow rate = 66 mL/min). The outlet gases were analyzed every 2 min by a GC system (Agilent 7820A) using a HP-PLOT Q column and TCD.

For steady-state activity measurements, the pre-treated sample was heated to target temperature under O_2 in He mixed gas and kept for 1 h for stabilization. After CO gas was added, steady-state activity was measured using same gas composition as described above for 2 h. The turnover frequencies (TOFs)

were calculated based the desorption peaks obtained from the CO-TPD experiments. The apparent activation barrier was evaluated from the steady-state activities collected at 5 different temperatures. The CO conversion was kept below 10%.

Results and discussion

The adipate-based Ce-coordination polymer (Ce-*aph*-CP) is prepared by mixing $Ce(NO_3)_3 \cdot 6H_2O$ with adipic acid ($HOOC(CH_2)_4COOH$) in the presence of TEA at room temperature. This synthetic method allows large-scale production of precursors for the CeO_2 framework, due to the complete deprotonation of carboxylic acid groups and their instant coordination to cations, as evidenced by infrared spectroscopy (Figure 2.44). In the XRPD patterns, the highest peak is located at $2\theta = 9°$ and there is a broad peak at around $26°$. These peaks do not match the previously reported X-ray structures of adipate ligand-based Ce-CPs (Figure 2.45). The Mn^{II}-containing Ce-*aph*-CPs are synthesized via similar methods by adding $Mn(NO_3)_2 \cdot 4H_2O$ to the reaction solution with the molar ratio of $Ce^{III}:Mn^{II}$ being 9:1 (10 mol%), 4:1 (20 mol%), or 1:1 (50 mol%); and a stoichiometric amount of adipic acid is used (Experimental section). By using ICP analysis, the three resultant CPs were found to have the compositions of $Mn_{0.11}Ce_{0.89}$-*aph*-CP, $Mn_{0.22}Ce_{0.78}$-*aph*-CP, and $Mn_{0.53}Ce_{0.47}$-*aph*-CP, respectively.

To determine the optimal pyrolysis condition, TGA was conducted under N_2 atmosphere (Figure 2.46). In the TGA trace of Ce-*aph*-CP, the first weight loss started at around 300 °C. 60% of the mass remained at 500 °C after ligand decomposition. This amount is larger than the corresponding value for pure CeO_2 (42%) which is possible for Ce-*aph*-CP if the N_2 treatment at 500 °C did not remove all carbogenic species to achieve pure nanoporous ceria. Therefore, the thermolysis of Ce-*aph*-CP was performed in two steps: heat treatment at 500 °C under N_2 flow (100 mL/min) for 6 h, followed by calcination at 300 °C under O_2 flow (100 mL/min) for 3 h. From its XRPD patterns, the black solid obtained after the first step was identified as single-phase cubic CeO_2 (JCPDS file no. 81-0792, Figure 2.47). However, it was nonporous due to the residual carbogenic species, as revealed by the N_2 adsorption-desorption measurement (Figure 2.48). The second calcination step successfully activated the pores of CeO_2 by eliminating the organic substances, according to the elemental analysis results (Table 2.4) as well as the pale-yellow color of the product. Both the BET surface area and the total pore volume of the product increased dramatically after O_2 treatment (from 7 to 125 m^2/g and 0.03 to 0.11 mL/g, respectively), indicating the nanoporous structure of *np*-CeO_2 (Figure 2.48). The as-prepared bimetallic CPs, namely $Mn_{0.11}Ce_{0.89}$-*aph*-CP, $Mn_{0.22}Ce_{0.78}$-*aph*-CP, and $Mn_{0.53}Ce_{0.47}$-*aph*-CP, were also thermally converted through the same procedure to synthesize the corresponding nanoporous Mn-doped ceria ($Mn_{0.08}Ce_{0.92}O_{2-\delta}$, $Mn_{0.18}Ce_{0.82}O_{2-\delta}$, and $Mn_{0.13}Ce_{0.87}O_{2-\delta} \cdot MnO_y$). As indicated by the XRPD patterns in Figure 2.49, all prepared *np*-$Mn_xCe_{1-x}O_{2-\delta}$ materials have the same crystalline cubic CeO_2 structure without other crystalline species such as manganese oxides. Even introducing a significant amount of

Mn species did not change this structure, although the peaks shifted to slightly higher angles. Thus, the reactions produced the solid solution phase of ceria with Mn ions, instead of segregated ceria and manganese oxides.
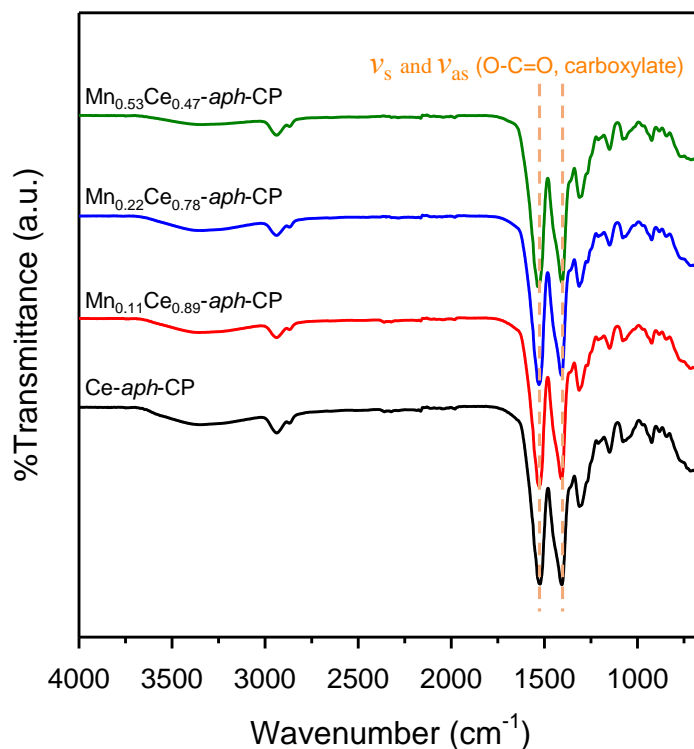

Figure 2.44. FT-IR spectra of four coordination compounds, Ce-*aph*-CP, $Mn_{0.11}Ce_{0.89}$-*aph*-CP, $Mn_{0.22}Ce_{0.78}$-*aph*-CP, and $Mn_{0.53}Ce_{0.47}$-*aph*-CP, measured by using attenuated total reflectance (ATR) technique.
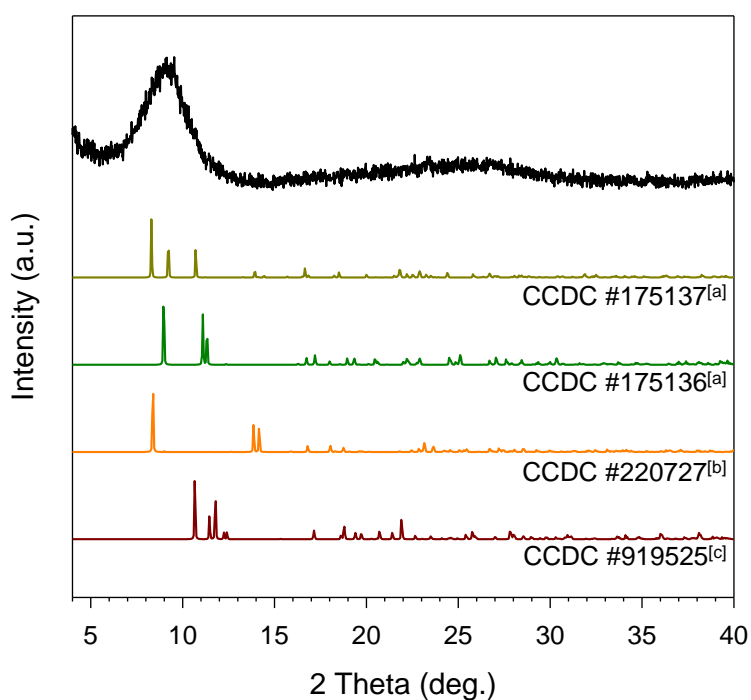
Figure 2.45. XRPD patterns of the coordination compounds constructed with Ce^{3+} and an adipate ligand.

[a] Z.-G. Sun, Y.-P. Ren, L.-S. Long, R.-B. Huang, L.-S. Zheng, *Inorg. Chem. Commun.* **2002**, *5*, 629.
[b] L.-M. Duan, J.-Q. Xu, F.-T. Xie, Y.-B. Liu, Ding, H. *Inorg. Chem. Commun.* **2004**, *7*, 216.
[c] V. S. Dhanya, M. R. Sudarsanakumar, S. Suma, S. W. Ng, M. S. Augustine, S. M. Roy, *Inorg. Chem. Commun.* **2013**, *35*, 140.
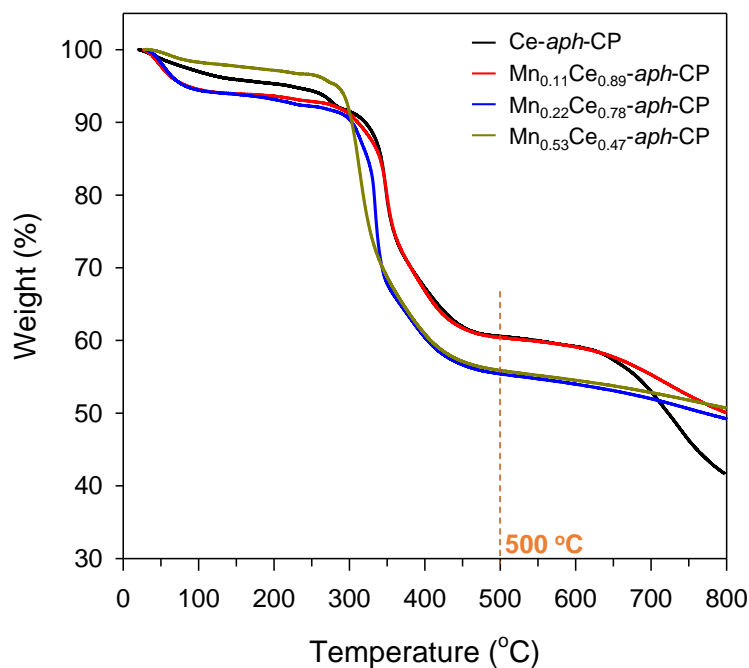
Figure 2.46. TGA traces of four coordination compounds, Ce-*aph*-CP, $Mn_{0.11}Ce_{0.89}$-*aph*-CP, $Mn_{0.22}Ce_{0.78}$-*aph*-CP, and $Mn_{0.53}Ce_{0.47}$-*aph*-CP under N_2 flow.

Table 2.4. Elemental compositions of coordination polymers, resultant materials after thermal conversion but before O_2 treatment, and *np*-$Mn_xCe_{1-x}O_{2-\delta}$ solid solutions based on the elemental combustion analysis.

Sample Name	C (wt%)	H (wt%)	N (wt%)
np-CeO_2 before O_2 treatment	15.21	0.51	0.00
np-$Mn_{0.08}Ce_{0.92}O_{2-\delta}$ before O_2 treatment	19.46	0.61	0.00
np-$Mn_{0.18}Ce_{0.82}O_{2-\delta}$ before O_2 treatment	8.89	0.31	0.00
np-$Mn_{0.13}Ce_{0.87}O_{2-\delta}$·$MnO_y$ before O_2 treatment	14.77	0.41	0.00
np-CeO_2	0.29	0.36	0.00
np-$Mn_{0.08}Ce_{0.92}O_{2-\delta}$	0.46	0.32	0.00

np-Mn$_{0.18}$Ce$_{0.82}$O$_{2-\delta}$	0.30	0.11	0.00
np-Mn$_{0.13}$Ce$_{0.87}$O$_{2-\delta}$·MnO$_y$	0.40	0.06	0.00

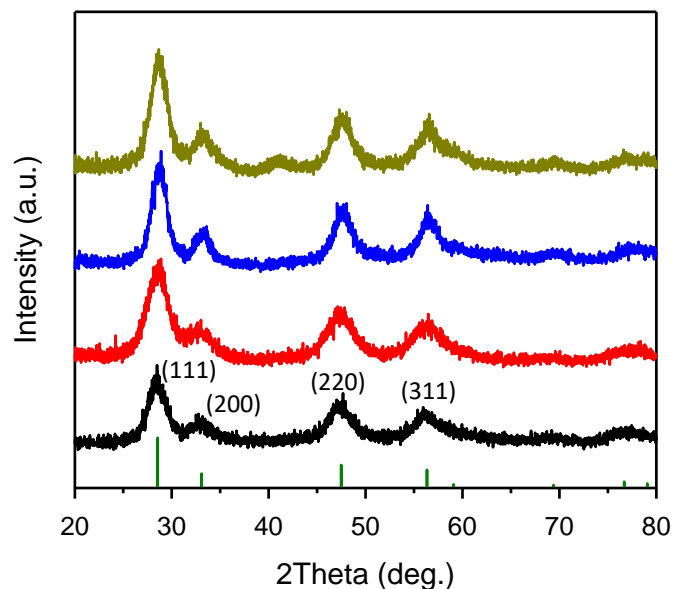**Figure 2.47.** XRPD patterns of black solids obtained after N$_2$ treatment of coordination compounds, Ce-*aph*-CP (black), Mn$_{0.11}$Ce$_{0.89}$-*aph*-CP (red), Mn$_{0.22}$Ce$_{0.78}$-*aph*-CP (blue), and Mn$_{0.53}$Ce$_{0.47}$-*aph*-CP (dark yellow).
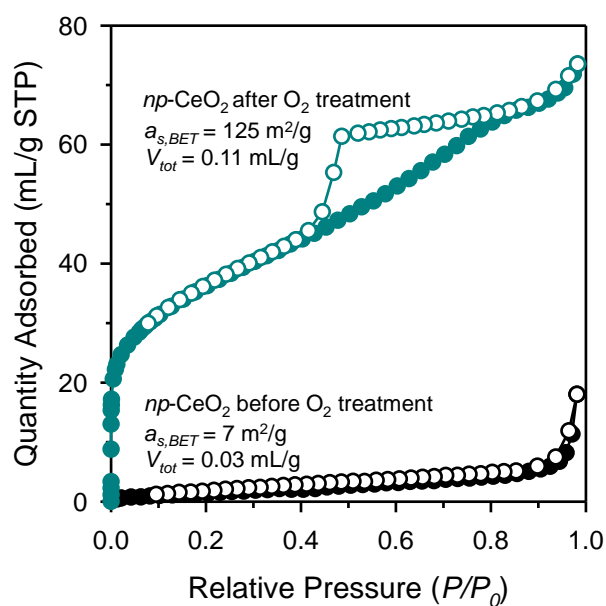

Figure 2.48. Comparison of nitrogen sorption isotherms before (black) and after (cyan) O$_2$ treatment for *np*-CeO$_2$.
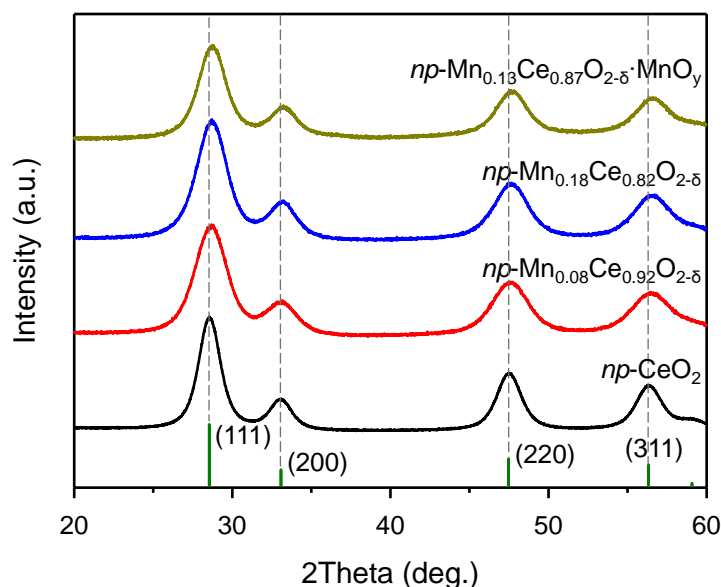
Figure 2.49. XRPD patterns for the prepared np-Mn$_x$Ce$_{1-x}$O$_{2-\delta}$ solid solutions and np-CeO$_2$, together with cubic CeO$_2$ standard card (JCPDS file no. 81-0792).

Table 2.5. Elemental compositions of coordination polymers, resultant materials after thermal conversion but before O$_2$ treatment, and np-Mn$_x$Ce$_{1-x}$O$_{2-\delta}$ solid solutions based on the elemental combustion analysis.

Sample	Fitting Lattice parameter (Å)	Mn (mol%) based on precursor used	Mn/(Mn+Ce) based on ICP	Mn/(Mn+Ce) based on EDS
np-CeO$_2$	5.4132	0	0.00	0.00
np-Mn$_{0.08}$Ce$_{0.92}$O$_{2-\delta}$	5.4107	10	0.10	0.08
np-Mn$_{0.18}$Ce$_{0.82}$O$_{2-\delta}$	5.4093	20	0.20	0.18
np-Mn$_{0.13}$Ce$_{0.87}$O$_{2-\delta}$·MnO$_y$	5.4098	50	0.41	0.46

Rietveld refinement was conducted on the XRPD patterns to examine the structures of np-Mn$_x$Ce$_{1-x}$O$_{2-\delta}$. As mentioned above, the peak shift caused by Mn doping represents the contraction of the ceria lattice, because the Mn ion has a smaller ionic radius than the cerium ion in the lattice. Indeed, the fitting lattice parameters of the three bimetallic samples obtained by Rietveld refinement analysis are 5.4107, 5.4093, and 5.4098 Å for 10, 20, and 50 mol% Mn doping, respectively (Table 2.5); all of which are smaller than those of np-CeO$_2$ (5.4132 Å) and bulk CeO$_2$ (5.4124 Å). Based on these results, the Mn mole fractions substituted into the ceria lattice were calculated as Mn$_{0.08}$Ce$_{0.92}$O$_{2-\delta}$, Mn$_{0.18}$Ce$_{0.82}$O$_{2-}$

$_\delta$, and $Mn_{0.13}Ce_{0.87}O_{2-\delta}$, respectively. For 10 and 20 mol% doping, the amounts of incorporated Mn ions obtained from ICP and EDS analysis are in good agreement with those calculated from Rietveld refinement, demonstrating the homogeneous nature of the solid solutions. However, with 50 mol% Mn doping, incomplete replacement of Ce by Mn in the lattice was observed compared with the actual compositions based on ICP and EDS results. This may arise from the solubility limit of Mn in the ceria lattice, and the residual Mn ions may form manganese oxide clusters in the solid solution phase (*np*-$Mn_{0.13}Ce_{0.87}O_{2-\delta} \cdot MnO_y$).[36] However, the XRPD pattern failed to show certain phases of manganese oxides, which can be attributed to the low crystallinity of manganese oxides, or the existence of very small clusters of manganese oxides well distributed in the solid solution matrix.

The broad peaks in the XRPD patterns imply a nanocrystalline nature. The average sizes of nanocrystals in *np*-CeO_2, *np*-$Mn_{0.08}Ce_{0.92}O_{2-\delta}$, *np*-$Mn_{0.18}Ce_{0.82}O_{2-\delta}$, and *np*-$Mn_{0.13}Ce_{0.87}O_{2-\delta} \cdot MnO_y$ were estimated as 4.1, 3.2, 3.3, and 3.6 nm, respectively, by applying the Debye-Scherrer equation to the (111) reflections. The nanocrystalline framework of *np*-CeO_2 induces lattice expansion due to the high dislocation densities, leading to a larger lattice parameter than that of bulk CeO_2 (5.4132 versus 5.4124 Å).[37] This effect is also visible in the $Mn_xCe_{1-x}O_{2-\delta}$ solid solutions, which have slightly larger lattice parameters than the reported values of other $Mn_xCe_{1-x}O_{2-\delta}$ solid solutions with similar amounts of doping.[15,38-40] TEM images in Figure 2.50 further show that nanoparticles comprise the wall of the nanoporous structure. The clear lattice fringes in the high-resolution TEM images (insets) indicate that the solid solutions are constructed from 3–4 nm-sized nanocrystals with ceria lattice. The EDS results also indicate that the Mn ions are well-dispersed throughout the CeO_2 matrix (Figures 2.51).
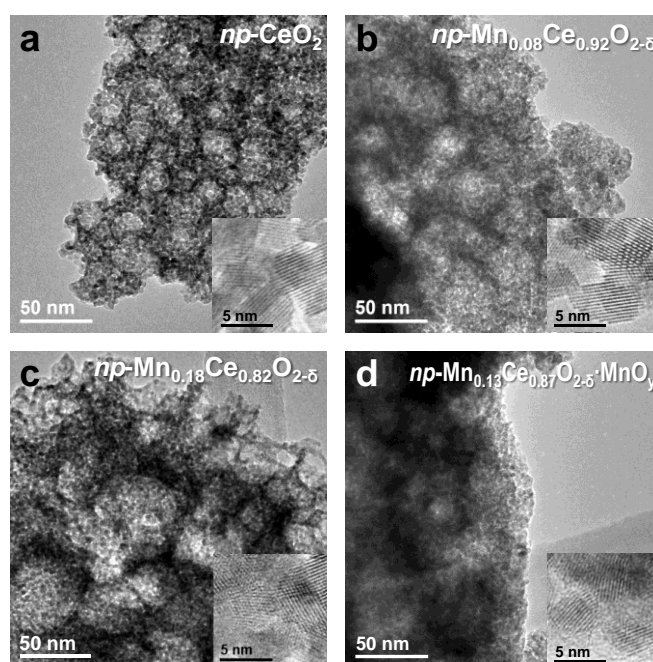
Figure 2.50. TEM images for (a) np-CeO$_2$, (b) np-Mn$_{0.08}$Ce$_{0.92}$O$_{2-\delta}$ solid solution, (c) np-Mn$_{0.18}$Ce$_{0.82}$O$_{2-\delta}$ solid solution, and (d) np-Mn$_{0.13}$Ce$_{0.87}$O$_{2-\delta}$·MnO$_y$.
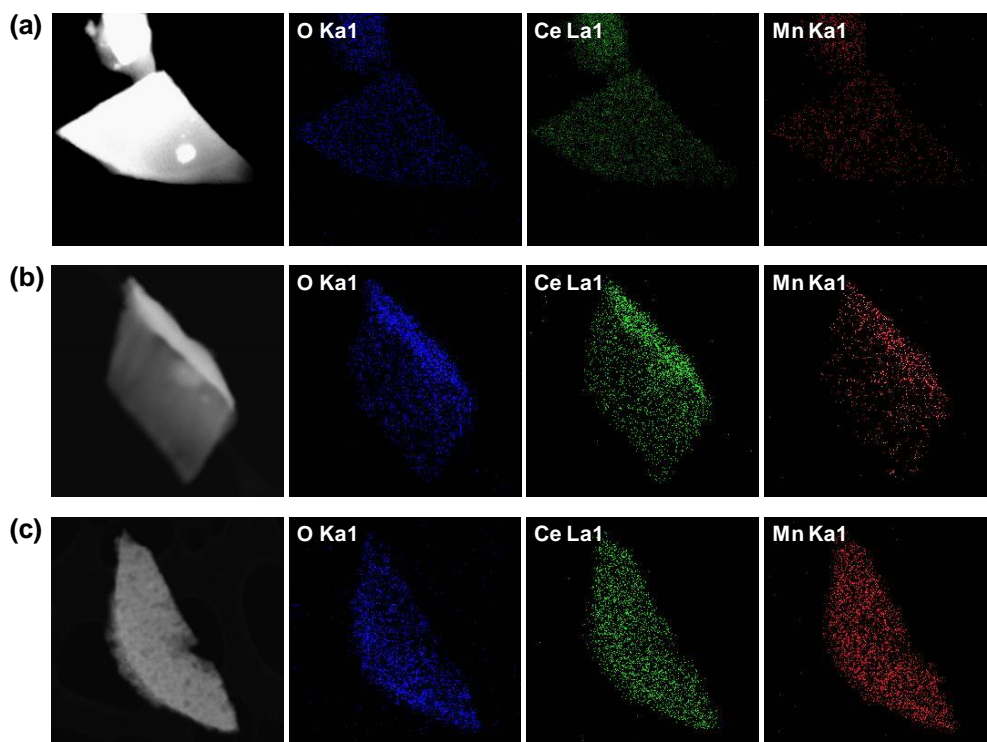
Figure 2.51. EDS mapping of (a) np-Mn$_{0.08}$Ce$_{0.92}$O$_{2-\delta}$ solid solution, (b) np-Mn$_{0.18}$Ce$_{0.82}$O$_{2-\delta}$ solid solution, and (c) np-Mn$_{0.13}$Ce$_{0.87}$O$_{2-\delta}$·MnO$_y$.

To assess the porosity of np-CeO$_2$ with and without the Mn doping, nitrogen adsorption-desorption measurements were conducted. As shown in Figure 2.52, all four materials showed typical type IV isotherms with H2 type hysteresis loop over the relative pressure range of $0.44 < P/P_0 < 0.99$. Such isotherms are characteristic of cage-like pore structures with well-developed mesopores. The pore size distributions were obtained by using nonlocal density functional theory (NLDFT) algorithm. The distribution curves (Figure 2.53) indicated micropores as well as mesopores, with a broad pore size distribution from 2 to ~ 100 nm. The BET surface areas for np-CeO$_2$, np-Mn$_{0.08}$Ce$_{0.92}$O$_{2-\delta}$, np-Mn$_{0.18}$Ce$_{0.82}$O$_{2-\delta}$, and np-Mn$_{0.13}$Ce$_{0.87}$O$_{2-\delta}$·MnO$_y$ were 125, 149, 127, and 68 m^2/g, respectively, which are comparable to the value of ordered mesoporous CeO$_2$ produced by using a nanocasting approach.[41,42] The increased surface area in np-Mn$_{0.08}$Ce$_{0.92}$O$_{2-\delta}$ compared with np-CeO$_2$ may be attributed to either the replacement of Ce by the lighter Mn, or the lower density of the incorporated manganese oxide (2.8–5.4 g/cm^3) relative to CeO$_2$ (7.2 g/cm^3).[43] However, the specific surface area decreased at higher Mn doping levels (np-Mn$_{0.18}$Ce$_{0.82}$O$_{2-\delta}$), which might result from the combined effects of previously mentioned factors and increased partial destruction of the np-CeO$_2$ nanoporous structure.[43] Furthermore,

the severely reduced surface area in np-$Mn_{0.13}Ce_{0.87}O_{2-\delta} \cdot MnO_y$ is consistent with the existence of discrete domains of manganese oxides that do not add to the surface area.

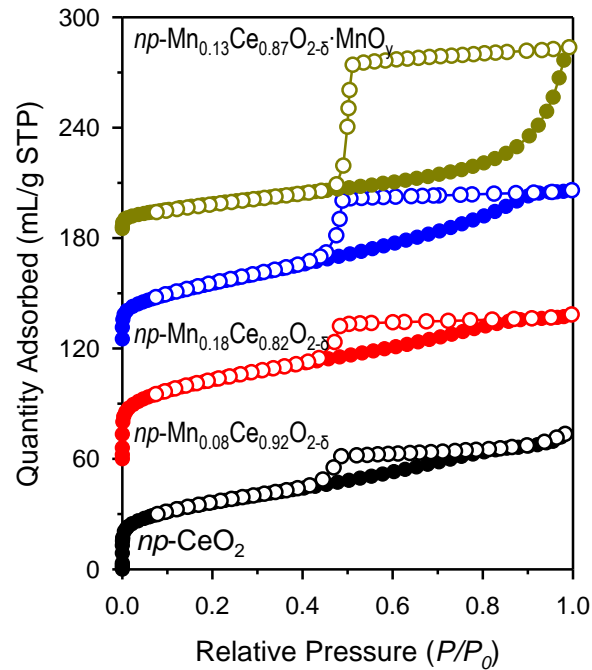**Figure 2.52.** N_2 sorption isotherms for np-CeO_2 and np-$Mn_xCe_{1-x}O_{2-\delta}$ samples. For clarity, the top three curves were offset by 60, 120, and 180 mL/g.
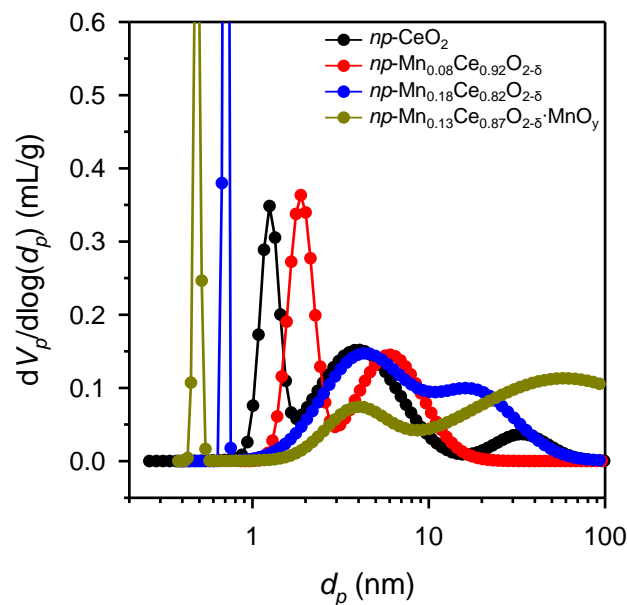

Figure 2.53. NLDFT pore size distribution curves of np-$Mn_xCe_{1-x}O_{2-\delta}$ solid solutions as well as np-CeO_2.

The structures of Mn-doped ceria materials and np-CeO$_2$ were further studied by Raman spectroscopy (Figure 2.54a). In all samples, the main peak at around 460 cm^{-1} was attributed to the F$_{2g}$ vibration mode of the cubic fluorite structure of CeO$_2$.[44,45] However, this band became broader and red-shifted slightly with increased amount of Mn doping. The peak broadening originated from the increased defect concentration. The peak shift was associated with the contracted fluorite lattice structure of CeO$_2$ upon the formation of solid solutions, in good agreement with the Rietveld refinement results.[44,45] The additional weak, broad band at near 602 cm^{-1} was caused by the defect species of MnO$_8$-type complex that include a dopant cation in 8-fold coordination of O^{2-}.[46,47] As more Mn ions were substituted into the ceria lattice, this band became more distinct. In np-Mn$_{0.13}$Ce$_{0.87}$O$_{2-\delta}$·MnO$_y$, a new peak at 647 cm^{-1} was observed. This peak revealed the coexistence of segregated manganese oxide, since its peak wavelength corresponds to the most intense A$_g$ mode of the Mn$_5$O$_8$ phase.[48] Thus, a Mn doping level of 50% leads to the formation of Mn$_5$O$_8$ that could not be detected in the XRPD patterns, in addition to the Mn$_{0.13}$Ce$_{0.87}$O$_{2-\delta}$ solid solution.

The oxidation states of Mn species were examined by XPS analysis. The Mn 3s XPS spectra (Figure 2.54b) revealed that the amount of 3s multiplet splitting (ΔE_{3s}) gradually decreased from 5.6 to 5.3 eV with increasing Mn content in the solid solution. According to previous reports, these ΔE_{3s} values show that np-Mn$_{0.08}$Ce$_{0.92}$O$_{2-\delta}$ contains mixed Mn^{2+} and Mn^{3+}, while np-Mn$_{0.18}$Ce$_{0.82}$O$_{2-\delta}$ and np-Mn$_{0.13}$Ce$_{0.87}$O$_{2-\delta}$·MnO$_y$ contain mostly Mn^{3+}.[49] The change from mixed Mn^{2+}/Mn^{3+} to mainly Mn^{3+} with increasing Mn content up to 50 mol% is attributed to the enhanced local lattice distortion as more oxygen vacancies were created.[24] Meanwhile, the peak with lower binding energy gradually shifted to even lower with increasing Mn doping content, which is different from the case of bulk MnO$_x$.[30] This chemical shift is ascribed to the charge transfer between Mn and Ce, which might be affected by the structure of the homogeneous Mn-Ce-O solid solution.[50,51]
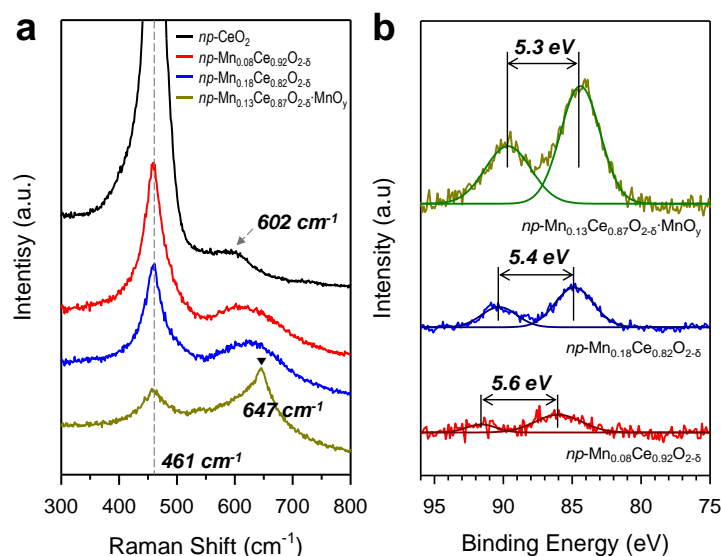
Figure 2.54. (a) Raman spectra of the np-$Mn_xCe_{1-x}O_{2-\delta}$ series and np-CeO_2. (b) Mn 3s XPS spectra of np-$Mn_xCe_{1-x}O_{2-\delta}$ solid solutions.
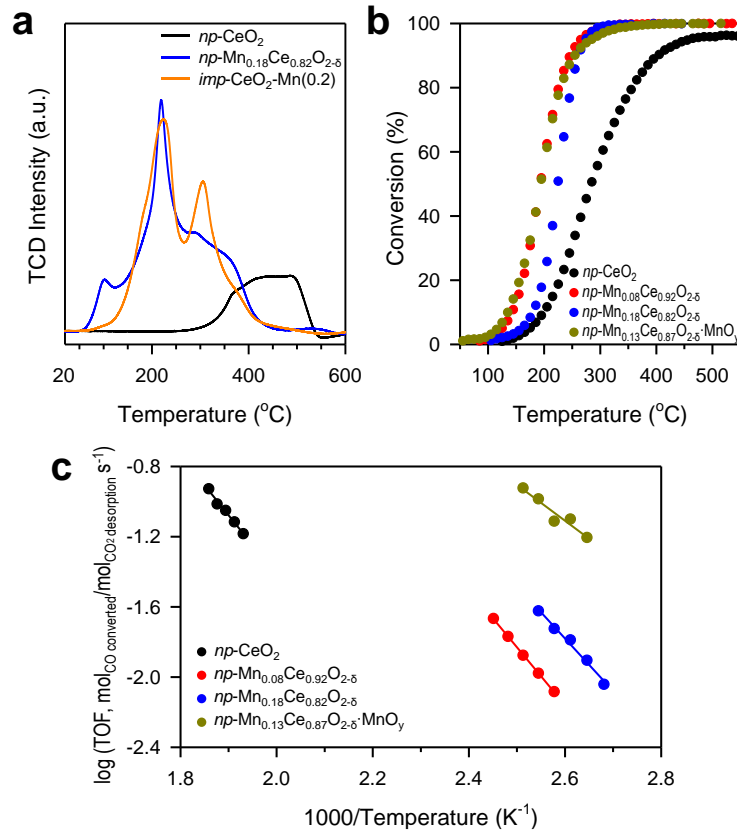
Figure 2.55. (a) H_2-TPR profiles for np-CeO_2, np-$Mn_{0.18}Ce_{0.82}O_{2-\delta}$, and imp-CeO_2-Mn(0.2) samples. (b) CO oxidation curves of np-CeO_2 as well as the np-$Mn_xCe_{1-x}O_{2-\delta}$ series. (c) Arrhenius plots of CO oxidation with pure CeO_2 and np-$Mn_xCe_{1-x}O_{2-\delta}$ samples.

Figure 2.56. TEM images for the imp-CeO_2-Mn(0.2).

The modified electronic states due to the Mn ion substitution into CeO_2 lead to different reduction behavior of solid solutions compared to segregated MnO_x-CeO_2 mixture, as evidenced by the H_2-TPR

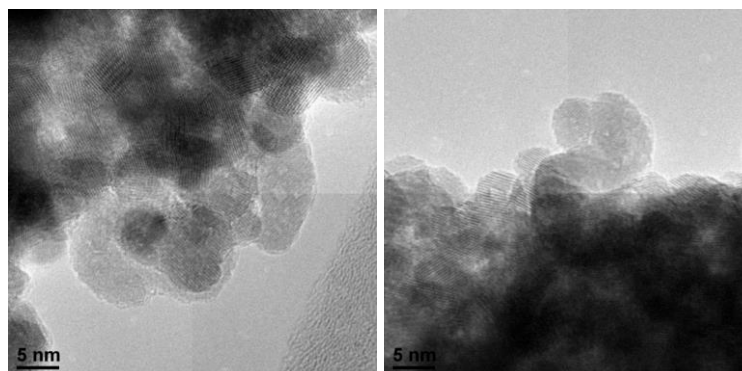measurement results (Figure 2.55a). The reference samples of MnO_x-CeO_x mixed oxides were prepared by an incipient wetness impregnation method, using $Mn(NO_3)_2 \cdot 6H_2O$ as the precursor with a commercial CeO_2 powder.[52] The Mn content was matched to those in the np-$M_xCe_{1-x}O_{2-\delta}$ solid solutions, and the samples were designated as imp-CeO_2-Mn(X) (X: mole fraction of Mn to Ce, X = 0.1, 0.2, and 0.5). In these samples, MnO_x was found to be dispersed on the surface of CeO_2, as shown in the TEM images (Figure 2.56). In the corresponding XRPD patterns, no peak shift from the CeO_2 diffraction was observed, implying that the impregnation method yielded the segregated mixture of MnO_x and CeO_2 instead of a homogeneous solid solution (Figure 2.57). Interestingly, np-CeO_2, np-$Mn_{0.18}Ce_{0.82}O_{2-\delta}$, and imp-CeO_2-Mn(0.2) all displayed significantly different reduction behaviors in their H_2-TPR profiles (Figure 5a). The profile of np-CeO_2 exhibits a broad reduction peak from 300 to 550 °C, in good agreement with previous observation in pure ceria.[53] Imp-CeO_2-Mn(0.2) shows two major peaks. According to previous reports, the earlier peak at 220 °C corresponds to the reduction of MnO_2/Mn_2O_3 of poor crystallinity to Mn_3O_4 among the highly dispersed surface manganese species.[40] The other peak at around 300 °C can be assigned to the reduction of Mn_3O_4 to MnO, along with the reduction of CeO_2 on the surface.[40] In contrast, np-$Mn_{0.18}Ce_{0.82}O_{2-\delta}$ has an additional peak with a low onset temperature (around 55 °C) and the maximum at 100 °C, both being the lowest temperatures observed for manganese oxide reduction so far. This phenomenon is not fully understood yet, but might be attributed to the Mn-O-Ce bond originated from the homogeneous solid solution of highly dispersed Mn species in nanocrystalline CeO_2, which lowers the reduction potential of Mn ions.[25] While np-$Mn_{0.08}Ce_{0.92}O_{2-\delta}$ displays the same reduction behavior, the np-$Mn_{0.13}Ce_{0.87}O_{2-\delta} \cdot MnO_y$ sample containing segregated manganese oxides shows a trend that closely resembles the impregnated sample (Figure 2.58). Thus, as we expected, the facile conversion of bimetallic CPs successfully doped Mn ions into np-CeO_2, thereby altered the material's physical and chemical properties.
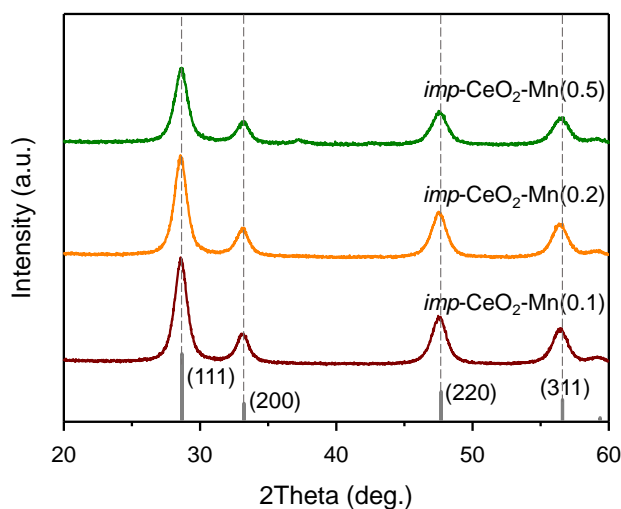

Figure 2.57. XRPD patterns for the imp-CeO_2-Mn materials with cubic CeO_2 standard card (JCPDS file no. 81-0792).
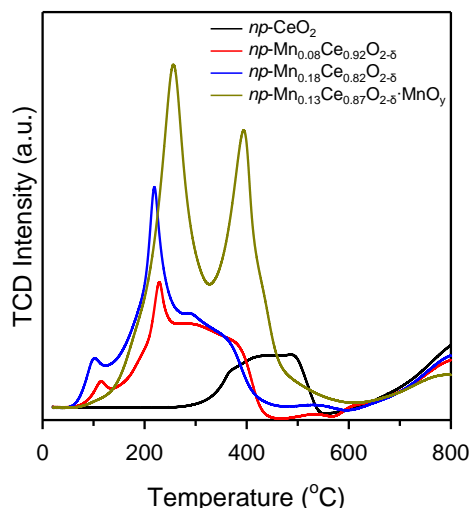
Figure 2.58. H_2-TPR profiles for *np*-CeO_2 as well as *np*-$Mn_xCe_{1-x}O_{2-\delta}$ solid solutions.

Table 2.6. Activation energy (E_a) of CO oxidation on *np*-CeO_2 and *np*-$Mn_xCe_{1-x}O_{2-\delta}$ solid solutions.

Sample	E_a (kJ/mol)
np-CeO_2	65
np-$Mn_{0.08}Ce_{0.92}O_{2-\delta}$	63
np-$Mn_{0.18}Ce_{0.82}O_{2-\delta}$	57
np-$Mn_{0.13}Ce_{0.87}O_{2-\delta}\cdot MnO_y$	39
Mn_2O_3 (commercial)	64

Table 2.7. Summary of CO-TPD of *np*-$Mn_xCe_{1-x}O_{2-\delta}$ solid solutions.

Sample	Number of Mn[a] (10^{-3} mol/g)	Desorption amount of CO_2 (10^{-4} mol/g)
np-$Mn_{0.08}Ce_{0.92}O_{2-\delta}$	0.6	2.0
np-$Mn_{0.18}Ce_{0.82}O_{2-\delta}$	1.3	1.8
np-$Mn_{0.13}Ce_{0.87}O_{2-\delta}\cdot MnO_y$	2.6	0.4

[a] Number of Mn was calculated based on ICP analysis.

The catalytic activities of the *np*-$Mn_xCe_{1-x}O_{2-\delta}$ samples were investigated by the catalytic oxidation of CO to CO_2. This reaction is a benchmark in heterogeneous catalysis, a continuing subject of fundamental mechanistic studies, as well as of practical importance in many industrial processes. The light-off curves for CO oxidation are presented in Figure 2.55b. As expected from their structures, the

Mn-doped np-$Mn_xCe_{1-x}O_{2-\delta}$ samples exhibited superior catalytic activity compared to np-CeO_2, as evidenced by a lower CO conversion temperature. The value of T_{50} (temperature for 50% conversion) was 195 °C for np-$Mn_{0.08}Ce_{0.92}O_{2-\delta}$ and np-$Mn_{0.13}Ce_{0.87}O_{2-\delta}\cdot MnO_y$, 225 °C for np-$Mn_{0.18}Ce_{0.82}O_{2-\delta}$, and 285 °C for np-CeO_2. Therefore, the substitution of aliovalent Mn into ceria enhanced the mobility of the lattice oxygen atoms.[40] The Arrhenius plot for CO oxidation is shown in Figure 2.55c, and the activation energy (E_a) values are summarized in Table 2.6. It should be noted here that turnover frequencies (TOFs) were calculated based on all desorption peaks over the entire temperature range in the CO-TPD experiment (Figure 2.59 and Table 2.7). While the profiles for all np-$Mn_xCe_{1-x}O_{2-\delta}$ samples showed a broad peak from 50 °C to 350 °C, the kinetic study was conducted in a much narrower temperature range (100–130 °C). Thus, the number of effective active sites on the catalysts is possibly overestimated, and the TOF underestimated accordingly.
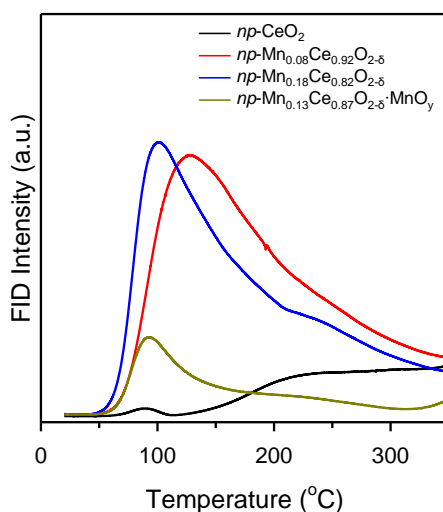

Figure 2.59. CO-TPD profiles for np-CeO_2 as well as np-$Mn_xCe_{1-x}O_{2-\delta}$ solid solutions.

Overall, our results indicate that the substitution of Mn in CeO_2 promoted CO oxidation by at least one order of magnitude, suggesting that the reaction mostly takes place on the active Mn-O sites. The effect of the Mn doping level on the catalytic performance was also studied. As shown in Table 2.6, E_a was lowered as the Mn content increased from 10 to 50 mol%, and these values are significantly lower than that of commercial Mn_2O_3. This result implies the synergistic interaction between MnO_x and ceria at the solid-solution interface.[26] The reason is that the introduction of Mn of lower valence and multiple oxidation states could enhance the reactivity of ceria, by facilitating the migration of oxygen atoms toward the active sites of Mn-O bond through the CeO_2 lattice, thus serving as an oxygen reservoir.[54] Interestingly, the sample with the lowest activation energy ($Mn_{0.13}Ce_{0.87}O_{2-\delta}\cdot MnO_y$, below 40 kJ/mol) has an intermediate level of Mn doping. The segregated MnO_y phase could possibly act as a catalyst by itself to lower the E_a value for CO oxidation.[55,56]
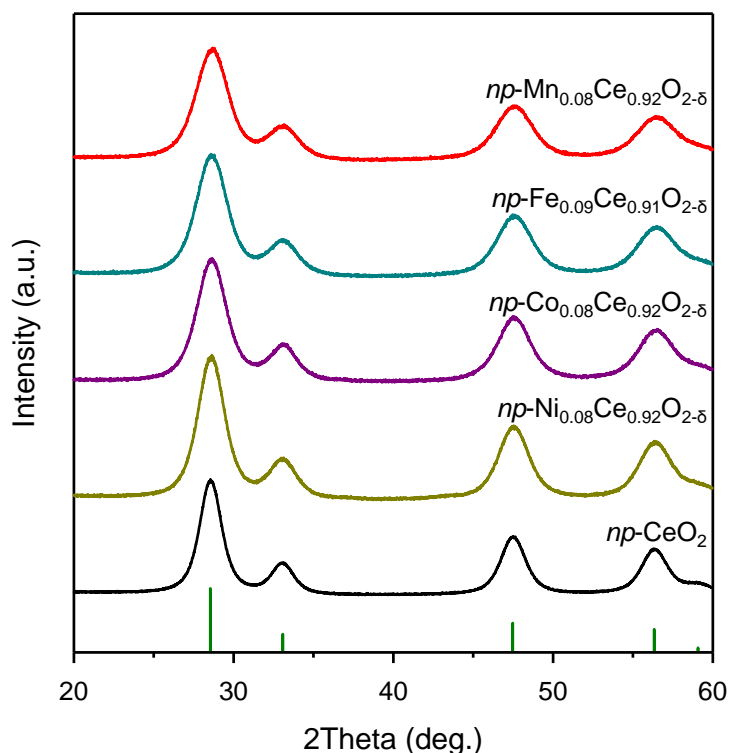
Figure 2.60. XRPD patterns of the np-$TM_xCe_{1-x}O_{2-\delta}$ series (TM = Ni, Co, Fe, and Mn) and np-CeO_2.

Furthermore, this synthetic strategy was successfully extended to three other transition metals, namely iron, cobalt, and nickel. The products (np-$TM_xCe_{1-x}O_{2-\delta}$) with 10 mol% doping all displayed the cubic CeO_2 phase, as shown in Figure 2.60. Based on Rietveld refinement analysis, the fitting lattice parameters of these samples were 5.4086, 5.4102, and 5.4127 Å for Fe, Co, and Ni doping, respectively (Table 2.8); and all these values are comparable to the previous reports.[57-59] From these results, the mole fractions of the substituted transition metal ions into the ceria lattice were calculated as $Fe_{0.09}Ce_{0.91}O_{2-\delta}$, $Co_{0.08}Ce_{0.92}O_{2-\delta}$, and $Ni_{0.08}Ce_{0.92}O_{2-\delta}$. ICP and EDS quantitative analyses also indicated consistent compositions, confirming the successful synthesis of homogeneous np-$Fe_{0.09}Ce_{0.91}O_{2-\delta}$, np-$Co_{0.08}Ce_{0.92}O_{2-\delta}$, and np-$Ni_{0.08}Ce_{0.92}O_{2-\delta}$ solid solutions. Their TEM images (Figure 2.61) exhibited nanoporous structures composed of 3 nm-sized nanoparticles, in agreement with the average crystalline size (~3.3 nm) estimated by applying the Debye-Scherrer equation to the (111) reflections (Table S8). EDS mapping results indicated that the Fe, Co, and Ni ions were also well-dispersed in the materials (Figure 2.62). Furthermore, all materials exhibited the hierarchical porous structure of micro- and mesopores as shown in Figure 2.63. The BET surface areas of np-$Ni_{0.08}Ce_{0.92}O_{2-\delta}$, np-$Co_{0.08}Ce_{0.92}O_{2-\delta}$, and np-$Fe_{0.09}Ce_{0.91}O_{2-\delta}$ were 171, 194, and 144 m^2/g, respectively; all higher than that of np-CeO_2 (Table 2.10). Therefore, all the np-$M_xCe_{1-x}O_{2-\delta}$ (M = Ni, Co, Fe, and Mn) samples exhibited hierarchical nanoporous structure composed of highly crystalline nanoparticles 3 nm in size.

Table 2.8. The results of Rietveld refinement and quantitative analysis of ICP and EDS for np-$M_xCe_{1-x}O_{2-\delta}$ solid solutions.

Sample	Fitting lattice parameter (Å)	M (mol%) based on precursor used	M/(M+Ce) based on ICP	M/(M+Ce) based on EDS
np-$Fe_{0.09}Ce_{0.91}O_{2-\delta}$	5.4086	10	0.10	0.08
np-$Co_{0.08}Ce_{0.92}O_{2-\delta}$	5.4102	10	0.10	0.09
np-$Ni_{0.08}Ce_{0.92}O_{2-\delta}$	5.4127	10	0.11	0.09

Table 2.9. Crystalline size for np-$M_xCe_{1-x}O_{2-\delta}$ series (M = Ni, Co, Fe and Mn) calculated by applying the Debye-Scherrer equation to the (111) reflection.

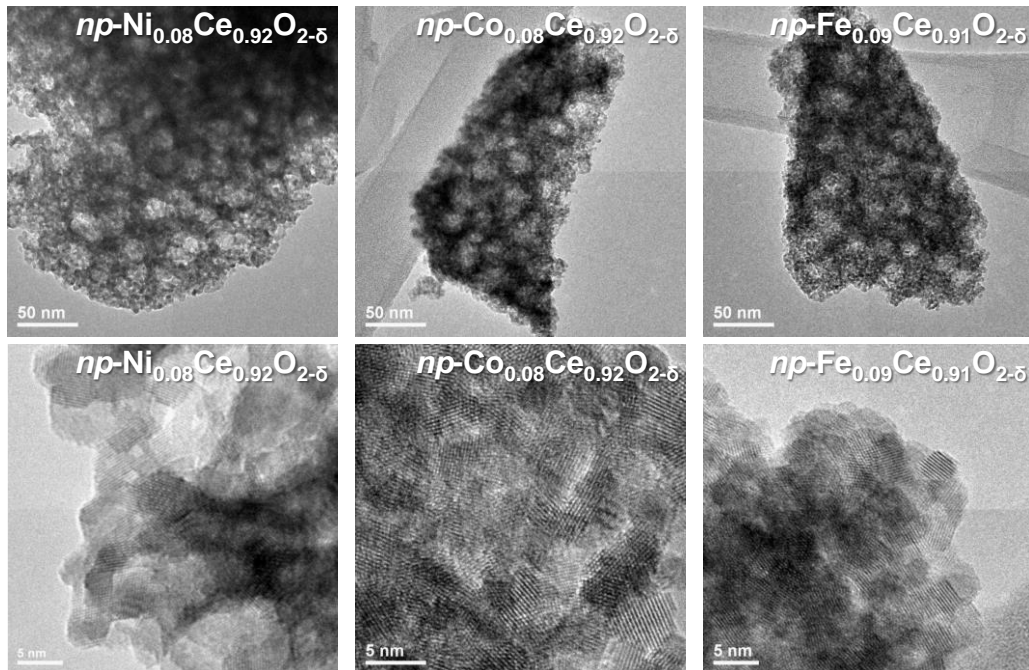| Sample	NP size (nm)
np-$Mn_{0.08}Ce_{0.92}O_{2-\delta}$	3.2
np-$Fe_{0.09}Ce_{0.91}O_{2-\delta}$	3.3
np-$Co_{0.08}Ce_{0.92}O_{2-\delta}$	3.4
np-$Ni_{0.08}Ce_{0.92}O_{2-\delta}$	3.7
np-CeO_2	4.1

Figure 2.61. TEM images for converted np-$Ni_{0.08}Ce_{0.92}O_{2-\delta}$, np-$Co_{0.08}Ce_{0.92}O_{2-\delta}$ and np-$Fe_{0.09}Ce_{0.91}O_{2-\delta}$ solid solutions.
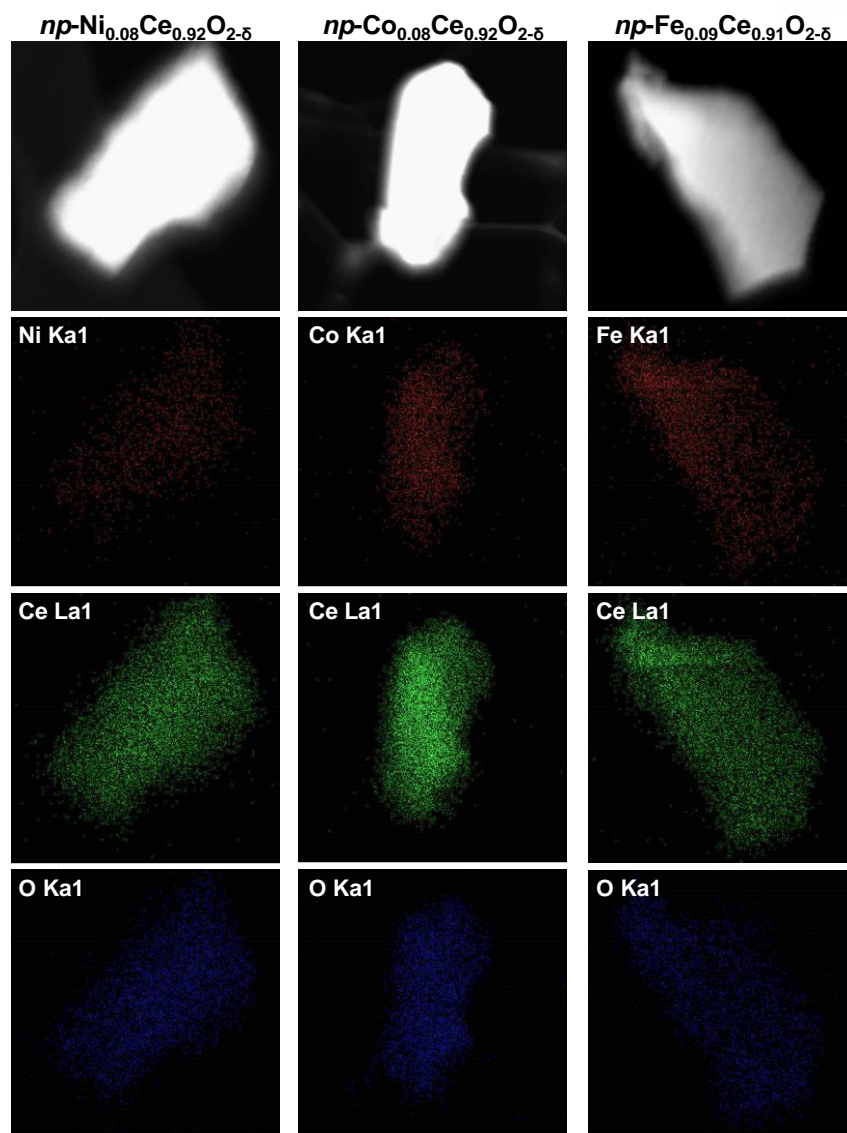
Figure 2.62. EDS mapping for np-$Ni_{0.08}Ce_{0.92}O_{2-\delta}$, np-$Co_{0.08}Ce_{0.92}O_{2-\delta}$ and np-$Fe_{0.09}Ce_{0.91}O_{2-\delta}$.

Table 2.10. Summary of N_2 sorption isotherms of the np-$M_xCe_{1-x}O_{2-\delta}$ series.

Sample	$a_{s,BET}$[a] (m²/g)	V_{tot}[b] (mL/g)	V_{micr}[c] (mL/g)	V_{meso}[d] (mL/g)
np-$Mn_{0.08}Ce_{0.92}O_{2-\delta}$	149	0.12	0.08	0.04
np-$Fe_{0.09}Ce_{0.91}O_{2-\delta}$	144	0.13	0.07	0.06
np-$Co_{0.08}Ce_{0.92}O_{2-\delta}$	194	0.17	0.10	0.07
np-$Ni_{0.08}Ce_{0.92}O_{2-\delta}$	171	0.17	0.08	0.09
np-CeO_2	125	0.11	0.06	0.05

[a] The specific surface area ($a_{s,BET}$) was calculated by Brunauer-Emmet-Teller (BET) method.
[b] V_{tot} represented the total pore volume at $P/P_0 = 0.99$.
[c] The micropore volume (V_{micro}) was determined by applying Dubinin-Astakhov (DA) analysis.
[d] The mesopore volume (V_{meso}) was obtained by subtracting the microporous volume from total volume.

Figure 2.63. N_2 sorption isotherms for np-$M_xCe_{1-x}O_{2-\delta}$ series and np-CeO_2. For clarity, the isotherm curves for np-$Ni_{0.08}Ce_{0.92}O_{2-\delta}$, np-$Co_{0.08}Ce_{0.92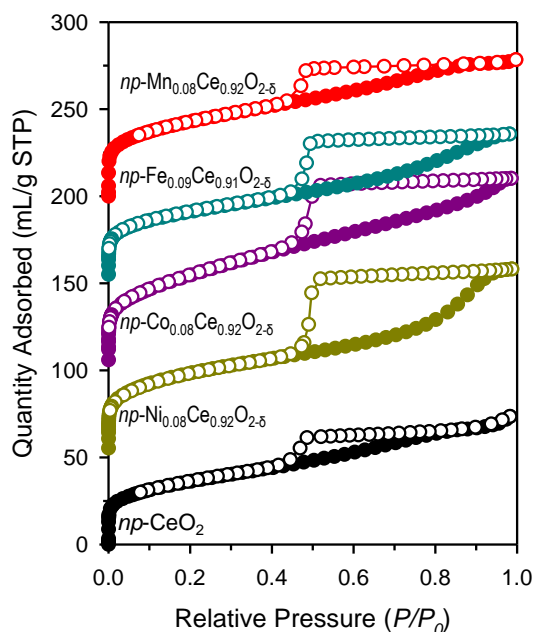}O_{2-\delta}$, np-$Fe_{0.09}Ce_{0.91}O_{2-\delta}$ and np-$Mn_{0.08}Ce_{0.92}O_{2-\delta}$ were offset by 50, 100, 150 and 200 mL/g, respectively.

Conclusion

In conclusion, we have developed a facile and general synthetic method for transition metal-ceria solid solutions with nanosized particles and hierarchical nanoporous structures (np-$TM_xCe_{1-x}O_{2-\delta}$; TM = Mn, Ni, Co, and Fe). This method employs the conversion reactions of bimetallic aliphatic-ligand-based CPs to successfully produce homogeneous substitution of transition metal ions into the ceria lattice, as proven by the XRPD and Rietveld refinement analysis results. The prepared np-$Mn_xCe_{1-x}O_{2-\delta}$ solid solutions showed that their doping amounts and catalytic properties could be easily adjusted by tuning the CPs while preserving their nanostructures. The properties of the solid solutions were characterized by TEM, N_2 sorption, Raman spectroscopy, and XPS. In particular, the homogeneity of the solid solutions affected their altered physicochemical properties, as evidenced by the H_2-TPR measurement results. In addition, the Mn species in the np-$Mn_xCe_{1-x}O_{2-\delta}$ solid solutions were responsible for increasing the catalytic activity for CO oxidation by an order of magnitude compared to pure ceria. We envisage that this approach can enrich the possible structures and compositions of nanoporous solid solutions with nanocrystalline frameworks and inspire further studies of MOF/CP conversion reactions.

References

1. Q. Fu, H. Saltsburg, M. Flytzani-Stephanopoulos, *Science* **2013**, *301*, 935-938.
2. W. C. Chueh, C. Falter, M. Abbott, D. Scipio, P. Furler, S. M. Haile, A. Steinfeld, *Science* **2010**, *330*, 1719-1801.
3. Z. Wu, M. Li, S. H. Overbury, *J. Catal.* **2012**, *285*, 61-73.
4. T. Nagata, K. Miyajima, F. Mafuné, *J. Phys. Chem. A* **2015**, *119*, 10225-10263.
5. E. Mamontove, T. Egami, R. Brezny, M. Koranne, S. Tyagi, *J. Phys. Chem. B* **2000**, *104*, 11110-11116.
6. D. Martin, D. Duprez, *J. Phys. Chem.* **1996**, *100*, 9429-9438.
7. F. Wnag, W. Li, W. Feng, D. Liu, Y. Zhang, *Chem. Sci.* **2016**, *7*, 1867-1873.
8. P. Fornasiero, R. D. Monte, G. R. Rao, J. Kašpar, S. Meriani, A. Trovarelli, M. Graziani, *J. Catal.* **1995**, *151*, 168-177.
9. M. Mogensen, N. M. Sammes, G. A. Tompsett, *Solid State Ionics* **2000**, *129*, 63-94.
10. L. Katta, P. Sudarsanam, G. Thrimurthulu, B. M. Reddy, *Appl. Catal., B.* **2010**, *101*, 101-108.
11. B. Mallesham, P. Sudarsanam, B. V. S. Reddy, B. M. Reddy, *Appl. Catal., B.* **2016**, *181*, 47-57.
12. B. Delimaris, T. Ioannides, *Appl Catal., B.* **2009**, *89*, 295-302.
13. M. Epifani, T. Andreu, S. Abdollahzadeh-Ghom, J. Arbiol, J. R. Morante, *Adv. Funct. Mater.* **2012**, *22*, 2867-2875.
14. D. Gamarra, A. Martínez-Arias, *J. Catal.* **2009**, *263*, 189-195.
15. D. Jampaiah, P. Venkataswamy, V. E. Coyle, B. M. Reddy, S. K. Bhargava, *RSC Adv.* **2016**, *6*, 80541-80548.
16. S. Chen, M. Xue, Y. Li, Y. Pan, L. Zhu, D. Zhang, Q. Fang, S. Qiu, *Inorg. Chem. Front.* **2015**, *2*, 177-183.
17. S. Li, N. Wang, Y. Yue, G. Wang, Z. Zu, Y. Zhang, *Chem. Sci.* **2015**, *6*, 2495-2500.
18. S. Chenn, M. Xue, Y. Li, Y. Pan, L. Zhu, S. Qiu, *J. Mater. Chem. A.* **2015**, *3*, 20145-20152.
19. Y. Li, Y.-X. Zhou, X. Ma, H.-L. Jiang, *Chem. Commun.* **2016**, *52*, 4199-4202.
20. J. Tang, R. R. Salunkhe, J. Liu, N. L. Torad, M. Imura, S. Furukawa, Y. Yamauchi, *J. Am. Chem. Soc.* **2015**, *137*, 1572-1580.
21. X. Ma, Y.-X. Zhou, H. Liu, Y. Li, H.-L. Jiang, *Chem. Commun.* **2016**, *52*, 7719-7722.
22. L. Jiao, Y.-X. Zhou, H.-L. Jiang, *Chem. Sci.* **2016**, *7*, 1690-1695.
23. J. Zhao, F. Wang, P. Su, M. Li, J. Chen, Q. Yang, C. Li, *J. Mater. Chem.* **2012**, *22*, 13328-13333.
24. J. S. Elias, M. Risch, L. Giordano, A. N. Mansour, Y. Shao-Horn, *J. Am. Chem. Soc.* **2014**, *136*, 17193-17200.
25. L. Lu, A. Eychmüller, *Acc. Chem. Res.* **2008**, *41*, 244-253.
26. P. Zhang, H. Lu, Y. Zhou, L. Zhang, Z. Wu, S. Yang, H. Shi, Q. Zhu, Y. Chen, S. Cai, *Nat. Commun.* **2015**, *6*, 8446.
27. G. Kim, J. M. Kim, C.-H. Lee, J. Han, B.-H. Jeong, J.-K. Jeon, *J. Nanosci. Nanotechnol.* **2016**, *16*, 9153-9159.
28. M. K. Sheehan, M. Rudden, H. Cai, C.-K. Tsung, *Catal. Lett.* **2016**, *146*, 309-318.
29. H. I. Lee, Y. Y. Lee, D.-U. Kang, K. Lee, Y.-U. Kwon, J. M. Kim, *Sci. Rep.* **2016**, *6*, 21496.
30. J. H. Lee, Y. J. Sa, T. K. Kim, H. R. Moon, S. H. Joo, *J. Mater. Chem. A* **2014**, *2*, 10435–10443.
31. K. J. Lee, T.-H. Kim, T. K. Kim, J. H. Lee, H.-K. Song, H. R. Moon, *J. Mater. Chem. A* **2014**, *2*, 14393-14400.
32. J. H. Lee, B. Moon, T. K. Kim, S. Jeoung, H. R. Moon, *Dalt. Trans.* **2015**, *44*, 15130–15134.
33. T. K. Kim, K. J. Lee, J. Y. Cheon, J. H. Lee, S. H. Joo, H. R. Moon, *J. Am. Chem. Soc.* **2013**, *135*, 8940–8946.
34. C. J. Howard, *J. Appl. Cryst.* **1982**, *15*, 615-620.
35. B. H. Toby, *J. Appl .Cryst.* **2001**, *34*, 210-213.
36. X. Wu, Q. Liang, D. Weng, J. Fan, R. Ran, *Catal. Today* **2007**, *126*, 430-435.
37. L. Chen, P. Fleming, V. Morris, J. D. Holmes, M. A. Morris, *J. Phys. Chem. C* **2010**, *114*, 12909-12919.
38. B. Murugan, A. V. Ramaswamy, *Chem. Mater.* **2005**, *17*, 3983-3993.
39. Q. Liang, X. Wu, D. Weng, H. Xu, *Catal. Today* **2008**, *139*, 113-118.

40. P. Venkataswamy, K. N. Rao, D. Jampaiah, B. M. Reddy, *Appl. Catal., B* **2015**, *162*, 122-132.

41. Q. Wang, Y. Zhang, Y. Zhou, Z. Zhang, J. Wue, Y. Xu, C. Zhang, X. Sheng, N. Kui, *RSC Adv.* **2016**, *6*, 730-739.

42. P. Ji, J. Zhang, F. Chen, M. Anpo, *J. Phys. Chem. C* **2008**, *112*, 17809-17813.

43. V. I. Markoulaki, I. T. Papadas, I. Kornarakis, G. S. Armatas, *Nanomaterials* **2015**, *5*, 1971-1984.

44. M. Li, U. Tumuluri, Z. Wu, S. Dai, *ChemSusChem.* **2015**, *8*, 3651-3660.

45. D. Qiao, G. Lu, X. Liu, Y. Guo, Y. Wang, Y. Guo, *J. Mater. Sci.* **2011**, *46*, 3500-3506.

46. T. Taniguchi, T. Watanabe, N. Sugiyama, A. K. Subramani, H. Wagata, N. Matsushita, M. Yoshimura, *J. Phys. Chem. C* **2009**, *113*, 19789-19793.

47. L. Li, F. Chen, J.-Q. Lu, M.-F. Luo, *J. Phys. Chem. A* **2011**, *115*, 7972-7977.

48. C. B. Azzoni, M. C. Mozzati, P. Galinetto, A. Paleari, V. Massarotti, D. Capsoni, M. Bini, *Solid State Commun.* **1999**, *112*, 375-378.

49. J. Q. Torres, J.-M. Giraudon, J.-F. Lamonier, *Catal. Today* **2011**, *176*, 277-280.

50. J. A. Anderon, M. F. García, Characterization of Supported Metal Catalysts by Spectroscopic Techniques. In *Supported Metals in Catalysis*; Hutchings, G. J., Eds.; Imperical College Press, London, **2012**, *vol. 11*, pp 128.

51. J. M. Cerrato, M. F. Hochella, W. R. Jr. Knocke, A. M. Dietrich, T. F. Cromer, *Environ. Sci. Technol.* **2010**, *44*, 5881-5886.

52. S. Chang, M. Li, Q. Hua, L. Zhang, Y. Ma, B. Ye, Y. Huang, *J. Catal.* **2012**, *293*, 195-204.

53. X. Tang, Y. Li, X. Huang, Y. Xu, H. Zhu, J. Wang, W. Shen, *Appl. Catal., B* **2006**, *62*, 265-273.

54. J. Quiroz, J.-M. Giraudon, A. Gervasini, C. Dujardin, C. Lancelot, M. Trentesaux, J.-F. Lamonier, J.-F. *ACS Catal.* **2015**, *5*, 2260-2269.

55. M. Roy, S. Basak, M. K. Naskar, *Phys. Chem. Chem. Phys.* **2016**, *18*, 5253-5263.

56. K. Ramesh, L. Chen, F. Chen, Y. Liu, Z. Wang, Y.-F. Han, *Catal. Today* **2008**, *131*, 477-482.

57. A. S. P. Lovón, J. J. Lovón-Quintana, G. I. Almerindo, G. P. Valenca, M. I. B. Bernardi, V. D. Araújo, T. S. Rodrigues, P. A. Robles-Dutenhefner, H. V. Fajardo, *J. Power Sources* **2012**, *216*, 281-289.

58. M. O. Mazan, J. Marrero-Jerez, A. Soldati, P. Núñez, S. A. Larrondo, *Int. J. Hydrogen Energy* **2015**, *40*, 3981-3989.

59. R. O. Fuentes, L. M. Acuña, C. A. Albornoz, A. G. Leyva, N. Sousa, F. M. Figueiredo, *RSC Adv.* **2016**, *6*, 64861-64870.

Chapter 3. Stimul-Responsive Transformation of Flexible MOFs

3.1. Fundamentals

Flexibility is a unique property of metal-organic frameworks (MOFs) that differentiates them from other rigid inorganic porous materials such as zeolites and porous silica. Flexible frameworks are not only scientifically interesting, but also applicable for real-world gas storage/delivery, separation, sensing, and catalysis. So far, a plethora of MOFs with flexible frameworks, termed as 'soft porous crystal', 'flexible MOF', 'breathing MOF', 'sponge-like MOF' or 'dynamic MOF', has emerged as a new subclass of MOFs. Flexibility is, by definition, the ability of a material to change its form easily without breaking, according to the situation. From an anatomic perspective, it can be described as a range of joint movements and change in muscle length that connects the joints to induce a bending motion. However, in the case of inorganic solids, such concept of flexing was not compatible, because most of the materials were dense and rigid. Only the vibrational mode of atoms induced trivial displacements ($0.1 \text{ Å} < d < 1 \text{ Å}$).[1-3] From the end of the 20th century, metal-organic frameworks (MOFs; also known as porous coordination polymers) have emerged as a new class of porous materials composed of metal ions or clusters linked by organic struts, so that crystalline and extended structures can be generated.[4-6] Since then, much effort has been made to achieve permanent porosity of MOFs by securing structural rigidity. In the course of intensive studies, an intriguing aspect of MOFs, namely flexibility, has been found. Many MOFs show reversible flexing of the structures under the action of external stimuli such as guest elimination/reintroduction, temperature, pressure, or light, maintaining their structural topology but with dynamic molecular displacements (movements of > 5–10 Å).[7-13] This is because the frameworks were built with relatively weak interactions (hydrogen bonds, π-π interactions, coordination bonds, etc.), which resulted in a large number of intermolecular degrees of freedom.[14] Again, from the anatomic view, secondary building units (SBUs) of the frameworks behave like human joints and organic moieties act like bones and muscles, and this allows flexibility through the collaboration of both the organic and inorganic parts.

Unlike rigid MOFs, the adsorption isotherms of flexible MOFs generally display type V or VI (S-shaped or multi-step) behaviours.[15-17] As shown in Figure 3.1, the working capacity can be significantly increased between the gas charge and discharge pressures, because the MOF exhibits abrupt gas uptake over a narrow pressure range. In this regard, flexible MOFs often display larger working capacity in the storage/delivery of gases, such as CO_2 and CH_4, than rigid MOFs.[19-21] Optimal flexibility has also been demonstrated to maximise the selective separation efficiency of similarly sized molecules, even isomers or isotopes.[22-24] Moreover, other switchable dielectric, magnetic, and optoelectronic applications can be realized, as reversible structural transformation naturally induces changes in the physicochemical properties, such as spin transition and electron transfer. Likewise, although previous studies on flexible

MOFs have shown very attractive and meaningful results, there is a mismatch between the fundamental flexible phenomena being investigated by the laboratory scientists and the practical application sought by the industry scientists/engineers.[3] Further exploration of the structural dynamism, even for well-known archetypal MOFs, would enable their use in more practical applications.
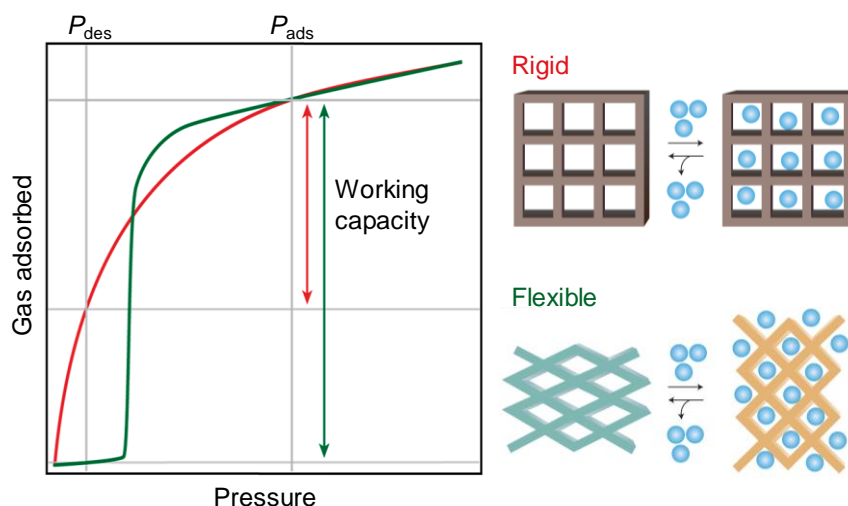

Figure 3.1. Schematic view of the adsorption profiles of rigid microporous frameworks (red line, Type I behaviour) and adsorption-induced flexible frameworks (green line, S-shaped Type V behaviour).[15,16]

Apart from the perspective of chemistry, the rigidity/flexibility of crystals has been of interest in mathematics and engineering. In general, their approaches and terminologies are somewhat unfamiliar to experimental chemists, and they are understandably out of the scope of this review. Some studies have represented MOFs on the basis of mechanical representation, however, to provide a more intuitive understanding to describe their flexibility.[23] For instance, in 2012, Goodwin et al. employed mechanical building units (MBUs) to visualise the supramolecular components and interactions of MOFs (Figure 3.2),[24] which aided in interpreting their thermo- and piezo-mechanical properties (i.e., positive/negative thermal expansion (PTE/NTE) and positive/negative linear compressibility (PLC/NLC)). Herein, three different kinds of MBUs were used to represent weak interactions, network hinges, and struts. Under variable-temperature and/or variable-pressure situations, the length and angle of each MBU would vary, thus dictating the flexibility of the framework (or mobility from the mechanical/machine viewpoint). For example, from this viewpoint, MOF-5 can be regarded as a connected array of 'strut' MBUs (Figure 3.2). Thus, one can anticipate that the vibrational modes of the struts reduce their effective length and give rise to lattice contraction with an increase in temperature (NTE effect), which was indeed observed experimentally.[25-27] Likewise, MIL-53, as a connected network of all kinds of MBUs (Figure 3.2), would display very strong anisotropic PTE/NTE and PLC/NLC behaviours, as also observed in a real system.[28-35]
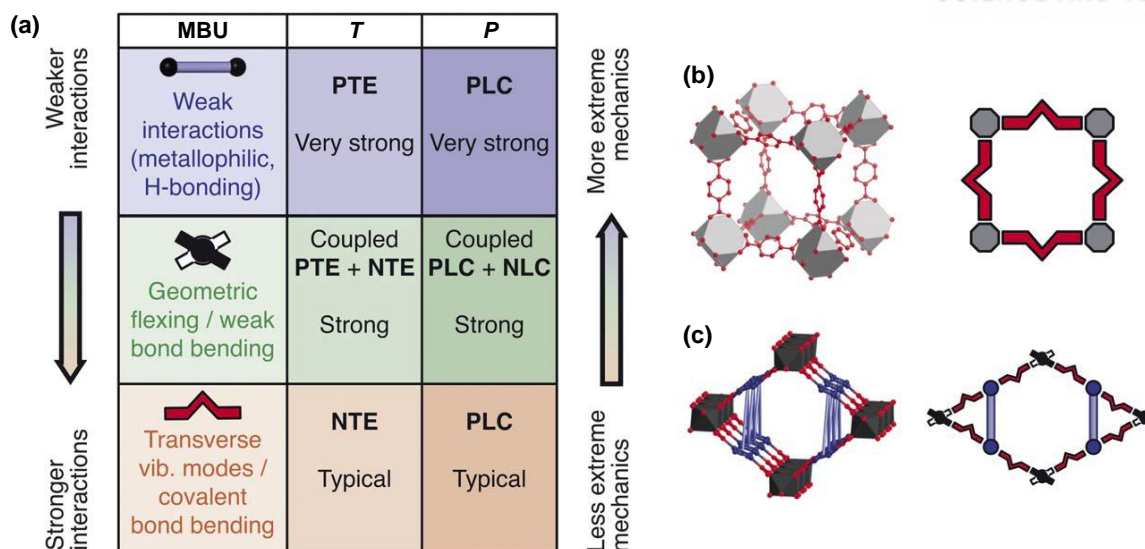
Figure 3.2. (a) Tabular summary of the thermo- and piezo-mechanical properties as a function of different classes of MBUs, based on the reported force constants. Schematic representations of (b) MOF-5 and (c) MIL-53 with their 2D MOF analogues made up of MBUs.[24]

Another mechanical representation was proposed by Smit et al. in 2014.[23] It is based on treating MOFs as a mechanical system of rigid bodies, connected by hinge joints, so that their cooperative effect governing the large-scale network flexibility can be identified (Figure 3.3). For example, a single cage of MOF-5 is reduced to a 'molecular toy' comprising red cubes and blue rods, and a 'molecular truss system' (far right of Figure 3.3). The red cube indicates the SBU and the dicarboxylate ligand the blue rod. It is noteworthy that the blue rods are oriented at 45° with respect to the face of the MOF-5 cage to reflect its potential hinge-like motion. Despite these flexible joints, the entire structure is rigid, because each hinge restricts the movement of the linkers (blue rods) to one direction while all the hinges are oriented to the faces of the cage. Overall, the degrees of freedom of the joints are mutually excluded.
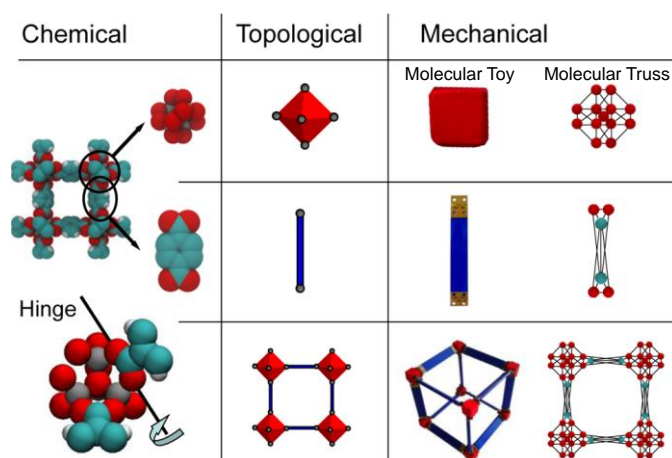

Figure 3.3. Chemical, topological, and mechanical representations of MOF-5. The far-right column represents mechanical systems of molecular trusses.[23]

The flexibility of MOFs has also been studied via computational modelling. Computational chemists have adapted versatile thermodynamic methods and models to examine what factors and mechanisms are responsible for these structural transitions upon gas sorption.[36-40] The earliest work was reported in 2009 by Miyahara et al.,[39] who conducted grand canonical Monte Carlo (GCMC) simulations and free energy analysis on an interpenetrating jungle-gym structure. The results revealed that the structural transition is guided by the stabilisation of the host upon guest adsorption, which compensates for the required energy to create adsorption sites by transforming the host framework. Moreover, in their work, hysteretic sorption behaviour, which is a characteristic of flexible MOFs, results from an energy barrier between two local minima of the structures.
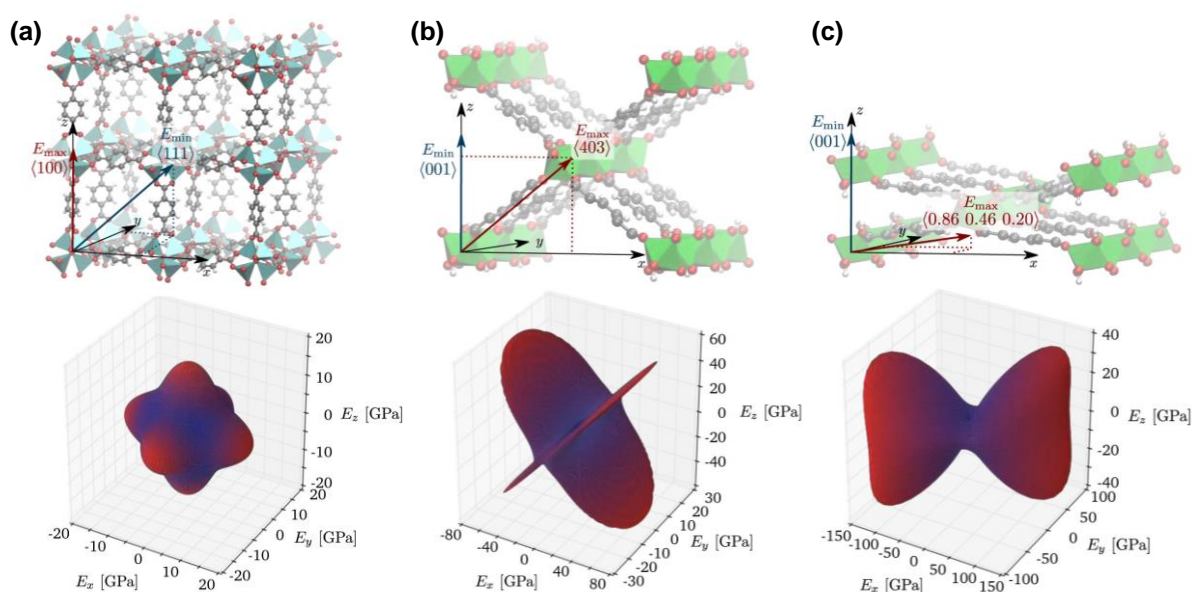

Figure 3.4. Unit cell with directions of highest and lowest Young's modulus E (left) and directional Young's modulus E at 300 K and 0 MPa represented as a 3D map (right); (a) MOF-5, (b) MIL-53-LP, and (c) MIL-53-NP.[42]

The molecular dynamic simulations are often combined with the experimental data to predict the sorption profiles and mechanical stability of flexible MOFs. For example, Coudert et al. conducted *ab initio* calculations on the elastic tensor to prove that high elastic anisotropy is the key signature of flexibility in MOFs.[37,41-43] ELATE[44] is an open-source online application that can be used to analyse and visualise elastic properties. The program uses a 6×6 symmetry matrix of elastic constants as an input to compute commonly used mechanical properties such as Bulk, Young's, and Shear moduli, and produces 3D spherical plot and its 2D projection. As shown in Figure 3.4, the Young's modulus of MIL-53 is very anisotropic depending on the direction of distortion, compared to that of MOF-5. This implies that anomalously low moduli in certain directions (i.e., high anisotropy) are required to activate flexible movement of the frameworks.

During the last decade, a number of spin-off companies from academic research groups has been found to produce MOFs that perform useful roles in markets. However, large-scale production of MOF materials that are both environmentally sustainable and economically viable is still challenging, and the commercial applications so far mostly focus on the store/release of various speciality gases and limited to niche applications. The search for a breakthrough application continues to drive research directions in MOF community. Given this industrial environment for MOF commercialization, flexible MOFs are not completely developed, yet several research papers have shown their huge potential in the fields of separation, sensing and catalysis.[3,45] However, many works are only limited to adsorption-induced gate-opening and/or breathing effects. In some cases, the enhanced performances are scarcely related to flexibility in MOFs. What makes them supreme candidates for the potential applications is the dynamic structural system that instantly responds to external stimuli.

One exemplary finding is that the flexible nature of MIL-53(Al) enabled the separation of mixtures of similar-sized and similar-shaped isotopes (H_2 and D_2) that require precise pore tuning.[46] This result reveals the following: (i) the flexible effect of MOFs helps in maximizing the separation efficiency even for very challenging gas mixtures, (ii) the mechanism and dynamics during the phase transition of flexible MOFs are still elusive, but the present findings are expected to provide new opportunities for further application of MOFs, and (iii) the existent profound studies on archetypal MOFs favours further research into exploiting their flexible properties. In this regard, we envision that a deeper understanding of the flexibility of MOFs (even the known MOFs) would allow their use in more practical and diverse applications, thereby expanding the horizons for the MOF field.

References

1. G. Férey, C. Serre, *Chem. Soc. Rev.* **2009**, *38*, 1380.
2. G. Férey, Z. Anorg. *Allg. Chem.* **2012**, *638*, 1897.
3. G. Férey, *Dalton Trans.* **2016**, *45*, 4073.
4. S. Kitagawa, R. Matsuda, *Coord. Chem. Rev.* **2007**, *251*, 2490.
5. O. M. Yaghi, H. Li, *J. Am. Chem. Soc.* **1995**, *117*, 10401.
6. H. Li, M. Eddaoudi, M. O'Keeffe, O. M. Yaghi, *Nature* **1999**, *402*, 276.
7. J. Park, D. Yuan, K. T. Pham, J.-R. Li, A. Yakovenko, H.-C. Zhou, *J. Am. Chem. Soc.* **2012**, *134*, 99.
8. T. D. Keene, D. Rankine, J. D. Evans, P. D. Southon, C. J. Kepert, J. B. Aitken, C. J. Sumby, C. J. Doonan, *Dalton Trans.* **2013**, *42*, 7871.
9. S. Henke, A. Schneemann, R. A. Fischer, *Adv. Funct. Mater.* **2013**, *23*, 5990.
10. L. D. DeVries, P. M. Barron, E. P. Hurley, C. Hu, W. Choe, *J. Am. Chem. Soc.* **2011**, *133*, 14848.
11. M. Alhamami, H. Doan, C.-H. Cheng, *Materials* **2014**, *7*, 3198.
12. Y. Yue, J. A. Rabone, H. Liu, S. M. Mahurin, M.-R. Li, H. Wang, Z. Lu, B. Chen, J. Wang, Y. Fang, S. Dai, *J. Phys. Chem. C* **2015**, *119*, 9442.
13. P. L. Llewellyn, S. Bourrelly, C. Serre, Y. Filinchuk, G. Férey, *Angew. Chem. Int. Ed.* **2006**, *45*, 7751.
14. T. D. Bennett, A. K. Cheetham, A. H. Fuchs, F.-X. Coudert, *Nat. Chem.* **2017**, *9*, 11.
15. C. J. Sumby, *Nat. Chem.* **2016**, *8*, 294.

16. C. M. McGuirk, T. Runcevski, J. Oktawiec, A. Turkie-wicz, M. K. Taylor, J. R. Long, *J. Am. Chem. Soc.* **2018**, *140*, 15924.
17. T. M. McDonald, J. A. Mason, X. Kong, E. D. Bloch, D. Gygi, A. Dani, V. Crocellà, F. Giordanino, S. O. Odoh, W. S. Drisdell, B. Vlaisavljevich, A. L. Dzubak, R. Poloni, S. K. Schnell, N. Planas, K. Lee, T. Pascal, L. F. Wan, D. Prender-gast, J. B. Neaton, B. Smit, J. B. Kortright, L. Gagliardi, S. Bordiga, J. A. Reimenr, J. R. Long, *Nature* **2015**, *519*, 303.
18. J.-R. Li, Y. Ma, M. C. McCarthy, J. Sculley, J. Yu, H.-K. Jeong, P. B. Balbuena, H.-C. Zhou, *Coord. Chem. Rev.* **2011**, *255*, 1791.
19. S. Hiraide, H. Tanaka, N. Ishikawa, M. T. Miyahara, *ACS Appl. Mater. Interfaces* **2017**, *9*, 41066.
20. M. Witman, S. Ling, S. Jawahery, P. G. Boyd, M. Haranczyk, B. Slater, B. Smit, *J. Am. Chem. Soc.* **2017**, *139*, 5547.
21. J. Y. Km, L. Zhang, R. Balderas-Xicohténcatl, J. Park, M. Hirscher, H. R. Moon, H. Oh, *J. Am. Chem. Soc.* **2017**, *139*, 17743.
22. R. El Osta, A. Carlin-Sinclair, N. Guillou, R. I. Walton, F. Vermoortele, M. Maes, D. de Vos, F. Millange, *Chem. Mater.* **2012**, *24*, 2781.
23. L. Sarkisov, R. L. Martin, M. Haranczyk, B. Smit, *J. Am. Chem. Soc.* **2014**, *136*, 2228.
24. J. M. Ogborn, I. E. Collings, S. A. Moggach, A. L. Thompson, A. L. Goodwin, *Chem. Sci.* **2012**, *3*, 3011.
25. N. Lock, Y. Wu, M. Christensen, L. J. Cameron, V. K. Peterson, A. J. Bridgeman, C. J. Kepert, B. B. Iversen, *J. Phys. Chem. C* **2010**, *114*, 16181.
26. L. H. N. Rimmer, M. T. Dove, A. L. Goodwin, D. C. Palmer, *Phys. Chem. Chem. Phys.* **2014**, *16*, 21144.
27. N. Lock, M. Christensen, Y. Wu, V. K. Peterson, M. K. Thomsen, R. O. Piltz, A. J. Ramirez-Cuesta, G. J. Mclntyre, K. Norén, R. Kutteh, C. J. Kepert, G. J. Kearley, B. B. Iversen, *Dalton Trans.* **2013**, *42*, 1996.
28. F. Millange, C. Serre, N. Guillou, G. Férey, R. I. Walton, *Angew. Chem. Int. Ed.* **2008**, *47*, 4100.
29. C. Serre, S. Bourrelly, A. Vimont, N. A. Ramsahye, G. Maurin, P. L. Llewellyn, M. Daturi, Y. Filinchuk, O. Ley-naud, P. Barnes, G. Férey, *Adv. Mater.* **2007**, *19*, 2246.
30. M.-A. Springuel-Huet, A. Nossov, Z. Adem, F. Guen-neau, C. Volkringer, T. Loiseau, G. Férey, A. Gédéon, *J. Am. Chem. Soc.* **2010**, *132*, 11599.
31. A. Boutin, F.-X. Coudert, M.-A. Springuel-Huet, A. V. Neimark, G. Férey, A. H. Fuchs, *J. Phys. Chem. C* **2010**, *114*, 22237.
32. C. Triguero, F.-X. Coudert, A. Boutin, A. H. Fuchs, A. V. Neimark, *J. Chem. Phys.* **2012**, *137*, 184702.
33. J. P. S. Mowat, V. R. Seymour, J. M. Griffin, S. P. Thompson, A. M. Z. Slawin, D. Fairen-Jimenez, T. Düren, S. E. Ashbrook, P. A. Wright, *Dalton Trans.* **2012**, *41*, 3937.
34. L. Chen, J. P. S. Mowat, D. Fairen-Jimenez, C. A. Mor-rison, S. P. Thompson, P. A. Wright, T. Düren, *J. Am. Chem. Soc.* **2013**, *135*, 15763.
35. J. Wieme, K. Lejaeghere, G. Kresse, V. V. Speybroeck, *Nat. Commun.* **2018**, *9*, 4899.
36. F.-X. Coudert, A. Boutin, M. Jeffroy, C. Mellot-Draznieks, A. H. Fuchs, *ChemPhysChem* **2011**, *12*, 247.
37. T. D. Bennett, A. H. Fuchs, A. K. Cheetham, F.-X. Coudert, *Dalton Trans.* **2016**, *45*, 4058.
38. C. M. Simon, E. Braun, C. Carraro, B. Smit, *Proc. Natl. Acad. Sci.* **2017**, *114*, E287.
39. S. Watanabe, H. Sugiyama, H. Adachi, H. Tanaka, M. T. Miyahara, *J. Chem. Phys.* **2009**, *130*, 164707.
40. R. Numaguchi, H. Tanaka, S. Watanabe, M. T. Mi-yahara, *J. Chem. Phys.* **2013**, *138*, 054708.
41. A. U. Ortiz, A. Boutin, A. H. Fuchs, F.-X. Coudert, *Phys. Rev. Lett.* **2012**, *109*, 195502.
42. S. M. J. Rogge, M. Waroquier, V. Van Speybroeck, *Acc. Chem. Res.* **2018**, *51*, 138.
43. A. U. Ortiz, A. Boutin, A. H. Fuchs, F.-X. Coudert, *J. Chem. Phys.* **2013**, *138*, 174703.
44. R. Gaillac, P. Pullumbi, F.-X. Coudert, *J. Phys.: Condens. Matter* **2016**, *28*, 275201.
45. A. Schneemann, V. Bon, I. Schwedler, I. Senkovska, S. Kaskel, R. A. Fischer, *Chem. Soc. Rev.* **2014**, *43*, 6062.
46. J. Y. Kim, L. Zhang, R. Balderas-Xicohténcatl, J. Park, M. Hircher, H. R. Moon, H. Oh, *J. Am. Chem. Soc.* **2017**, *139*, 17743.

3.2. Direct detection of explosive nitroaromatic compounds in a luminescent Li-based MOF

Introduction

Luminescent MOFs can be applied in the detection of hazardous substances, which is a very important aspect in terms of environmental and safety considerations. Several MOFs showed selective and fast detection of toxic aromatic compounds via a fluorescence quenching mechanism.[1-11] For example, a highly luminescent MOF, [$Zn_2(oba)_2(bpy)$] (H_2oba = 4,4'-oxybis (benzoic acid); bpy = 4,4'-bipyridine) was found to exhibit unique selectivity for the detection of high explosives and other aromatics via a fluorescence quenching and enhancement mechanism.[3-5] In that report, the explanation of the quenching/enhancement mechanism relied on molecular orbital and electronic band-structure calculations. Herein, we report the synthesis of a well-defined ditopic organic ligand, H_2CPMA, for the potential provision of luminescence properties in MOFs, and the successful preparation of the luminescent 3-dimensional Li-based MOF, {$Li_3[Li(DMF)_2](CPMA)_2$}·$4DMF$·$1H_2O$ (**1**) (DMF = N,N'-dimethyl formamide; H_2CPMA = bis(4-carboxyphenyl)-N-methylamine), by using the tailored H_2CPMA ligand and a lithium cation. The luminescent MOF was examined as a detector of the toxic and explosive aromatic compounds containing nitro groups as an explosophore by changing its visible color as well as showing luminescence quenching in the solid state. Significantly, we provide direct evidence for the alteration of the electronic structure of **1** upon a representative nitroaromatic compound, nitrobenzene sensing by the single-crystal-to-single-crystal transformation. The single crystal X-ray diffraction results for **1**⊃nitrobenzene clearly showed strong π-π interactions between nitrobenzene and the benzene rings of $CPMA^{2-}$ in **1**, and the inducement of CH···π interactions between neighboring $CPMA^{2-}$ ligands in the framework.

Experimental section

All chemicals and solvents used in the syntheses were of reagent grade and they were used without further purification. FT-NMR spectra were measured by a Varian 600 MHz. Infrared spectra were recorded with a ThermoFisher ScientificNicolet 6700 FT-IR spectrophotometer. Elemental analyses were performed at the UNIST Central Research Facilities Center (UCRF) in Ulsan National Institute of Science and Technology (UNIST). UV/Vis spectra were recorded with a Cary 5000 UV/vis spectrophotometer. Fluorescence spectra were measured with a Cary Eclipse fluorescence spectrometer. TGA were performed under $N_2(g)$ atmosphere at a scan rate of 5 °C/min using Q50 from TA instruments. X-ray photoelectron spectroscopy was performed using a Thermo Scientific K-Alpha XPS spectrometer. **Synthesis of H_2CPMA.** H_2CPMA (bis(4-carboxyphenyl)-N-methylamine) was prepared by modifying the methods reported in the previous study.[15] N-methyldiphenylamine (6 mL, 33.6 mmol) was dissolved

in chloroform (100 mL), to which a chloroform solution (70 mL) of Br_2 (1.8 mL, 34.9 mmol) was slowly added at 0 ℃. After stirring at 0 ℃ for 3 h, the solution was evaporated under reduced pressure, which resulted in a pale yellowish oily residue. MeOH was added to the residue until white microcrystals of bis(4-bromophenyl)-*N*-methylamine were formed. The product was filtered, washed with MeOH, and dried briefly in air. Yield: 3.9 g (35%). ^{1}H-NMR (DMSO-d_6): δ 7.43 (d, 4H), 6.97 (d, 4H), 3.22 (s, 3H). Bis(4-bromophenyl)-*N*-methylamine (1.0 g, 2.9 mmol) was dissolved in freshly distilled tetrahydrofuran (40 mL) in Ar(g) atmosphere, and *n*-butyllithium (1.6 M hexane) (12 mL, 19 mmol) was added to the solution at –78 ℃. After stirring the solution for 3 h, crushed dry ice was added, which immediately formed white precipitates. The white precipitate suspended in the solution was kept at room temperature for 4 h, and acetic acid was added to the solution until the precipitate was completely dissolved. After filtering the solution, the filtrate was concentrated and added to cold water. The resulting precipitate was filtered, washed with water, and dried under reduced pressure at ambient temperature. Yield: 0.62 g (79%). ^{1}H-NMR (DMSO-d_6): δ 7.86 (d, 4H), 7.15 (d, 4H), 3.31 (s, 3H). FT-IR (KBr pellet): $\nu_{O\text{-}C=O}$, 1673(s), 1593(s) cm^{-1}.

Synthesis of {Li$_3$[Li(DMF)$_2$](CPMA)$_2$}·4DMF·1H$_2$O (1). H$_2$CPMA (0.040 g, 1.5×10^{-1} mmol) was dissolved in DMF (2 mL) and added to the DMF solution (3 mL) of LiNO$_3$•6H$_2$O (0.021 g, 3.0×10^{-1} mmol). The mixture was placed in a Teflon vessel within the autoclave, and heated and kept at 150 ℃ for 12 h. The temperature was sequentially raised to 180 ℃ and kept for another 24 h. The solution was cooled to room temperature and kept until resulting in pale-yellow rod-like crystals. The crystals were filtered off, and washed briefly with DMF. Yield: 22%. FT-IR for **1** (Nujol mull): $\nu_{C=O(DMF)}$, 1678; $\nu_{O\text{-}C=O(carboxylate)}$, 1595; $\nu_{C=C(aromatic)}$, 1557 cm^{-1}. UV/Vis (Diffuse reflectance, λ_{max}) 339, 283 nm. Anal.Calcd for Li$_4$C$_{48}$H$_{66}$O$_{15}$N$_8$: C, 56.36; H, 6.50; N, 10.95. Found: C, 56.50; H, 6.08; N, 11.11.

Detection of nitrobenzene in 1. {Li$_3$[Li(H$_2$O)$_2$](CPMA)$_2$}·3nitrobenzene·2DMF (**1**⊃nitrobenzene): Freshly prepared pale-yellow crystals of **1** (0.032 g, 3.13×10^{-2} mmol) were immersed in nitrobenzene for 8 days. The color of **1** was dramatically changed to intensive red in 16 h, and the red crystals were filtered off, and washed briefly with DMF. The resultant solid, **1**⊃nitrobenzene was characterized by IR, UV/vis, and fluorescence spectroscopy, EA, and XPS. FT-IR for **1**⊃nitrobenzene (Nujol mull): $\nu_{C=O(DMF)}$, 1674; $\nu_{O\text{-}C=O(carboxylate)}$, 1595; $\nu_{C=C(aromatic)}$, 1557 cm^{-1}; $\nu_{O\text{-}C=O(carboxylate)}$, ν_{NO2}, 1532, 1347; $\nu_{C\text{-}N}$, 852 cm^{-1}. Anal.Calcd for Li$_4$C$_{54}$H$_{55}$O$_{18}$N$_7$: C, 58.02; H, 4.96; N, 8.77. Found: C, 59.01; H, 4.59; N, 8.70. Upon soaking **1** in nitrobenzene, two coordinated DMF molecules to Li4 are exchanged by two water molecules, which is evidenced by single-crystal X-ray diffraction. One nitrobenzene molecule and two coordinating water molecules are crystallographically detected, and the other guest molecules in {Li$_3$[Li(H$_2$O)$_2$](CPMA)$_2$}·3nitrobenzene·2DMF are completed by elemental analysis, FT-IR, and TGA.

X-ray Powder Diffraction Analysis. Powders of compounds **1** and **1**⊃nitrobenzene were packed in the 0.4 mm diameter capillary (wall thickness, 0.01 mm), respectively. Those diffraction data were

collected at 95 K with the 200 mm of detector distance in 600 sec exposure with synchrotron radiation ($\lambda = 0.79984$ Å) on an ADSC Quantum-210 detector at 2D SMC with a silicon (111) double crystal monochromator (DCM) at the Pohang Accelerator Laboratory, Korea. The ADX program[16] was used for data collection, and Fit2D program[17] was used for converting a 2-dimensional diffraction image to a 1-dimensional diffraction pattern.

Single-Crystal X-ray crystallography. Single-crystals of **1** and **1**⊃nitrobenzene coated with paratone-N oil were mounted on the loop and those diffraction data were collected at 95 K with synchrotron radiation ($\lambda = 0.74999$ Å) on a ADSC Quantum-210 detector at 2D SMC with a silicon (111) double crystal monochromator (DCM) at the Pohang Accelerator Laboratory, Korea. The ADSC Q210 ADX program[16] was used for data collection, and HKL2000 (Ver. 699.18) for **1** and HKL3000 (Ver. 703r)[18] for **1**⊃nitrobenzene were used for cell refinement, reduction and absorption correction, respectively.

The crystal structure of **1** was solved by the direct space method with SIR2011 program[19] and refined by full-matrix least-squares calculations with the SHELX-TL (Ver. 2008) program package.[20] Two ligands, four lithium ions, and two coordinated DMF molecules were observed as an asymmetric unit. Thermal factors of nitrogen (N1A) and carbon (C1A) atoms in a coordinated DMF molecule were restrained by using SIMU, DELU, and ISOR during the least-squares refinement. The crystal structure of **1**⊃nitrobenzene was solved by the direct method with SHELXTL-XS program[20] and refined by full-matrix least-squares calculations with the SHELX-TL (Ver. 2008) program package.[20] Two ligands, four lithium ions, two coordinated waters, and one nitrobenzene molecule as a guest were observed as an asymmetric unit. After soaking **1** in nitrobenzene, its single crystallinity was decreased to result in inferior quality of data to **1**. The nitro group in a nitrobenzene molecule was restrained by using DFIX, DANG, SIMU and DELU during the least-squares refinement. For both structures, all non-hydrogen atoms were refined anisotropically. The hydrogen atoms were assigned isotropic displacement coefficients U(H) = 1.2U (C,N) or 1.5U(C$_{methyl}$), and their coordinates were allowed to ride on their respective atoms. All the methyl hydrogen atoms and some hydrogen atoms on the carbon atoms are not included during the least-squares refinement. Even though electron densities of some guest solvent molecules were found, those could not be well modeled in the refinement due to the severe disorder. The final refinement was performed with the modification of the structure factors for the contribution of the disordered solvent electron densities using the SQUEEZE option of PLATON.[21] Further crystallographic details for the structure reported in this paper can be obtained from the Cambridge Crystallographic Data Center, on quoting the depository numbers CCDC 874240 for **1**, and 874241 for **1**⊃nitrobenzene.

Results and discussion

To construct a luminescent MOF, we designed an organic building block which can induce intraligand charge transfer (ILCT) through the coexistence of electron donor and acceptor groups in a molecule. Since the charges in bis(4-carboxyphenyl)-*N*-methylamine (H$_2$CPMA) can be transferred from the *N*-methylamino donor group to an acceptor carboxylate group, H$_2$CPMA is a good candidate ligand for the construction of luminescent MOFs (Figure 3.5). H$_2$CPMA was successfully prepared *via* the halogen-lithium exchange reaction of bis(4-bromophenyl)-*N*-methylamine and subsequent carbonation of the resultant dilithio compound (Figure 3.6, synthetic details in Experimental section). The solvothermal reaction of Li(NO$_3$)·6H$_2$O with H$_2$CPMA in DMF as the solvent yielded pale yellow crystals of {Li$_3$[Li(DMF)$_2$](CPMA)$_2$}·4DMF·1H$_2$O (**1**). The structure of **1**, which was determined by single-crystal X-ray diffraction,[12] consisted of Li-O chains as the SBUs and bridging ligands (Figure 3.7a). Compound **1** possesses four crystallographically independent lithium atoms in distorted tetrahedral coordination geometry.
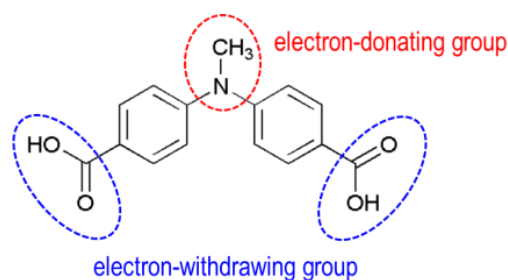
Figure 3.5. Schematic structure of organic ligand H$_2$CPMA.
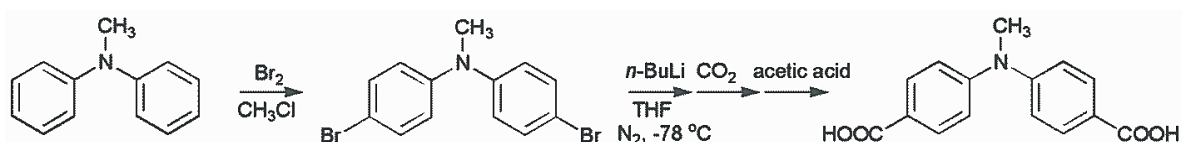
Figure 3.6. Preparation of bis(4-carboxyphenyl)-*N*-methylamine (H$_2$CPMA).

As shown in Figure 3.7a, Li1, Li2, and Li3 are bonded by four carboxylate oxygen atoms, associated with four different CPMA^{2-} moieties (bond lengths of Li-O; 1.910 – 2.016 Å). Li4 also has a tetrahedral geometry, and is coordinated with two oxygen atoms from two different carboxylate groups (Li-O, av. 1.994(5) Å) and two carbonyl oxygen atoms of DMF (Li-O, av. 1.911(6) Å). The tetrahedrally coordinated lithium ions generate 1D Li-O chains as SBUs, which are bridged with four neighboring chains by dicarboxylate ligands, CPMA^{2-}, in four different directions (Figure 3.7b). As a result, a 3-dimensional {Li$_3$[Li(DMF)$_2$](CPMA)$_2$}$_n$ network is constructed with two kinds of rectangular channels, A and B, along *c*-axis. Channel A, of 13.4 x 10.4 Å, is occupied by free guest molecules, DMF and water, and channel B of 12.3 x 9.5 Å^2 is filled with Li4-coordinating DMF molecules. In Figure 3.9a and b, the XRPD pattern of the as-synthesized **1** is compared with the simulated pattern based on the

X-ray single crystal diffraction data, and the good agreement reveals that the as-synthesized product is a pure-phase material.
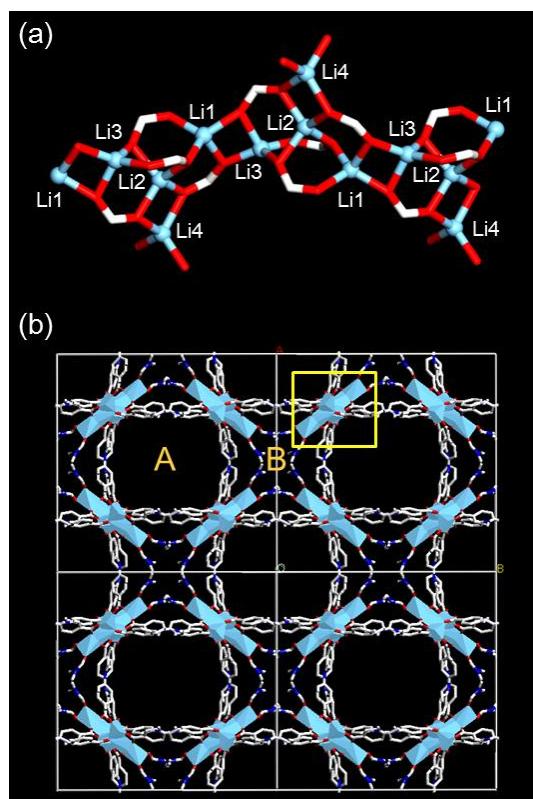

Figure 3.7. Single-crystal X-ray structure of **1**. (a) SBU of Li-O chain. (b) 3D framework formed by association of SBUs and organic ligands, projected along the *c*-axis. Hydrogen atoms and non-coordinating guest molecules are omitted for clarity. (Color scheme: C, white; O, red; N, blue; and Li, light blue) The yellow rectangle indicates the SBU of the Li-O chain.

Figure 3.8. An ORTEP drawing with an atomic numbering scheme (thermal ellipsoids at 30% probability). Hydrogen atoms are omitted for clarity. The hydrogen atoms of coordinated water molecules were not located. Symmetry operations: #1, x-1/2, -y+1/2, z; #2, -x+3/2, y+1/2, z; #3, -x+3/2, -y+1/2, z-1/2; #4, -x+2, y, z-1/2; #5, x, -y, z-1/2.

Figure 3.9. Synchrotron X-ray powder diffraction data (λ = 0.79984 Å) measured at 95 K for (a) as-synthesized **1** and (c) **1**⊃nitrobenzene, and simulated patterns from X-ray single-crystal data of (b) as-synthesized **1** and (d) **1**⊃nitrobenzene, respectively.

Figure 3.10. TGA trace of $\{Li_3[Li(DMF)_2](CPMA)_2\}\cdot 4DMF\cdot 1H_2O$ (**1**).

In the TGA trace of as-synthesized **1** (Figure 3.10), the guest solvent molecules occupied in channel A of **1** can be removed in the range from room temperature to *ca.* 160 $^{\circ}C$ with experimentally determined weight loss of 31.2%, which shows good agreement with the calculated one of 30.3%. To remove coordinating DMF molecules from Li4, temperature should reach around 450 $^{\circ}C$, followed by decomposition of **1**. PLATON calculations indicate that **1** contains 40.3% void space (4276.5 $Å^3$ per unit cell volume) for accessing the guest molecules per unit cell. Gas sorption isotherm for dried Li-MOF **1** showed no porosity as shown in N_2 sorption isotherm (Figure 3.12), because Li-MOF **1** showed the flexible behavior according to existence of guest molecules as evidenced by XRPD in Figure 3.11. Disappearance of (200) peak at the range of low angles exhibits the collapse of channels in Li-MOF, resulting in the different structure from the as-synthesized.
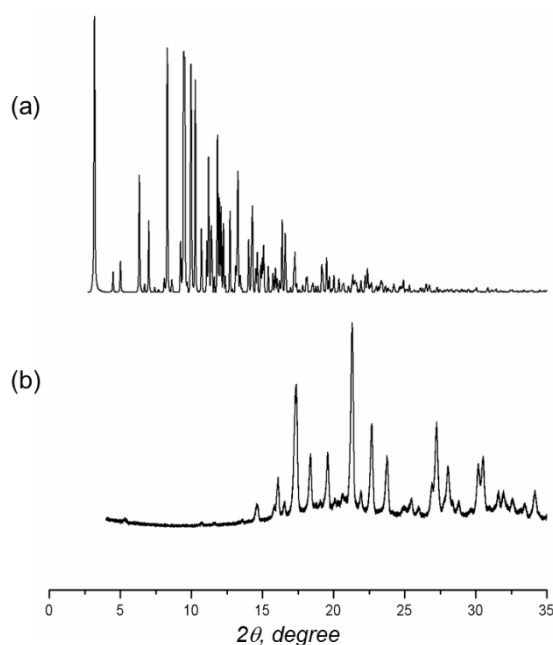
Figure 3.11. Comparison of X-ray powder diffraction data for (a) as-synthesized **1**, and (b) dried MOF.
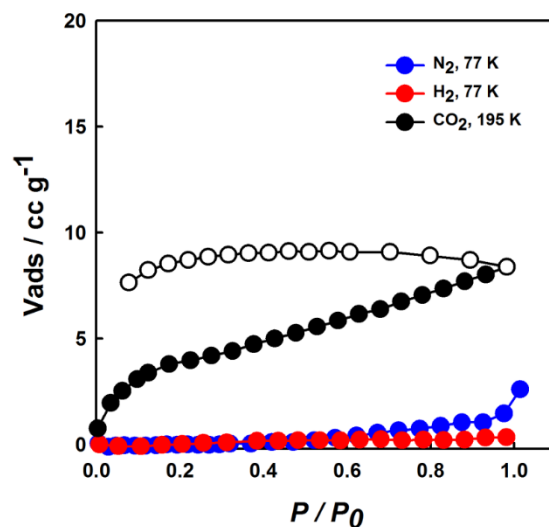
Figure 3.12. Gas sorption isotherms of Li-MOF **1**.

To see the specific analytes detection ability of **1**, compound **1** is soaked in nitrobenzene, 2,4-dinitrotoluene (DNT), benzene, and toluene. Because DNT is a solid phase at room temperature, **1** is immersed in concentrated DMF solution of DNT, and other solvents are used as neat. When Li-MOF **1** is immersed in nitrobenzene and 2,4-dinitrotoluene (DNT), it shows a dramatic color changes from pale yellow to red and deep orange, respectively. In contrast, **1** remains original color upon soaking in benzene and toluene (Figure 3.14). Thus, **1** has ability to detect nitroaromatic compounds selectively, and **1** containing nitrobenzene molecules is scrutinized to understand the sensing mechanism. Li-MOF **1** absorbs three nitrobenzene molecules per formula unit, yielding $\{Li_3[Li(H_2O)_2](CPMA)_2\}\cdot 3nitrobenzene\cdot 2DMF$ (**1**⊃nitrobenzene), as evdenced by elemental analysis. In Figure 3.13, comparison of the IR spectra of **1** and **1**⊃nitrobenzene exhibits that **1**⊃nitrobenzene clearly shows asymmetric NO_2 stretch (1532 cm^{-1}), symmetric NO_2 stretch (1347 cm^{-1}), and C-N stretch for Ar-NO_2 (852 cm^{-1}). The XPS results also clearly show the inclusion of nitrobenzene in **1** (Figure 3.15). The UV-vis absorption spectrum of **1** in the solid state (Figure 3.16) shows two absorption peaks, at 248 and 352 nm, which means there is no significant color in the visible region. However, when the as-synthesized **1** absorbs nitrobenzene, the obtained **1**⊃nitrobenzene exhibits deep-red color (Figure 3.17a); this is proved spectroscopically by the appearance of an additional absorption peak at around 500 nm (Figure 3.16). The intense red color of **1**⊃nitrobenzene is attributed to the charge-transfer transition between the aromatic rings of the electron-rich CPMA^{2-} molecules and the electron-deficient nitrobenzene due to the strong electron-withdrawing –NO_2 group. **1** is reversibly regenerated in 5 min simply by heating the nitrobenzene-absorbed **1** at 100 ℃ under vacuum, as is readily observed by the color change. Such visualization of the uptake of harmful molecules in the solid state provides great opportunities for utilizing this MOF as a sensor.
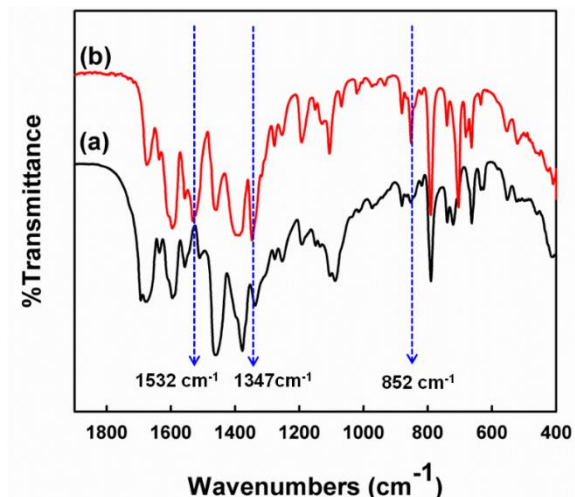
Figure 3.13. Transmission FT-IR spectra of (a) **1** (black) and (b) **1**⊃nitrobenzene (red).
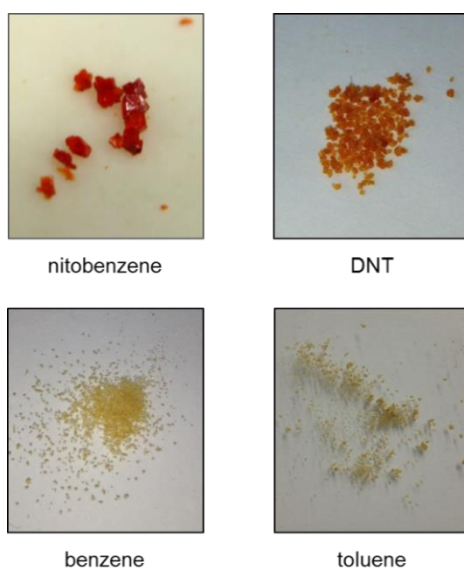

Figure 3.14. Photographs of **1** after immersing in neat nitrobenzene, benzene, toluene, and 2,4-dinitrotoluene (DNT)/DMF solution, respectively.
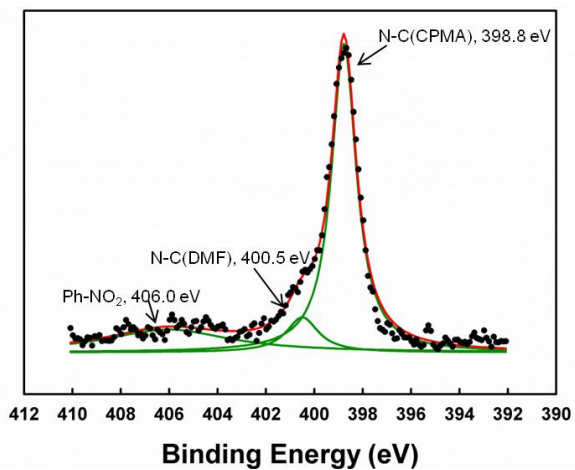

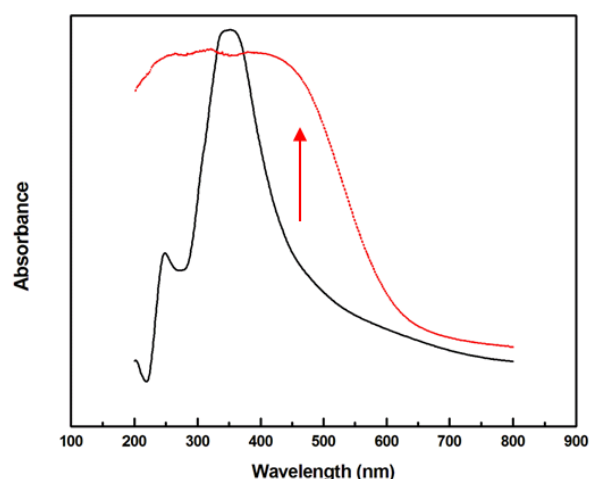**Figure 3.15.** N 1s XPS result of **1**⊃nitrobenzene.

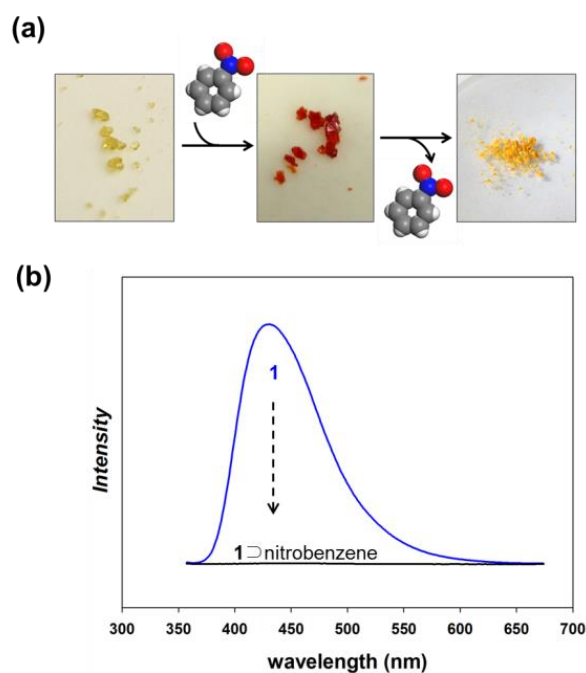**Figure 3.16.** UV-visible spectra of **1** (black) and **1**⊃nitrobenzene (red) in the solid state.

Figure 3.17. Detection of nitrobenzene in **1**. (a) Photographs of **1**, **1**⊃nitrobenzene, and **1** regenerated by heating. (b) Fluorescence spectra of **1** and **1**⊃nitrobenzene.

The other approach for sensing nitroaromatic explosives is fluorescence quenching on detection. As our aim was to generate fluorophores in a MOF by using a tailored organic ligand as a building block, the emission spectrum of **1** was recorded in the solid state. The MOF **1** exhibits an intense emission at λ_{max} = 430 nm when it is excited at 345 nm. The emission in **1** is derived from a strong intraligand charge transfer (ILCT) from the donor *N*-methylamino group to the acceptor carboxylate groups in the CPMA^{2-} molecule. On the contrary, **1**⊃nitrobenzene is completely non-emissive under excitation at 345 nm (Figure 3.17b). The same response occurs in **1**⊃DNT as shown in Figure 3.18. This

fluorescence-quenching phenomenon can be explained by an electron-transfer donor-acceptor mechanism via host-guest interactions.[9,14] To see the detection behavior of **1** upon the concentration of explosive materials, the fluorescence spectra for MOF **1** after immersion in various concentration solutions of nitrobenzene/DMF were obtained (Figure 3.19). As increasing the concentration of nitrobenzene in DMF (2.4×10^{-2} M ~ neat nitrobenzene), the maximum intensity of fluorescence spectrum was decreased. To clearly show the relative intensities, percentage of fluorescence was plotted in Figure 3.19b, which was estimated using formula (I_a/I_0) x 100%, where I_0 is the maximum intensity of Li-MOF **1**, and I_a is the maximum intensity of Li-MOF **1** after immersion in a M nitrobenzene/DMF solution. From the fitting curve of it, the concentration for half-quenching of fluorescence is calculated to 0.048 M of nitrobenzene/DMF solution.
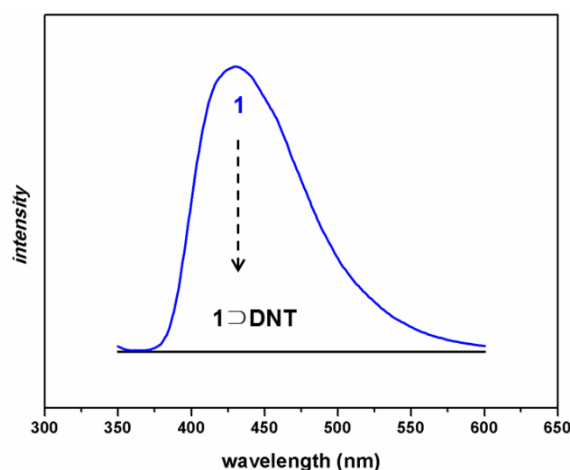

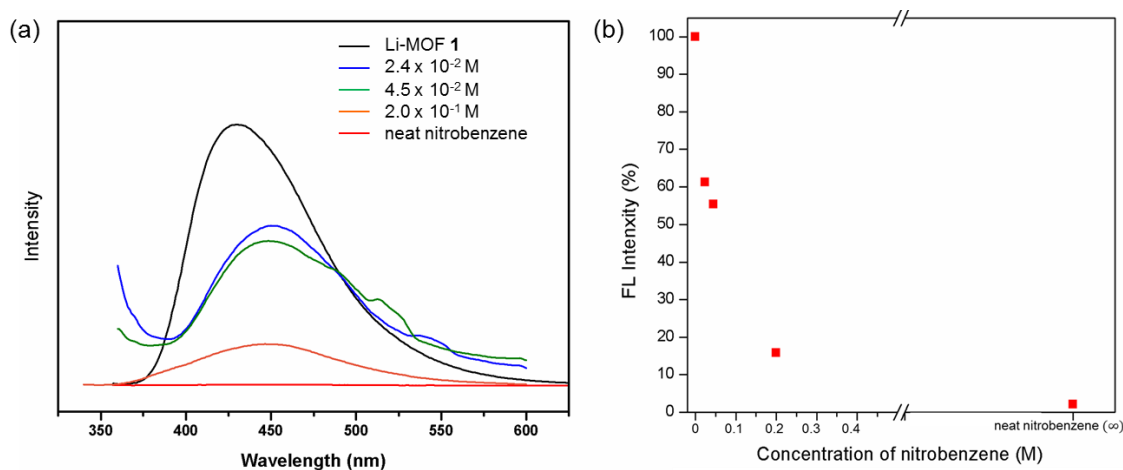**Figure 3.18.** Fluorescence spectra of **1** and **1**⊃DNT.

Figure 3.19. (a) Nitrobenzene concentration-dependent fluorescence spectra of Li-MOF **1**. (b) Percentage of fluorescence at the λ_{max}, estimated using formula (I_a/I_0) x 100%, where I_0 is the maximum intensity of Li-MOF **1**, and I_a is the maximum intensity of Li-MOF **1** after immersion in a M nitrobenzene/DMF solution.
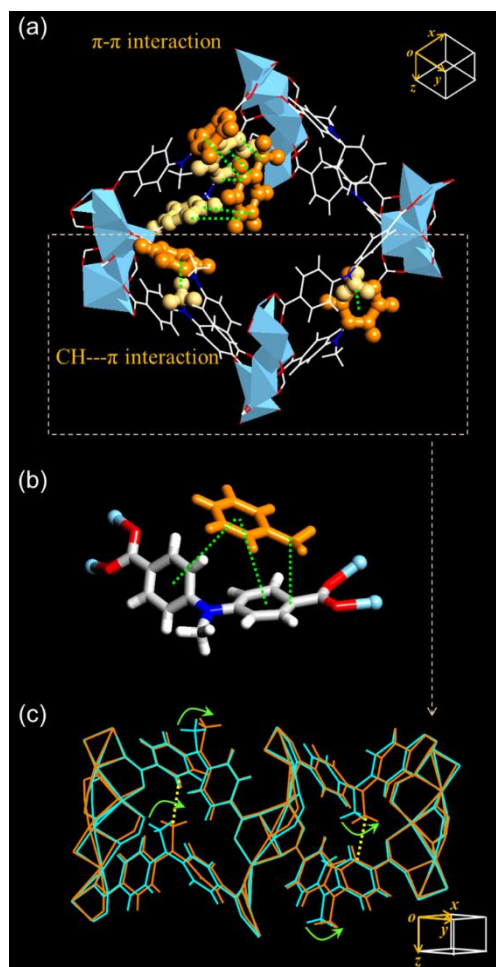
Figure 3.20. (a) X-ray structure of **1** ⊃ nitrobenzene, in which π-π and C-H⋯π interactions are emphasized by the orange ball-and-stick representation (color scheme: C, white; O, red; N, blue; and Li, light blue). (b) Close-up shot of interaction between nitrobenzene (orange) and CPMA^{2-} incorporated in **1**. (c) Comparison of the superimposed X-ray structures of **1** (cyan), and **1** ⊃ nitrobenzene (orange).

When **1** is immersed in nitrobenzene, the molecules are easily included as guests in the channels of **1**, for which the driving forces are these effective interactions of nitrobenzene with the inner surface of **1**. As shown in Figure 3.17a, even after the absorption of nitrobenzene, **1** preserves its single-crystalline nature. Therefore, the host-guest interaction in **1** ⊃ nitrobenzene is observed directly by single-crystal X-ray diffraction,[13] and this accounts for the luminescence quenching as well as the crystal color change. In Figure 3.9c and d, XRPD pattern of the **1** ⊃ nitrobenzene is coincident with the simulated pattern based on the X-ray single crystal diffraction data, showing the homogeneous uptakes of nitrobenzene in **1**. The X-ray structures of **1** and **1** ⊃ nitrobenzene are compared clearly in Figure 3.20. The confined nitrobenzene molecules in the channels of **1** lead to strong π-π stacking with three benzene rings belonging to two neighboring CPMA^{2-} units in the framework (shortest C⋯C distances: 3.455, 3.550, and 3.849 Å, respectively) (Figure 3.20a). Furthermore, strong interaction between the nitro group and

the benzene ring of a CPMA^{2-} ligand is revealed by a short distance of $N_{nitro}\cdots C_{CPMA2-}$ as 3.091 Å. The close-up shot of interaction between nitrobenzene and one of CPMA^{2-} incorporated in **1** is shown in Figure 3.20b. In this range of interactions, the electron-deficient nitrobenzene can act as an electron acceptor for the photoexcited electrons of **1**, resulting in electron-transfer from the MOF to the nitrobenzene, followed by back electron transfer instead of fluorescence. Moreover, as shown in the superimposed X-ray structures of **1** and **1**⊃nitrobenzene (Figure 3.20c), the π-π interactions cause the molecular dynamics of the flexible ligand CPMA^{2-}; meanwhile, the methyl group of CPMA^{2-} approaches the neighboring benzene ring of CPMA^{2-} to induce C-H$\cdots$π interactions in the framework. The $C_{methyl}\cdots$centroid distances decrease from 4.359 to 4.050 Å after nitrobenzene inclusion. This interligand interaction also contributes to the change in the electronic structure of **1**, quenching the fluorescence.

Conclusion

In conclusion, we introduced a well-defined ditopic organic ligand, H$_2$CPMA, for the potential provision of luminescence properties in MOFs, and the successful preparation of the luminescent 3-dimensional Li-based MOF. A luminescent Li-based MOF detected explosive nitroaromatic compounds selectively by showing an intensive color change as well as luminescence quenching in the solid state. We provided the direct evidence for the sensing mechanism of the MOF toward the nitroaromatic compound via single-crystal X-ray diffraction of MOF containing nitroaromatic compounds. Strong interaction between the MOF and included compounds explained the alteration of the electronic structure of the MOF. This result will afford in-depth understanding to help design MOFs as a sensor, in which the specific sites to interact with analytes are introduced.

References

1. S. S. Kaye, A. Dailly, O. M. Yaghi, J. R. Long, *J. Am. Chem. Soc.* **2007**, *129*, 14176-14177.
2. Y.-G. Lee, H. R. Moon, Y. E. Cheon, M. P. Suh, M. P. *Angew. Chem., Int. Ed.* **2009**, *47*, 7741-7745.
3. A. Corma, H. Garcia, F. X. Llabrés i Xamena, *Chem. Rev.* **2010**, *110*, 4606-4655.
4. T. Ishida, M. Nagaoka, T. Akita, M. Haruta, *Chem. Eur. J.* **2008**, *14*, 8456-8460.
5. M. S. El-Shall, V. Abdelsayed, A. E. R. S. Khder, H. M. A. Hassan, H. M. El-Kaderi and T. E. Reich, *J. Mater. Chem.* **2009**, *19*, 7625-7631.
6. S. Bureekaew, H. Sato, R. Matsuda, Y. Kubota, R. Hirose, J. Kim, K. Kato, M. Takata, S. Kitagawa, *Angew. Chem. Int. Ed.* **2010**, *49*, 7660-7664.
7. S. Henke, R. A. Fischer, *J. Am. Chem. Soc.* **2011**, *133*, 2064-2067.
8. A. J. Lan, K. H. Li, H. H. Wu, D. H. Olson, T. J. Emge, W. Ki, M. Hong, J. Li, *Angew. Chem. Int. Ed.* **2009**, *48*, 2334-2338.
9. S. Pramanik, C. Zheng, X. Zhang, T. J. Emge, J. Li, *J. Am. Chem. Soc.* **2011**, *133*, 4153-4155.

10. H. Xu, F. Liu, Y. Cui, B. Chen, G. Qian, *Chem. Commun.* **2011**, *47*, 3153-3155.
11. Z. Zhang, S. Xiang, X. Rao, Q. Zheng, F. R. Fronczek, G. Qian, B. Chen, *Chem. Commun.* **2010**, *46*, 7205-7207.
12. Crystal data for **1** (Li$_4$C$_{36}$H$_{36}$N$_4$O$_{10}$), M_r = 712.45, *Orthorhombic*, space group *Iba*2 (no. 45), a = 28.467(6), b = 28.594(6), c = 12.960(3) Å, α = 90°, V = 10549(4) Å^3, Z = 8, d_{calcd} = 0.897 g cm^{-3}, T = 95(2) K, crystal size 0.3 x 0.3 x 0.1 mm^3, λ = 0.74999 Å, 2θ = 60.00, 491 parameters, R_1 = 0.0862 ($I > 2\sigma(I)$, 13000 reflections), wR_2 = 0.2489 (all data, 44991 reflections), GOF = 1.070. Further crystallographic details for the structure can be obtained from the Cambridge Crystallographic Data Center, on quoting the depository number CCDC 874240.
13. Crystal data for **1**⊃nitrobenzene (Li$_4$C$_{36}$H$_{31}$N$_3$O$_{12}$), M_r = 725.40, *Orthorhombic*, space group *Iba*2 (no. 45), a = 28.710(6), b = 28.737(6), c = 12.883(3) Å, α = 90°, V = 10629(4) Å^3, Z = 8, d_{calcd} = 0.907 g cm^{-3}, T = 95(2) K, crystal size 0.1 x 0.1 x 0.05 mm^3, λ = 0.90000 Å, 2θ = 60.00, 466 parameters, R_1 = 0.1906 ($I > 2\sigma(I)$, 7225 reflections), wR_2 = 0.4817 (all data, 23112 reflections), GOF = 2.042. Further crystallographic details for the structure can be obtained from the Cambridge Crystallographic Data Center, on quoting the depository number CCDC 874241.
14. S. J. Toal, W. C. Trogler, *J. Mater. Chem.* **2006**, *16*, 2871-2883.
15. B. R. Laliberte, S. A. Leone, *J. Organometal. Chem.* **1972**, *37*, 209-215.
16. A. J. Arvai, C. Nielsen, ADSC Quantum-210 ADX Program, Area Detector System Corporation; Poway, CA, USA, **1983**.
17. Fit2D program: Andy Hammersley (E-mail: hammersley@esrf.fr), ESRF; 6 RUE JULES HOROWITZ BP 220 38043 GRENOBLE CEDEX 9 FRANCE
18. Z. Otwinowski, W. Minor, in Methods in Enzymology, ed. Carter, Jr., C. W.; Sweet, R. M. Academic Press, New York, **1997**, vol. 276, part A, pp. 307.
19. M. C. Burla, R. Caliandro, M. Camalli, B. Carrozzini, G. L. Cascarano, C. Giacovazzo, M. Mallamo, A. Mazzone, G. Polidori, R. J. Spagna, *Appl. Cryst.* **2012**, *45*, 357-361.
20. G. M. Sheldrick, SHELXTL-PLUS, Crystal Structure Analysis Package; Bruker Analytical X-Ray; Madison, WI, USA, **1997**.
21. Platon program: A. L. Spek, *ActaCrystallogr., Sect. A* **1990**, *46*, 194-201.

3.3. Solvent-induced transformation of a Zn_4O-containing doubly interpenetrated MOF

Introduction

The structural rearrangement of molecular components responding to a specific stimulus exerts an immediate effect on the chemical or physical properties of MOFs.[1-4] Thus, direct observations of structural changes in MOFs using single-crystal X-ray diffraction (SCD) facilitate the understanding of their behaviours, and aid in the design of MOFs with superior performance. Over the past decade after Fijita's and Suh's groups reported the first single-crystal to single-crystal to single-crystal (SC-SC) transformation phenomena for the coordination polymers,[5,6] numerous examples SC-SC transformations have been reported,[7-20] such as those on guest removal,[11,12] guest exchange,[13,14] temperature change, [15-17] ligand exchange,[18] and metal ion exchange[19] and addition of metal ions and anions.[20]

The guest-induced dynamic structural changes of MOFs are the important phenomena that can be applied for sensor technologies. If the transformation occurs in a SC-SC manner on guest-exchange, it can provide meaningful and direct structural information for the property change such as a pore structure, luminescence, and magnetism. The SC-SC transformation occurs only when the framework is robust yet flexible in solvent exchange. In this context, interpenetrating MOFs can serve as appropriate systems, as several interesting observations regarding the same have been reported.[21-27] For example, Kitagawa *et al.* reported an α-polonium-type doubly interpenetrated 3-D MOF,[25] which retained single crystallinity during dehydration and rehydration with a concomitant colour change; moreover, the anion exchange between $N(CN)_2^-$ and N_3^- induced slippage of the two independent networks and an increase in channel size. The same group developed the flexible doubly interpenetrated porous framework for a chemosensor by using its structural dynamics in response to the incorporation of chemically diverse analytes, which were proved by SCD studies.[26] Another interesting interpenetrating MOF showing SC-SC transformations was reported by Barbour's group.[27] As-synthesized doubly interpenetrated MOF converted to its triply interpenetrated analogue upon desolvation, as monitored by SCD, and its conversion mechanism was proposed by computational results.

In the previous section 3.2, we conducted SC-SC transformations of a Li-based MOF upon the immersion of explosive nitro compounds.[15] The results clearly revealed that the change of its fluorescence properties was originated by the newly formed host-guest interactions. This interesting behaviour was attributed to the flexible ligand, bis(4-carboxyphenyl)-*N*-methylamine (H_2CPMA), which contains electron-donating and withdrawing groups simultaneously, and also has the rotating sites on a tertiary amine and carboxylate groups (Figure 3.21a). Thus, in this study, we chose the same flexible CPMA ligand to build a new 3-D doubly interpenetrated MOF, which was expected to exhibit dynamic structural changes upon guest-exchange with organic solvents. In order to explore the type and strength of the interactions with the phenyl rings in $CPMA^{2-}$, benzene, hexane, and methanol were

selected as exchanging solvents. Due to the SC-SC transformation upon guest-exchange, the effects of host-guest interactions on the motions of the molecular components in the coordination framework were directly observed.

Experimental section

All chemicals and solvents used in the syntheses were of reagent grade and they were used without further purification. H_2CPMA (bis(4-carboxyphenyl)-*N*-methylamine) was prepared by the methods reported in the previous study.[37] Elemental analyses were performed at the UNIST Central Research Facilities Center (UCRF) in Ulsan National Institute of Science and Technology (UNIST). IR spectra were recorded with a ThermoFisher Scientific Nicolet 6700 FT-IR spectrophotometer. TGA were performed under $N_2(g)$ atmosphere at a scan rate of 5 $^{\circ}C$ min^{-1} using Q50 from TA instruments. X-ray powder diffraction data were recorded on a Bruker D2 phaser diffractometer at 30 kV and 10 mA for Cu Kα ($\lambda = 1.541$ Å), with a step size of 0.02° in 2θ.

Synthesis of [Zn$_4$O(CPMA)$_3$]·6DMF (1). H_2CPMA (0.040 g, 1.5×10^{-4} mol) was dissolved in DMF (2 mL) and added to the DMF solution (3 mL) of $Zn(NO_3)_2$•6H$_2$O (0.051 g, 1.7×10^{-4} mol). The mixture was placed in a Teflon vessel within the autoclave and heated at 110 ºC for 24 h. The solution was cooled to room temperature, which resulted in deep orange block-like crystals. The crystals were filtered and washed briefly with DMF. Yield: 0.039 g (51%). FT-IR for **1** (KBr pellet): ν_{OH}, 3406; $\nu_{CH(aromatic)}$, 3066; $\nu_{CH3(aliphatic)}$, 2930; $\nu_{C=O(DMF)}$, 1664; $\nu_{O-C=O(carboxylate)}$, 1594; $\nu_{C=C(aromatic)}$, 1553 cm^{-1}. UV/Vis (diffuse reflectance, λ_{max}) = 237, 321, 375(sh), 428(sh) nm. Anal. Calcd for $Zn_4C_{63}H_{75}O_{19}N_9$: C, 49.66; H, 4.96; N, 8.27. Found: C, 47.71; H, 4.75; N, 7.84. Data indicates that some DMF guest molecules are readily released as soon as exposure to air.

Guest-exchange Studies. Three different organic solvents, benzene, *n*-hexane, and methanol, were selected for the guest exchange of DMF molecules in **1**. Crystals of **1** (ca. 120 mg) were immersed in a neat solvent (10 mL) at room temperature for 12 h. The solvent was discarded and the crystals were reimmersed in fresh solvent (10 mL) for another 60 h to exchange all guest DMF molecules. Guest-exchanged single crystalline compounds, namely, [Zn$_4$O(CPMA)$_3$] ·3.5benzene (**1$_{benzene}$**), [Zn$_4$O(CPMA)$_3$]·3(*n*-hexane) (**1$_{hexane}$**), and [Zn$_4$O(CPMA)$_3$]·9MeOH·4H$_2$O (**1$_{MeOH}$**), were obtained. Anal. Calcd for $Zn_4C_{66}H_{54}N_3O_{13}$ (**1$_{benzene}$**): C, 58.35; H, 4.01; N, 3.09. Found: C, 59.79; H, 4.31; N, 3.24. FT-IR (KBr pellet): $\nu_{C=C(aromatic)}$, 3090(m); $\nu_{O-C=O}$, 1594(s), 1541(s) cm^{-1}. Anal. Calcd for $Zn_4C_{63}H_{75}N_3O_{13}$ (**1$_{hexane}$**): C, 56.31; H, 5.63; N, 3.13. Found: C, 57.59; H, 6.10; N, 3.51. FT-IR (KBr pellet): $\nu_{CH3(aliphatic)}$, 2924(m); $\nu_{O-C=O}$, 1594(s), 1553(s) cm^{-1}. Anal. Calcd for $Zn_4C_{54}H_{77}N_3O_{26}$ (**1$_{MeOH}$**): C, 44.86; H, 5.37; N, 2.91. Found: C, 44.18; H, 5.37; N, 2.89. FT-IR (KBr pellet): ν_{OH}, 3351(m, br); $\nu_{O-C=O}$, 1595(s), 1538(s); cm^{-1}. In order to exclude the possibility of dissociation and renucleation in the

new solvent system, following experiments were also performed. Crystal **1** was sealed in a glass capillary together with DMF. After the cell parameters of **1** were determined, the crystal was removed from the capillary. Capillaries with a size of 0.5 mm were each filled with different organic solvent, creating an empty space of 1 cm length from the bottom. Crystal **1** was dropped in the solvent layer and a photograph of the crystal was taken immediately. During the immersion of the crystal, photographs were taken to see if the size, morphology, transparency, and position of the crystal were altered. Since no change was observed, the possibility of the dissolution of **1** in the solvent followed by crystallization or renucleation at the surface as well as the growth of a new phase was excluded. The crystal was pushed from the solvent layer to the empty space by using a very thin glass fiber, and most of the solvent was removed, remaining small amount of the solvent in the capillary. The capillary was cut into an appropriate size, sealed, and mounted on Enraf Nonius Kappa CCD X-ray diffractometer to check the cell parameters for the guest exchanged crystal.

Monitoring of the guest exchange process. To trace the degree of exchange of DMF guest molecules with benzene, the sample **1** immersed in benzene was occasionally taken and digested in the D_2O with DCl for FT-NMR measurement. The integral ratios of NMR peaks corresponded to the methyl groups of DMF guest molecules and CPMA ligands in the MOF at each time were calculated to show the exchange percentage (Figure 3.28).

Single-crystal X-ray crystallography. Single-crystals of **1**, **1benzene**, **1hexane**, and **1MeOH** were coated with paratone-*N* oil, and the diffraction data were measured at 100 K with synchrotron radiation ($\lambda = 0.64999$ Å) on an ADSC Quantum-210 detector at 2D SMC with a silicon (111) double crystal monochromator (DCM) at the Pohang Accelerator Laboratory, Republic of Korea. The ADSC Q210 ADX program[38] was used for data collection, and HKL3000sm (Ver. 703r)[39] was used for cell refinement, reduction, and absorption correction. The crystal structures were solved by direct methods and refined by full-matrix least-squares calculations with the SHELX-97 computer program.[40] The positions of all non−hydrogen atoms were refined with anisotropic displacement factors. The hydrogen atoms were positioned geometrically using a riding model. In **1**, **1benzene**, and **1MeOH,** the final refinement was performed with modification of the structure factors for contribution of the disordered solvent electron densities using the SQUEEZE option of the PLATON program.[41] For **1**, no solvent molecules were refined in Zn_8 formula unit, and the electron densities of eight disordered DMF molecules were removed by SQUEEZE process. For **1benzene**, three benzene molecules were refined in Zn_{16} formula unit, and the electron densities of twenty eight disordered benzene molecules were removed by SQUEEZE process. For **1hexane**, three hexane molecules were refined in Zn_4 formula unit. For **1MeOH**, six methanol molecules and one water molecule was refined in Zn_4 formula unit, and the electron densities of three methanol and three water molecules were removed by SQUEEZE process. Further crystallographic details for the structure reported in this paper can be obtained from the Cambridge Crystallographic Data Center, on quoting the depository numbers CCDC 1403842-1403845.
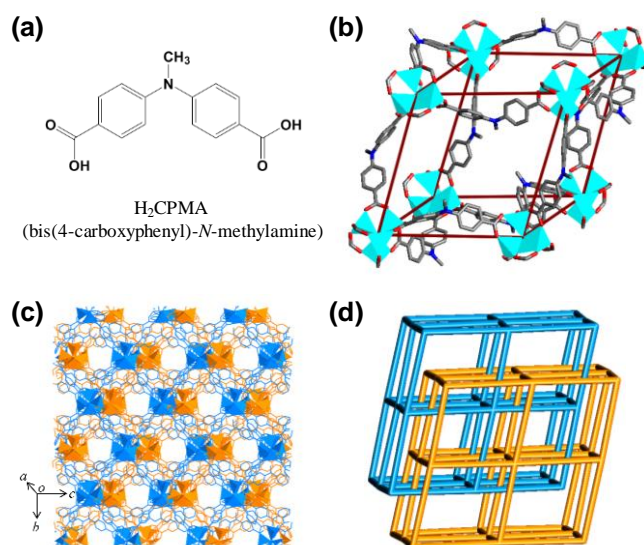
Figure 3.21. (a) Organic ligand H_2CPMA. (b) A single network unit with **pcu** topology composed of Zn_4O clusters and $CPMA^{2-}$ ditopic ligands. (c) - (d) Doubly interpenetrated 3D framework and its simplified view.

Results and discussion

The solvothermal reaction of $Zn(NO_3)_2 \cdot 6H_2O$ and H_2CPMA in DMF (DMF = *N,N*-dimethylformamide) resulted in deep-orange coloured crystals of $[Zn_4O(CPMA)_3]_2 \cdot 12DMF$ (**1**), based on the elemental analysis result. SCD analysis revealed that **1** crystallized in trigonal space group *R*32 and had a **pcu** net topology comprised of Zn_4O clusters as an octahedral SBU and $CPMA^{2-}$ ditopic ligands (Figure 3.21b).[30] The asymmetric unit of **1** contained two kinds of Zn_4O clusters with one third occupancy for each type of cluster, two $CPMA^{2-}$ ligands, as well as disordered solvent molecules. Even though the electron densities of some guest solvent molecules were observed, they could not be suitably modelled owing to severe disorders. Thus, the SQUEEZE option of PLATON was used to remove the electron densities in the void.[29] The **pcu** net was distorted to a parallelepiped structure, due to the curved dicarboxylate ligand, $CPMA^{2-}$ (Figure 3.21b), and the framework was doubly interpenetrated to generate curved 3-D channels (Figure 3.21c and d). There were π-π interactions between the phenyl rings of $CPMA^{2-}$ belonging to two interpenetrated nets (shortest C···C distances, 3.519–3.703 Å; dihedral angles, 58.88–83.37°) (Figure 3.22). PLATON calculations indicated that **1** contained 48.4% void space (103333.5 Å^3 per unit cell volume), which was occupied by the guest molecules. As seen in the TGA trace of as-synthesized **1** (Figure 3.23), the guest solvent molecules were completely removed upon heating from room temperature to ca. 150 °C with an experimentally determined weight loss of 28.7%, which was in good agreement with the calculated weight loss of 28.8%. However, the N_2-

sorption isotherm of dried **1** revealed no porosity, because **1** showed flexible, as evidenced by the XRPD patterns shown in Figure 3.24. Since dried MOF **1** lost transparency as well as single crystallinity, its SCD could not be obtained. However, the original structure of **1** was restored upon exposure to DMF vapour for 3 days at room temperature, indicating the reversibility of the structural movements.
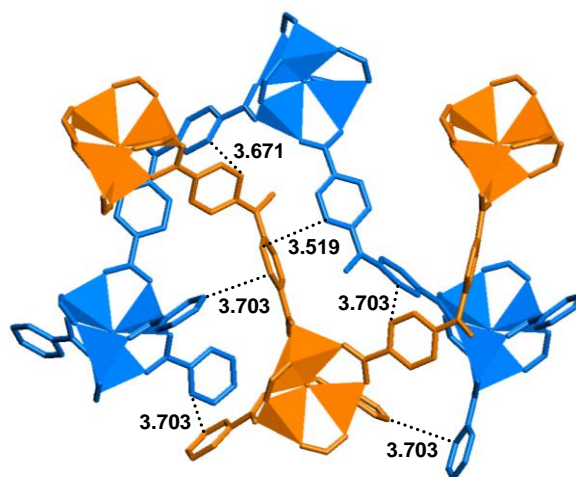

Figure 3.22. The interpenetrated structure of two *pcu* nets in **1** which interact each other via π- π interactions.
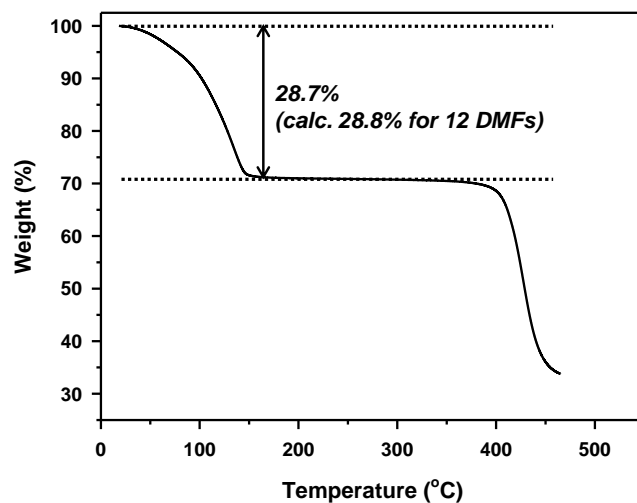
Figure 3.23. TGA trace of [Zn$_4$O(CPMA)$_3$]$_2$•12DMF (**1**). The result indicates 28.7% weight loss under 150 $^\circ$C for twelve uncoordinating DMF guest molecules (calc. 28.8%).
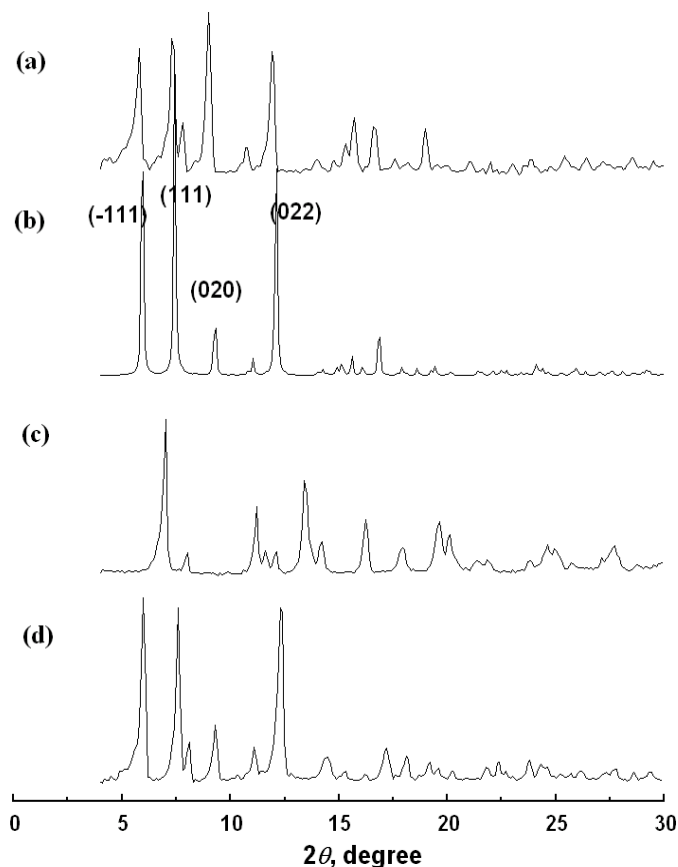
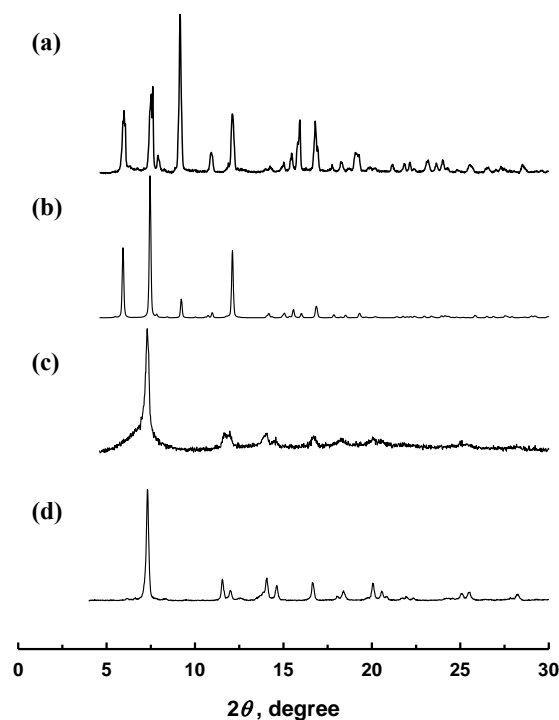**Figure 3.24.** The XRPD patterns for (a) **1** as-synthesized, (b) simulated pattern from the single-crystal X-ray data of **1**, (c) dried **1** that is prepared by heating **1** at 220 $^{\circ C}$ under vacuum for 24 h, and (d) solid isolated after exposure of dried **1** to DMF vapor for 3 days.

As revealed by guest removal and re-immersion experiments, **1** had a flexible structure, which was strongly influenced by the presence of guest molecules (Figures. 3.25-3.27). In order to determine the effects of different types of guest molecules on the structural changes, guest exchange experiments were conducted. When single crystal **1** was immersed in benzene, hexane, and methanol, in which **1** was insoluble, its crystallinity was retained to result in **1**$_{benzene}$, **1**$_{hexane}$, and **1**$_{MeOH}$, respectively, which were suitable for SCD analysis. The exchange process was traced by Fourier transform nuclear magnetic resonance (FT-NMR), and the result revealed the exchange was terminated in three days (Figure 3.28). After solvent-exchange, Fourier transform infrared (FT-IR) spectroscopy (Figure 3.29) revealed that the C=O stretching vibration of DMF molecules at 1661 cm^{-1} in **1** clearly disappeared. Instead, new peaks corresponding to the exchanged guest molecules appeared at ~3090 cm^{-1} for benzene ($v_{C-H(benzene)}$), ~2990 cm^{-1} for *n*-hexane ($v_{C-H(hexane)}$), and ~3340 cm^{-1} for methanol ($v_{O-H(methanol)}$). During the guest-exchange, possibility of dissolution and recrystallization of **1** in the new solvents was excluded by photographs obtained with an optical microscope during the immersion of the crystals, which also indicated the preservation of single-crystallinity of **1** during the exchange process (Figure 3.30).

114

Figure 3.25. The XRPD patterns for (a) $1_{benzene}$ as-synthesized, (b) simulated pattern from the single-crystal X-ray data of $1_{benzene}$, (c) dried $1_{benzene}$ that is prepared by heating $1_{benzene}$ at 200 ℃ under vacuum for 24 h, and (d) solid isolated after immersion of $1_{benzene}$ to benzene solvent for 3 d at room temperature.
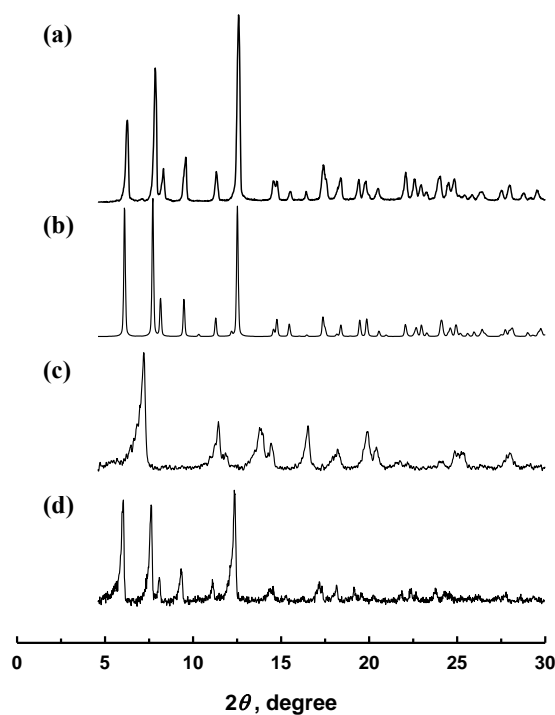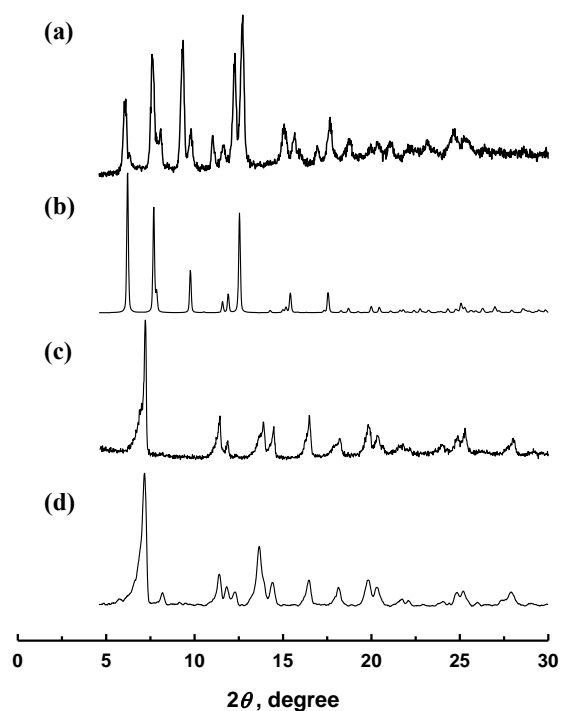

Figure 3.26. The XRPD patterns for (a) 1_{hexane} as-synthesized, (b) simulated pattern from the single-crystal X-ray data of 1_{hexane}, (c) dried 1_{hexane} that is prepared by heating 1_{hexane} at 200 ℃ under vacuum for 12 h, and (d) solid isolated after exposure of dried 1_{hexane} to hexane vapor for 3 d at room temperature.

Figure 3.27. The XRPD patterns for (a) 1_{MeOH} as-synthesized, (b) simulated pattern from the single-crystal X-ray data of 1_{MeOH}, (c) dried 1_{MeOH} that is prepared by heating 1_{MeOH} at 100 $^{\circ C}$ under vacuum for 12 h, and (d) solid isolated after exposure of dried 1_{MeOH} to methanol vapor for 3 d at room temperature.

Figure 3.28. The exchange degree of 1 with benzene as a function of time.

Figure 3.29. FT-IR spectra of **1**, **1**benzene, **1**hexane, and **1**MeOH.

Figure 3.30. Photographs of **1** crystals in guest-exchange processes. Left column: **1** as-synthesized sealed in a glass cappillary together with the mother liquor. Right column: After immsion in each organic solvent for 60 h. (a) benzene, (b) *n*-hexane, and (c) MeOH.

SCD analysis revealed the dynamic movement of the interpenetrated nets (Figure 3.31) upon the guest-exchange.[30-33] In the structure of **1**, the adjacent interpenetrated nets created two interesting spaces, which were composed of two phenyl rings from each net (Figure 3.31a). In the A site, a pair of two phenyl rings had an edge-to-edge geometry with a dihedral angle of 64.07°, but in the B site the phenyl rings were parallel to each other with a dihedral angle of 5.06°, creating a face-to-face geometry with an offset angle of 29.30°. These sites subsequently acted as important spaces for exchanged guest molecules to selectively fit into, depending on the preferred interactions. In **1_benzene**, benzene molecules were located in A sites with edge-to-face $\pi-\pi$ interactions with two phenyl rings from CPMA ligands (Figure 3.31b) (shortest C$\cdots$C distances, 3.883 Å; dihedral angles, 47.99°). Meanwhile, the dihedral angle between two phenyl rings of the framework showed minor changes as 66.36°. This was sufficient for the guest molecules to form the strongest $\pi-\pi$ interactions without significant alteration of the host framework because edge-to-face $\pi-\pi$ interactions are more stable than face-to-face interactions.[34-36] In **1_hexane**, the included *n*-hexane molecules formed CH$-\pi$ interactions with two phenyl rings of CPMA^{2-} ligands in the B sites (shortest C$\cdots$C distances, 3.919, and 4.016 Å) (Figure 3.31c). The space between the parallel phenyl rings in the B sites provided the hexane molecules with the proper environment for effective CH$-\pi$ interactions with both phenyl rings. Moreover, the offset angle of two phenyl rings changed from 29.30° (θ) to 20.02° (θ'), and the distance between the two phenyl rings became longer from 7.668 to 8.062 Å, which provides enough space to accommodate hexane molecules and constructs CH$-\pi$ interactions more efficiently (Figure 3.31c). This offset angle change is closely related with the cell parameter changes. However, in **1_MeOH**, there were no significant interactions between the MeOH molecules and the host framework except for a hydrogen bond of one methanol molecule with a carboxylate oxygen atom (Figure 3.31d). Instead, the included methanol molecules participated in guest-guest interactions with water molecules via hydrogen bonding, thus forming stronger host-host interactions via the $\pi-\pi$ interactions between the phenyl rings (Figure 3.32). TGA data of the guest-exchanged compounds also reflected the strength of the host-guest interaction depending on the guest molecules. The temperature at which the host lost its guest molecules was shifted from their boiling point depending on the strength of host-guest interactions (Figure 3.33 and Table 3.1); in **1_benzene**, the included benzene molecules were liberated at 100 °C while the boiling point of neat benzene is 80.1 °C. **1_hexane** showed much larger difference between those temperatures, 170 *vs.* 68.5 °C. In contrast, methanol molecules in **1_MeOH** evaporated completely at 60 °C, near the boiling point of MeOH, indicating its weak host-guest interactions.
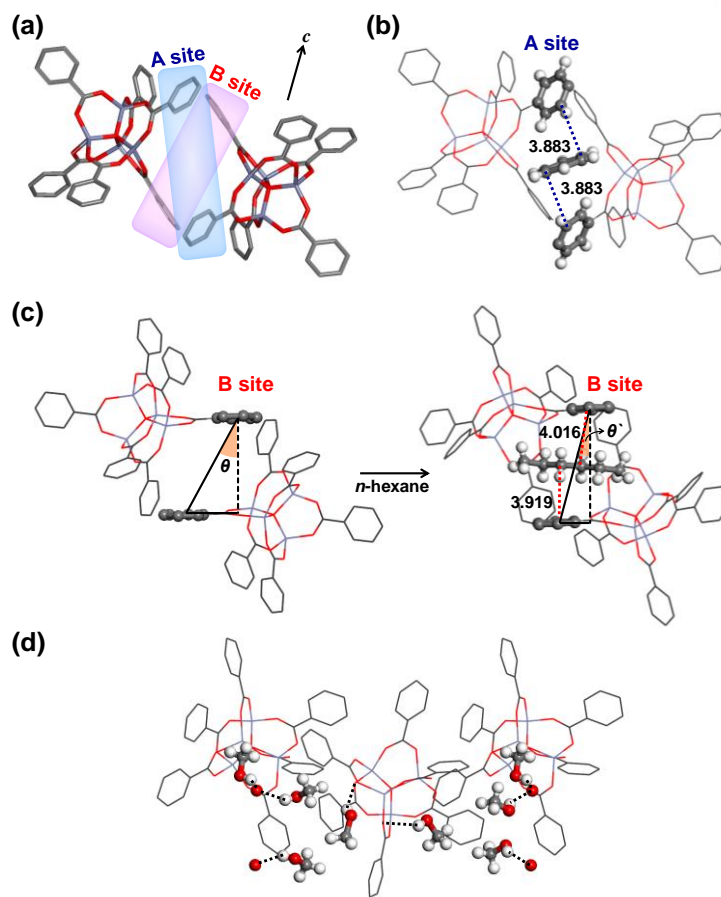
Figure 3.31. Host-guest and guest-guest interactions in (a) **1**, (b) **1$_{benzene}$**, (c) **1$_{hexane}$**, and (d) **1$_{MeOH}$**. In (c), θ and θ' are the offset angles of the two phenyl rings. Colour scheme: C (grey), O (red), H (white), Zn (purple).
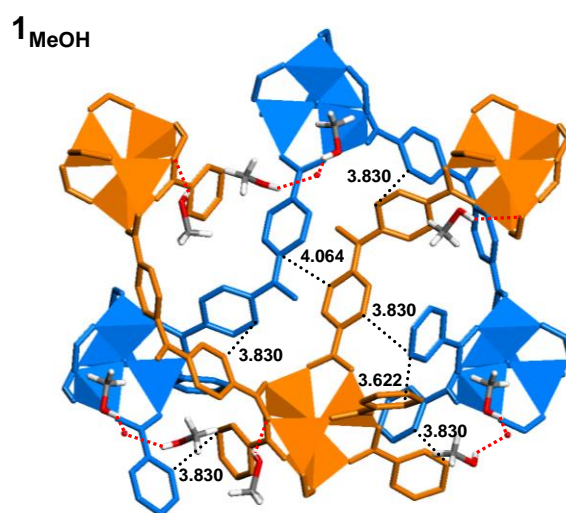

Figure 3.32. π-π interactions between doubly interpenetrated *pcu* nets and hydrogen bond interactions of MeOH molecules with water molecules or carboxylate oxygen atoms in **1$_{MeOH}$**.
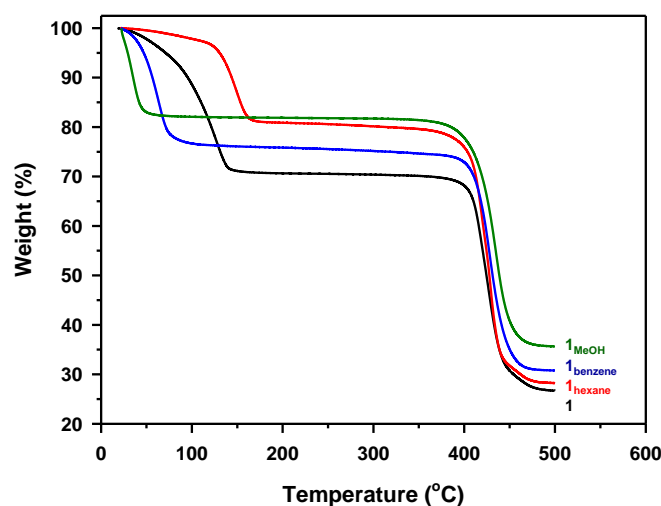
Figure 3.33. TGA traces of $[Zn_4O(CPMA)_2]_2 \cdot 12DMF$ (**1**, black), $[Zn_4O(CPMA)_3]_2 \cdot 6(n\text{-hexane})$ (**1$_{hexane}$**, red), $[Zn_4O(CPMA)_3]_2 \cdot 7benzene$ (**1$_{benzene}$,** blue), and $[Zn_4O(CPMA)_3]_2 \cdot 9MeOH \cdot 5H_2O$ (**1$_{MeOH}$**, green).

Table 3.1. Selected crystal parameters for **1**, **1$_{benzene}$**, **1$_{hexane}$**, and **1$_{MeOH}$**.

	$a = b$ (Å)	c (Å)	Cell volume (Å³)	Void volume (Å³)[a]	Intraframework O···O distance (Å³)[b]			Interframework O···O distance (Å³)[b]		Desolvating temperature (°C)[c]	Boiling point (°C)
					①-②	②-③	①-④	④-⑤	①-⑤		
1 (DMF)	18.985(3)	68.340(14)	21331(6)	10333.5 (48.4%)	15.539	16.080	33.794	12.104	21.690	150	152
1$_{benzene}$	19.168(3)	67.695(13)	21540(6)	10814.4 (50.2%)	15.582	16.029	33.535	12.519	21.016	100	80.1
1$_{hexane}$	18.653(3)	65.066(13)	19605(6)	8301.0 (42.3%)	15.283	15.283	32.533	11.000	21.533	170	68.5
1$_{MeOH}$	18.118(3)	67.542(14)	19202(5)	7865.3 (41.0%)	15.367	15.367	33.771	11.119	22.652	60	64.7

[a] Calculated by *PLATON*
[b] The numbering was indicated in the right figure.
[c] The desolvating temperature of guest molecules from MOF **1** was determined by TGA.
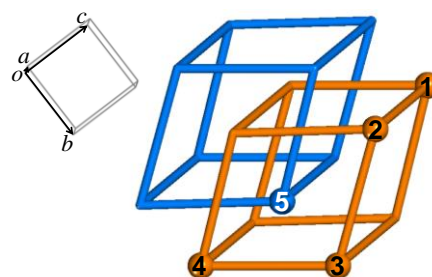
After guest exchange, the space groups remained as *R*32 for **1$_{benzene}$** and changed to *R*-3*c* for **1$_{hexane}$** and **1$_{MeOH}$**, and the dimensions of the unit cells changed significantly (Table 3.1).[30-33] This was primarily due to the interframework sliding, which was triggered by the newly formed host-guest, host-host, or guest-guest interactions upon guest-exchange, as described previously. The cell volume of **1** slightly increased from 21331(6) to 21540(6) Å³ for **1$_{benzene}$**, and significantly reduced to 19605(6) and 19202(5) Å³, for **1$_{hexane}$** and **1$_{MeOH}$**, respectively. Specially, the guest molecule exchange from DMF to MeOH led

to the greatest changes in the cell parameters, which corresponded to reduction of a cell volume by 10%, accompanied by a decrease in the void volume by 23.9%. The changes in the cell parameters were attributed to the compression of the individual **pcu** nets and the sliding motion between the interframework along the *c* axis as shown in the figure under Table 1. Since each edge of the **pcu** net conformed to the flexible CPMA ligand linking the oxo clusters (Figure 3.21b), new interactions altered the degree of framework compression, which can be expressed by the distances between oxo centres in the intraframework (Table 3.1). Consequently, since the oxo centres in positions O1 and O4 were located along the *c* axis, this framework compression directly changed the length of the c parameter. In addition, the sliding motion led to effective host-guest or host-host interactions, as described previously, and changed the interframework O···O distances between O4 and O5 as well and O1 and O5. Accordingly, 1_{hexane} and 1_{MeOH} experienced intraframework compression as well as the sliding motion, while in $1_{benzene}$ those movements did not occur significantly, because the benzene molecules fit into the A site and did not require significant structural changes. On the other hand, the offset change in 1_{hexane} led to a larger c axis compression than in other compounds, owing to CH−π interactions between hexane and the phenyl rings on the c axis (Figure 3.34). In 1_{MeOH}, the major changes were in the reduction of the *a* and *b* parameters, which were due to strong host-host interactions. The peak positions of the measured XRPD patterns for **1** and the guest-exchanged products coincided with those of the simulated patterns derived from the X-ray single-crystal data, except that the XRPD pattern of 1_{MeOH} was somewhat different from the simulated pattern (Figure 3.35). This may be because 1_{MeOH} rapidly lost MeOH molecules during the measurements. The compression of the lattice plane of 1_{hexane} and 1_{MeOH} was confirmed by the shift of the XRPD peaks to the higher angle region than those of **1** or $1_{benzene}$ (Figure 3.35).
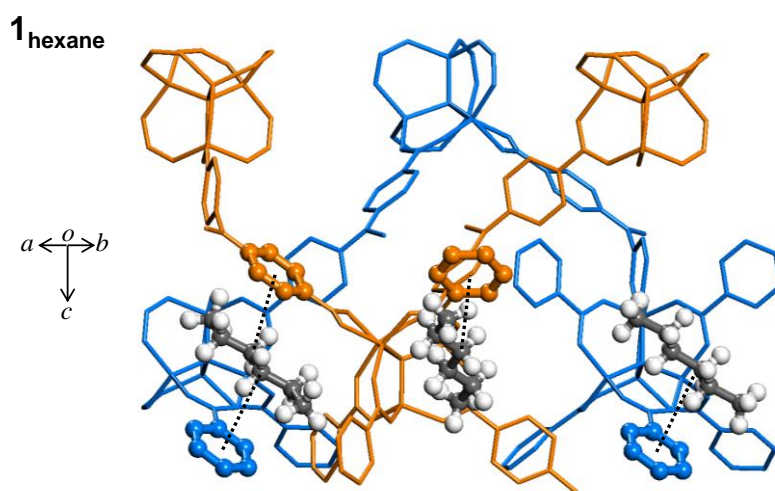

Figure 3.34. CH-π interactions between hexane molecules and phenyl rings of CPMA^{2-} ligands in the framework, 1_{hexane}.
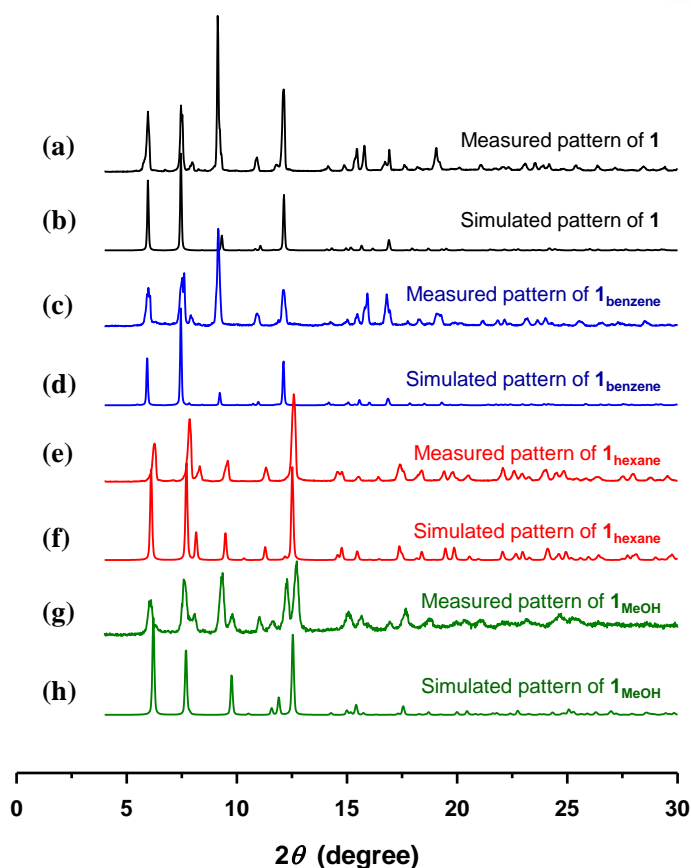
Figure 3.35. The XRPD patterns for (a) **1** as-synthesized, (b) that simulated based on X-ray single-crystal data of **1**, (c) a solid isolated **1**$_{benzene}$ after immersion of **1** in benzene for 60 h, (d) that simulated based on X-ray single-crystal data of **1**$_{benzene}$, (e) a solid isolated **1**$_{hexane}$ after immersion of **1** in *n*-hexane for 60 h, (f) that simulated based on X-ray single-crystal data of **1**$_{hexane}$, (g) a solid isolated after immersion of **1**$_{MeOH}$ in MeOH for 60 h, and (h) that simulated based on X-ray single-crystal data of **1**$_{MeOH}$.

Conclusion

A Zn$_4$O-containing doubly interpenetrated MOF with a *pcu* net, [Zn$_4$O(CPMA)$_3$]$_2$•12DMF (**1**) underwent single-crystal to single-crystal transformations upon guest exchange of DMF molecules with benzene, *n*-hexane, and methanol. SCD analysis revealed that the structural transformations involving sliding motions of the interpenetrating networks as well as dynamic movements of the molecular components were triggered by the host-guest interactions. The π−π interactions in **1**$_{benzene}$ and CH−π interactions in **1**$_{hexane}$ between the introduced solvent molecules and the phenyl rings of the CPMA^{2-} ligand in the host framework were discussed with respect to the resulting structures. Interestingly, **1** showed a significant decrease in cell volume from 21331 to 19202 Å^3 (10%) upon guest exchange with methanol, which indicated that in **1**$_{MeOH}$ the dominant force which determined the structure was the

interframework interactions rather than the host-guest interactions. In order to facilitate potential applications of MOFs in molecular sensing, separation, catalysis, and storage, it is essential to understand how MOFs respond to external stimuli and to determine the host-host, host-guest, and guest-guest interactions involved in the responses via X-ray single crystal structural analysis.

References

1. E. D. Bloch, L. J. Murray, W. L. Queen, S. Chavan, S. N. Maximoff, J. P. Bigi, R. Krishna, V. K. Peterson, F. Grandjean, G. J. Long, B. Smit, S. Bordiga, C. M. Brown, J. R. Long, *J. Am. Chem. Soc.* **2011**, *133*, 14814.
2. M.-H. Zeng, Q.-X. Wang, Y.-X. Tan, S. Hu, H.-X. Zhao, L.-S. Long, M. Kurmoo, *J. Am. Chem. Soc.* **2010**, *132*, 2561.
3. X.-N. Cheng, W.-X. Zhang, X.-M. Chen, *J. Am. Chem. Soc.* **2007**, *129*, 15738.
4. G. J. Halder, C. J. Kepert, B. Moubaraki, K. S. Murry, J. D. Cashion, *Science* **2002**, *298*, 1762.
5. K. Biradha, Y. Hongo, M. Fujita, *Angew. Chem. Int. Ed.* **2002**, *41*, 3395.
6. M. P. Suh, J. W. Ko, H. J. Choi, *J. Am. Chem. Soc.* **2002**, *124*, 10976.
7. J.-P. Zhang, P.-Q. Liao, H.-L. Zhou, R.-B. Lin, X.-M. Chen, *Chem. Soc. Rev.* **2014**, *43*, 5789.
8. S. Neogi, S. Sen, P. K. Bharadwaj, *CrystEngComm* **2013**, *15*, 9239.
9. S. Horike, S. Shimomura, S. Kitagawa, *Nature Chem.* **2009**, *1*, 695.
10. M. P. Suh, Y. E. Cheon, *Aust. J. Chem.* **2006**, *59*, 605.
11. M. P. Suh, H. R. Moon, E. Y. Lee, S. Y. Jang, *J. Am. Chem. Soc.* **2006**, *128*, 4710.
12. E. Y. Lee, M. P. Suh, *Angew. Chem. Int. Ed.* **2004**, *43*, 2798.
13. H. J. Park, M. P. Suh, *Chem. Eur. J.* **2008**, *14*, 8812.
14. C.-D. Wu, W. Lin, *Angew. Chem. Int. Ed.* **2005**, *44*, 1958.
15. H. J. Park, D.-W. Lim, W. S. Yang, T.-R. Oh, M. P. Suh, *Chem. Eur. J.* **2011**, *17*, 7251.
16. J. Y. Lee, S. Y. Lee, W. Sim, K.-M. Park, J. Kim, S. S. Lee, *J. Am. Chem. Soc.* **2008**, *130*, 6902.
17. J.-P. Zhang, Y.-Y. Lin, W.-X. Zhang, X.-M. Chen, *J. Am. Chem. Soc.* **2005**, *127*, 14162.
18. H. J. Park, Y. E. Cheon, M. P. Suh, *Chem. Eur. J.* **2010**, *16*, 11662.
19. H. J. Choi, M. P. Suh, *J. Am. Chem. Soc.* **2004**, *126*, 15844.
20. D.-W. Lim, S. A. Chyun, M. P. Suh, *Angew. Chem. Int. Ed.* **2014**, *53*, 7819.
21. B. F. Abrahams, H. E. Maynard-Casely, R. Robson, K. F. White, *CrystEngComm* **2013**, *15*, 9729.
22. A. Husain, M. Ellwart, S. A. Bourne, L. Öhrström, C. L. Oliver, *Cryst Growth Des.* **2013**, *13*, 1526.
23. H.-L. Jiang, T. A. Makal, H.-C. Zhou, *Coord. Chem. Rev.* **2013**, *257*, 2232.
24. R. Yang, L. Li, Y. Xiong, J.-R. Li, H.-C. Zhou, C.-Y. Su, *Chem. Asian J.* **2010**, *5*, 2358.
25. T. K. Maji, R. Masuda, S. Kitagawa, *Nature Mater.* **2007**, *6*, 142.
26. Y. Takashima, V. M. Martínez, S. Furukawa, M. Kondo, S. Shimomura, H. Uehara, M. Nakahama, K. Sugimoto, S. Kitagawa, *Nature Comm.* **2011**, *2*, 168.
27. H. Aggarwal, P. M. Bhatt, C. X. Bezuidenhout, L. J. Barbour, *J. Am. Chem. Soc.* **2014**, *136*, 3776.
28. T. K. Kim, J. H. Lee, D. Moon, H. R. Moon, *Inorg. Chem.* **2013**, *52*, 589.
29. *PLATON* program: A. L. Spek, *Acta Crystallogr.* **2015**, *C71*, pp. 9.
30. Crystal data for **1** ($Zn_8C_{90}H_{66}N_6O_{26}$), M_r = 2170.45, *Trigonal*, space group *R*32 (no. 155), a = 18.985(3), b = 18.985(3), c = 68.340(14) Å, α = 90°, β = 90°, γ = 120°, V = 21331(6) Å^3, Z = 6, d_{calcd} = 1.014 g cm^{-3}, T = 100(2) K, crystal size 0.28 x 0.25 x 0.20 mm^3, λ = 0.70000 Å, 2θ = 58.00, 346 parameters, R_1 = 0.0551 ($I > 2\sigma(I)$, 12870 reflections), wR_2 = 0.1835 (all data, 65641 reflections), GOF = 1.004. Further crystallographic details for the structure can be obtained from the Cambridge Crystallographic Data Center, on quoting the depository number CCDC 1403842.

31. Crystal data for $1_{benzene}$ ($Zn_{16}C_{198}H_{150}N_{12}O_{52}$), M_r = 4575.22, *Trigonal*, space group *R*32 (no. 155), a = 19.168(3), b = 19.168(3), c = 67.695(13) Å, α = 90°, β = 90°, γ = 120°, V = 21540(6) Å^3, Z = 3, d_{calcd} = 1.058 g cm^{-3}, T = 100(2) K, crystal size 0.22 x 0.18 x 0.15 mm^3, λ = 0.70001 Å, 2θ = 50.00, 385 parameters, R_1 = 0.0563 ($I > 2\sigma(I)$, 8835 reflections), wR_2 = 0.1783 (all data, 48637 reflections), GOF = 1.056. Further crystallographic details for the structure can be obtained from the Cambridge Crystallographic Data Center, on quoting the depository number CCDC 1403843.

32. Crystal data for 1_{hexane} ($Zn_4C_{63}H_{75}N_3O_{13}$), M_r = 1343.74, *Trigonal*, space group *R*-3*c* (no. 167), a = 18.653(3), b = 18.653(3), c = 65.066(13) Å, α = 90°, β = 90°, γ = 120°, V = 19605(6) Å^3, Z = 12, d_{calcd} = 1.366 g cm^{-3}, T = 100(2) K, crystal size 0.26 x 0.23 x 0.19 mm^3, λ = 0.77999 Å, 2θ = 62.00, 321 parameters, R_1 = 0.0575 ($I > 2\sigma(I)$, 8067 reflections), wR_2 = 0.1753 (all data, 77769 reflections), GOF = 0.998. Further crystallographic details for the structure can be obtained from the Cambridge Crystallographic Data Center, on quoting the depository number CCDC 1403844.

33. Crystal data for 1_{MeOH} ($Zn_4C_{51}H_{57}N_3O_{20}$), M_r = 1293.48, *Trigonal*, space group *R*-3*c* (no. 167), a = 18.118(3), b = 18.118(3), c = 67.542(14) Å, α = 90°, β = 90°, γ = 120°, V = 19202(5) Å^3, Z = 12, d_{calcd} = 1.342 g cm^{-3}, T = 100(2) K, crystal size 0.26 x 0.20 x 0.17 mm^3, λ = 0.54999 Å, 2θ = 51.00, 237 parameters, R_1 = 0.1078 ($I > 2\sigma(I)$, 5205 reflections), wR_2 = 0.3361 (all data, 53363 reflections), GOF = 1.173. Further crystallographic details for the structure can be obtained from the Cambridge Crystallographic Data Center, on quoting the depository number CCDC 1403845.

34. M. L. Waters, *Curr. Opin. Chem. Biol.* **2002**, *6*, 736.

35. J. Singh, J. M. Thornton, *J. Mol. Biol.* **1991**, *218*, 837.

36. C. A. Hunter, J. K. M. Sanders, *J. Am. Chem. Soc.* **1990**, *112*, 5525.

37. T. K. Kim, J. H. Lee, D. Moon, H. R. Moon, *Inorg. Chem.* **2013**, *52*, 589.

38. A. J. Arvai, C. Nielsen, *ADSC Quantum-210 ADX Program*, Area Detector System Corporation; Poway, CA, USA, **1983**.

39. Z. Otwinowski, W. Minor, Methods in Enzymology, Part A. In *Macromolecular Crystallography*; Carter Jr., C. W., Sweet, R. M., Eds.;, Academic Press: New York, **1997**; Vol. 276, pp 307-326.

40. G. M. Sheldrick, SHELXTL-PLUS, Crystal Structure Analysis Package; Bruker Analytical X-Ray; Madison, WI, USA, **1997**.

41. *PLATON* program: A. L. Spek, *Acta Crystallogr.* **2015**, *C71*, 9.

Acknowledgement